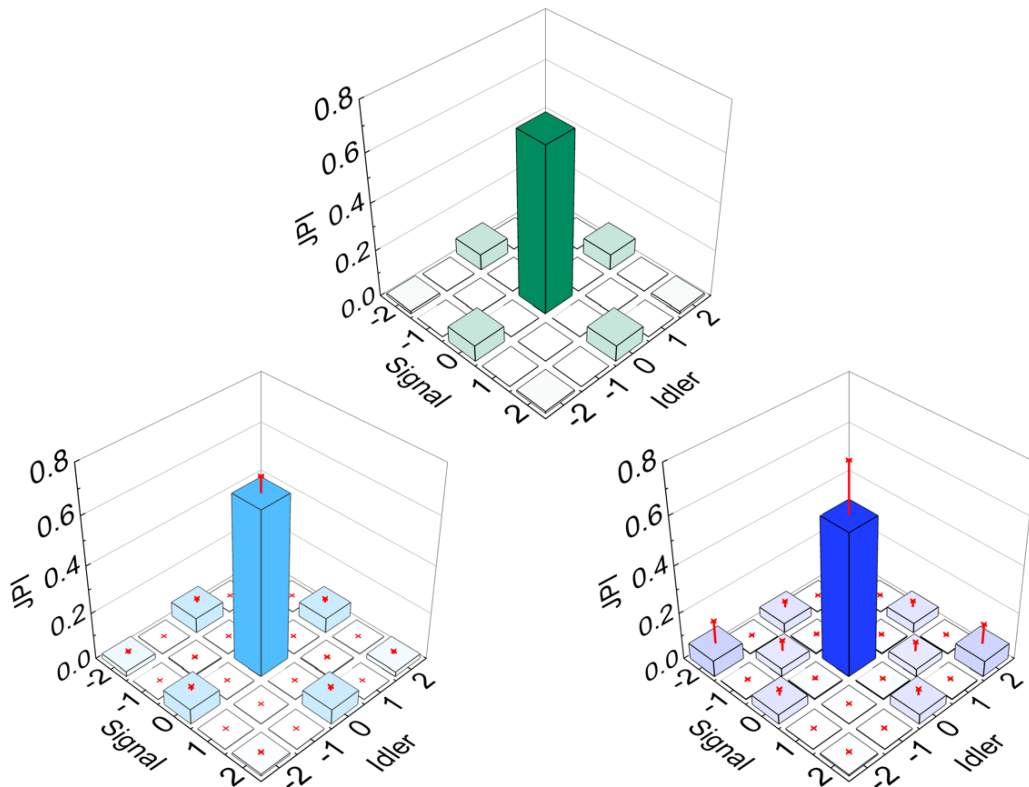


Generation of nonclassical light in topologically protected photonic structures

Nicola Bergamasco



Tesi per il conseguimento del titolo



Università degli Studi di Pavia
Dipartimento di Fisica

DOTTORATO DI RICERCA IN FISICA – XXXIII CICLO

Generation of nonclassical light
in topologically protected
photonic structures

Nicola Bergamasco

Submitted to the Graduate School of Physics in partial
fulfillment of the requirements for the degree of

DOTTORE DI RICERCA IN FISICA
DOCTOR OF PHILOSOPHY IN PHYSICS

at the

University of Pavia

Supervisor: Prof. Marco Liscidini

Cover: Joint path intensity of the generated photon pairs for the unperturbed structure, $\sigma = 14$ nm, and $\sigma = 43$ nm of disorder (from top, counterclockwise)

Generation of nonclassical light in topologically protected photonic structures

Nicola Bergamasco

PhD thesis - University of Pavia

Pavia, Italy, June 2021

CONTENTS

Introduction	iii
1 Elements of topological photonics	1
1.1 The Su-Schrieffer-Heeger model	1
1.2 Tight-binding scheme	3
1.3 Disorder and topological protection	11
2 Elements of quantum nonlinear photonics	15
2.1 Nonlinear optical processes	16
2.2 The asymptotic fields method	21
2.3 The backward Heisenberg picture approach	25
2.4 Figures of merit	30
3 Path states in a single topological mode	33
3.1 Structure and field propagation	34
3.2 Two-photon state generation	37
3.3 Topological protection of the quantum state	41
3.4 Conclusions	46
4 Hyper-entangled states in coupled topological modes	49
4.1 Structure and field propagation	50
4.2 Two-photon state generation	53
4.3 Topological protection of the quantum state	59
4.4 Conclusions	64
5 Beyond photon pairs: Squeezed states	67
5.1 Introduction to squeezed states	68
5.2 Channel operator formalism	71
5.3 Green function solution	74
5.4 Channel coupling and further developments	79

Conclusions	81
Appendix	85
List of publications	93
Bibliography	94

INTRODUCTION

In the past decade part of the scientific community working on integrated photonics has shifted its attention to the study of topological structures. This interest is justified not only by the curiosity of exploring new aspects of photonics, in which one can mix light-matter interactions with the topological properties of the medium, but also by the necessity to find an approach that mitigates the imperfections and defects introduced by present fabrication technologies. Indeed, the main reason for combining topology and photonics resides in the idea that topological properties observed in solid state systems, such as scattering-free propagation of electrons, can be transferred to the propagation of light, thus providing a method to avoid optical losses and degradation of the quantum states of light generated in these photonics structures. These problems are a pressing matter in view of the development of *photonic quantum technologies*, which are devices designed to generate and manipulate quantum states of light for the purpose of solving specific tasks in many fields like quantum communication, information, and computation, sensing, and metrology.

Against this background, we considered the new direction opened by topological photonics to be a very interesting topic because, as theoretical researchers in the field of photonics, we always pay great attention to the imperfections that may affect our designs when they are created in the real world. This awareness comes from our close collaboration with groups working on the fabrication side, and reminds us of the limits of current technology. Knowing this, we decided to dedicate part of our time to investigate a representative class of topological structures that are easy to study, with the intent to understand the impact of topology on the generated quantum states. Eventually, this study grew to become the core of my thesis and thus the work we present here wants to bring a small but significant contribution to this field, with the aim of clarifying some crucial aspects related to the generation of non-classical light in topological photonic structures. In this introduction we try to give a broad view on the developments of topological photonics, from which we borrow the key concepts, and photonics, in which

this work is well-rooted and constitutes the main topic. The two fields crossed each other in recent times enabling a new line of scientific development.

Perhaps the most common example that comes to mind when we talk about topology is the geometrical equivalence between a 'doughnut' and a 'mug'. The argument that one usually makes is that the surface enclosing one of the two objects can be *continuously* deformed to the point it becomes the other, and this is possible only because we *preserve* a key feature, called *topological invariant*, that is represented in this case by the number of 'holes' in the geometry of the surface. Indeed one can think of topology as the branch of mathematics that study the conservation of quantities, typically represented in the form of integer numbers, under the action of continuous deformations of the system. These concepts have been adapted to study many problems related to solid state physics and in particular they played a major role in the understanding of phenomena like the quantum Hall effect [1–3], which is one of the first problems where the idea of *topological insulator* is introduced. These topological phases of matter, while acting as insulators in the bulk, are able to conduct electrons on the surface without scattering even when large defects or impurities are present. In these systems the topological invariant is strictly connected to the band structure and the transition from one topological phase to the other, which happens at the surface where one observes scattering-free propagation, is associated with the formation of a topological mode inside a gap of the band structure.

Later, these principles have been transferred to photonics and an analogue behaviour was demonstrated in the microwave range [4–6]. Further studies in this direction managed to achieve similar result in integrated photonic structures [7, 8] thus expanding the potential applications of topology with the flexibility of the fabrication processes used to produce integrated photonic devices. Although the concept of topological phase transition and the analysis of the band structure in reciprocal space allows an in-depth view of the topological nature of a system, a more direct way to investigate topological protection consists in creating a discontinuity in a photonic structure with a uniform topology. As a result a new mode supported by the structure appears and one can show that it is topologically protected. Its linear properties, like other guided modes in photonic structures, are characterized by a propagation constant and a field distribution of the mode, and can be easily studied with this approach.

Moving away from the study of the linear properties to the generation of quantum states of light in such topological structure, we must provide a theoretical background, within the framework of quantum mechanics, for the description of the processes involved, and these fall within the field of competence of photonics. Photonics has a long history that arks back to the

first works of P. Franken, N. Bloembergen, and others [9, 10] on classical nonlinear optical phenomena in bulk crystals. These processes involve, as a first approximation of the light-matter interaction, the second order $\chi^{(2)}$ and third order $\chi^{(3)}$ susceptibilities that describe the response of the medium to the incident light. These response functions are very weak compared to the typical linear susceptibility and it is not surprising that the development of this field of optics started in the '60s together with the introduction of the first laser sources. Each nonlinear susceptibility is associated with a set of different processes. Just to name the most commonly used, we can think of second harmonic generation (SHG) and difference frequency generation (DFG) for $\chi^{(2)}$, and four-wave mixing (FWM) for $\chi^{(3)}$. All these nonlinear processes have the common characteristic of being classical, that is they can be described with a completely classical treatment of electrodynamics.

We have to wait the '70s and '80s to see the first experiments involving the respective quantum processes of spontaneous parametric down-conversion (SPDC) [11], corresponding to the inverse process of SHG, and spontaneous four-wave mixing (SFWM) [12] associated to FWM. Both quantum processes have been used extensively in the study of quantum correlations of entangled photon pairs. As the adjective *spontaneous* suggests, these processes are stimulated not by the presence of a seeding field, but by the quantum fluctuations of the vacuum state of radiation at the frequencies where the photons are generated, and they can be understood only with a quantum mechanical description of the electromagnetic field.

The growing interest in the quantum properties of light and the development of novel quantum applications demands platforms with an ever-growing number of components for the generation and manipulation of the quantum state of photons. This trend, if pursued with the use of bulk optical components, in the end leads to unrealistic prospects to scale the applications, and to a poor quality of the target quantum state because of the difficulty in stabilizing all the elements. The natural evolution followed the path of *integration* [13] already seen in electronics, with bulk components transformed into elements of integrated photonic circuits for the generation, manipulation, and later also detection [14] of quantum light. But, as the number of elements grows in a photonic circuit, the quantum mechanical description of the generation and propagation of non-classical light becomes difficult, for it requires more and more terms in the Hamiltonian of the system [15]. This problem has been addressed in recent years, with the development of novel theoretical approaches for photonic structures of arbitrary complexity, allowing a simplified description of both the electrodynamics and the quantum state evolution.

It is at this point, when integrated photonics has reached a maturity

that makes it possible to include many elements in a single platform, that topology and photonics finally meet. The current technological level allows the precise repetition of many integrated elements, which is fundamental for the creation of topological photonic circuits and the investigation of their properties. These structures are interesting for both theoretical and practical reasons, as they allow to study the light-matter interaction under the constraints imposed by topology and might provide new ways to improve the current technologies that rely on photonics. Since topological photonic structures are in general more complex and extended compared to a typical photonic circuit performing similar tasks, a careful investigation of their properties is useful to evaluate the trade-off with the promised benefits, and this contributes to justify the interest in this novel field of research.

The work we present here can be divided into three parts, each with a different goal. In the first part, formed by chapters 1 and 2, we provide to the reader all the necessary elements to understand the results. In particular, in Ch. 1 we give a brief background on recently developed topological photonic structures and introduce the one specifically studied in this work, which is based on an array of waveguides. This particular geometry offers many advantages compared to other implementations since waveguide arrays: (i) are known and well-studied photonic platforms that can be analyzed theoretically with simple models and (ii) automatically provide the 'path' as an additional degree of freedom for the state of propagating photons. The second point highlights a kind of synergy in the structure, for the creation of a topology (and a topological defect) requires the specific arrangement of many waveguides as fundamental building block units. Thus, the 'path' degree of freedom can't be avoided but at the same time it's the one that is actually protected by topology. One can certainly envision practical applications based on this features and, obviously, if the goal is just the generate photon pairs there are way simpler structures that can be used, like a single waveguide instead of a whole array. However in this work we focus specifically on the topological protection mechanism and its relation with the generation of photons pairs and their state. In this chapter we deal mainly with the linear characterization of the two topological structures, that is, we focus on the properties supported modes in terms of propagation constants and field distribution, pointing out the differences between the topological mode and the other modes. We introduce the type of disorder and statistical analysis considered in our simulations and we demonstrate the protection of the linear properties of the topological mode.

In Ch. 2 we transition from the linear regime of light propagation to the nonlinear optical interactions, which are the cornerstone of non-classical light generation. It is at this point that a proper formalism for the quantization of

electromagnetic fields is introduced to show how the two processes of SPDC and SFWM emerge from their respective Hamiltonian terms. At the same time, the problem of describing SPDC and SFWM in complex structures is addressed by means of two methods: (i) the construction of asymptotic fields, which are full solutions of the linear Maxwell equations and can be used as a basis to solve the nonlinear interaction problem, and (ii) the backward-Heisenberg picture, with which we derive the quantum state of the generated photons from an initial state, in our case describing a laser pulse. The main properties of the generated state are commented in detail and then the chapter concludes with a description of a set of 'figures of merit' that can help us characterize the effects of topological protection on the generated photons.

The second part, formed by chapters 3 and 4 is the core of this work, here we report in detail our findings on the topological protection of the quantum state of the photon pairs. In Ch. 3 we focus on the first of the two waveguide arrays introduced in chapter 1. This structure is based on a silicon platform and the photon pairs are generated by SFWM. It has been studied experimentally by the group of Blanco-Redondo [16, 17] but the difficulties to perform a complete analysis of disorder on samples didn't led to definitive conclusions on the topological protection of the quantum state. In detail, the number of characterized samples was inevitably low, just few units, and the fabrication imperfections affected also the geometry of waveguides, thus invalidating the study of disorder on their position. With our statistical analysis of a large set of simulations we can consider hundreds of structures, with the assurance that the waveguides are always identical to the original. Our findings greatly improve their results and provide very interesting insights of the interplay between topology and nonlinear interactions in the process of photon pair generation. This in-depth analysis highlights the mechanisms that reduce the topological protection when nonlinear interactions are considered.

In Ch. 4 we take the chance to study topological protection under different conditions. The platform is now based on lithium niobate, a promising material for integrated photonics with a strong second order nonlinearity, which we use to generate photon pairs by SPDC. We also change the structure, introducing two interacting topological modes that are strongly coupled to each other, and with this configuration we demonstrate that it's possible to generate quantum states that are hyper-entangled in energy and path. Here the study of disorder on the topological protection also focus on the robustness of hyper-entanglement and shows similar results to those of Ch. 3 for the same figures of merit. However a further analysis of the generated states shows that the mechanisms that reduce the topological protection are not the same but are related mostly to the structure symmetry.

Finally, the third and final part in chapter 5 anticipates a future direc-

tion of our research that goes beyond the generation of photon pairs. Indeed, the theory presented in chapter 2 is valid only under the condition that the pump power is low enough to discard the possibility of generating multiple photon pairs. Here we relax this condition and develop a mathematical approach that is more suitable for the high power regime, where the result of the nonlinear interaction is the generation of a different kind of quantum state, called *squeezed state*. The properties of squeezed states are well-known in quantum optics, in particular their characteristic of having reduced uncertainty on the measure of a physical observable. This aspect is of great practical interest in metrological applications where it is crucial to reduce by several decibels even the quantum noise associated with the Heisenberg uncertainty relations. The price for this is an increase in the uncertainty for the conjugate observable, which is typically not employed in the setup and thus sacrificed. Compared to other platform used for the generation of squeezed states, topological protection could be an additional benefit that strengthen the stability of the state. Moreover, since the generation process is different from both SPDC and SFWM, it is worth investigating also in this case how the quantum correlations are affected by disorder. The chapter mainly deals with the mathematical formalism for a single isolated waveguide and the numerical method to solve the equations for the quantum operators introduced. We show that this approach reproduces the results expected from the usual photon pair approximation, when operating in the low power limit, and the expected exponential scaling when the power is sufficiently high to generate multiple pairs. We conclude presenting a straightforward extension to coupled waveguides and commenting on the possible difficulties of simulating this structure with our numerical method and in the presence of disorder.

1 ELEMENTS OF TOPOLOGICAL PHOTONICS

After the experimental verification of the first topological photonic system in the microwave regime [6], there's been an increasing interest into the development of similar devices that could operate in the optical spectrum. Following this seminal work, some implementations focused on creating optical systems which, with the help of an external field, provided either by modulation of coupling phases in a lattice of resonators [18] or induced strain [19], could be described by an Hamiltonian similar to that of the quantum Hall effect. Other works showed that topological properties could be obtained in systems without the help of external fields, using for example polarization in a 2-dimensional array of Bragg waveguide [20], or pairs of counter propagating modes in coupled resonators optical waveguides (CROW) [21, 22]. All these implementations achieved robust propagation of light in 2-dimensional systems through the formation of a topologically protected mode propagating at the edge of the structure, or at the interface between two regions with different topological phases. Yet, it's possible to create photonic structures supporting propagating topological modes also in 1-dimensional systems, which greatly reduce the complexity of the structure. The simplest way to achieve this is by creating a dimer chain that follows the Su-Schrieffer-Heeger (SSH) model [23].

1.1 THE SU-SCHRIEFFER-HEEGER MODEL IN PHOTONICS

The SSH model takes its name from the researchers who first studied the electronic properties of *polyacetylene*, a conjugated linear molecule formed by the repetition of the functional group CH_x . In their publication they demonstrated theoretically the formation of an electronic topological mode at the center site of the molecule chain. A sketch of the chemical structure is

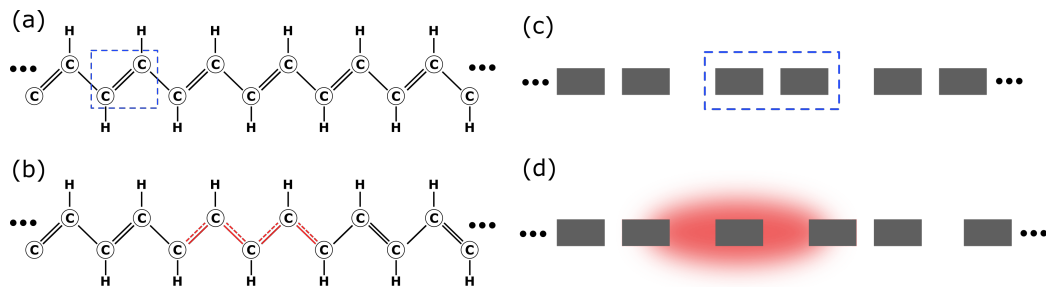


Figure 1.1: (a) Polyacetylene molecule in the SSH model, the dimers formed by double bonds (dashed box) are connected by single bonds. (b) Domain wall (red bonds) where the topological state is localized. (c) Photonic equivalent of the SSH model using waveguides (cross section) and (d) the configuration with a localized topological mode (red region).

shown in Fig. 1.1 (a) where one can see that the carbon atoms are connected by alternating double (σ and π) and single (σ) bonds. Because of this arrangement of chemical bonds, two degenerate stable structure can exist that differ only by the swapping of the single and double bonds, as can be seen intuitively. As a consequence of this degeneracy one expects the formation of an electronic topological mode formed by one unpaired spin. In Fig. 1.1 (b) we show the region of interest where the bonds are marked in red. This localized mode appear because in a region of the molecule chemical bonds are arranged in one of the two stable configurations, while on the other side the other configuration takes over. At a certain lattice position these two domains come into contact but there's no way to arrange the bonds in that point such that both configurations are respected. Thus, around the domain wall a localized electronic state of topological nature emerges.

This type of system, which can be seen also as a chain composed of *dimers* [see Fig. 1.1 (a)] having an internal (intra-dimer) and external (inter-dimer) coupling strength, has been exploited to create 1-dimensional photonic systems composed of waveguide lattices [24] or quasi-crystals supporting topological photonic modes [25]. Indeed the two systems, although different, can be described with the same underlying mathematical model. In [23] we see that the electrons forming the π bonds are described using a *tight-binding* model with bond energies regulating the probability of one electron to jump from one site of the lattice to the other. In a photonic system we have instead waveguides supporting one or more guided modes where light can propagate. If the waveguides are not too far from each other, such that the evanescent coupling of the modes is not negligible, then light can pass from one waveguide to the other, or if we talk about single photons, there's a probability

amplitude that a photon hops into the adjacent waveguides. In Fig. 1.1 (c) we show a typical array of waveguides that reproduce the stable configuration in Fig. 1.1 (a). As one can see the dimer representing the atoms connected by a double bond is formed by two waveguides separated by a short gap, and adjacent dimers are separate from each other by a longer gap to represent the single bond. This approach gives a one-to-one correspondence between the electronic and photonic systems, so it is expected that the supported supermodes of this photonic structure will also include a topological photonic mode. This procedure has been followed in recent works on photonic SSH model in waveguide arrays [16, 17], where the correctness of this choice of coupling scheme has been demonstrated in terms of topological phases of the 1-dimensional array in the reciprocal space. The creation of a topological guided mode is achieved in this photonic structure by repeating a long gap in the sequence, as depicted in Fig. 1.1 (d), where the region highlighted in red indicates where the topological mode is localized. The other alternative, consisting in the repetition of two short gaps creates a region with a higher average index of refraction leading to the formation of a topological mode and two trivial defect modes. Since in this alternative configuration it is difficult to study the topological mode because of the presence of the other two modes, in the following we will always consider the first method with two long gaps.

1.2 TIGHT-BINDING SCHEME IN WAVEGUIDE ARRAYS

Before discussing the mathematical formulation of the tight-binding scheme in a photonic structure reproducing the SSH model, we introduce the two waveguide arrays that we are going to study in this work. The first structure that we investigate is a silicon over insulator (SOI) platform composed of an array of 203 identical silicon waveguide fabricated over a silica substrate. This array has the identical geometrical parameters of the one studied experimentally in [17] and we choose to keep them to make a direct comparison of our theoretical findings with their experimental results. In Fig. 1.2 (a) we show a sketch representing the portion of the array where the topological defect is localized. The waveguides have typical geometrical parameters for a silicon platform, with a height $h = 220$ nm and a width $w = 450$ nm, and are separated by short (S) and long (L) gaps of width $d_S = 173$ nm and $d_L = 307$ nm, respectively. This structure is used to study the generation of photon pairs by SFWM at the wavelength $\lambda = 1550$ nm, where the only sup-

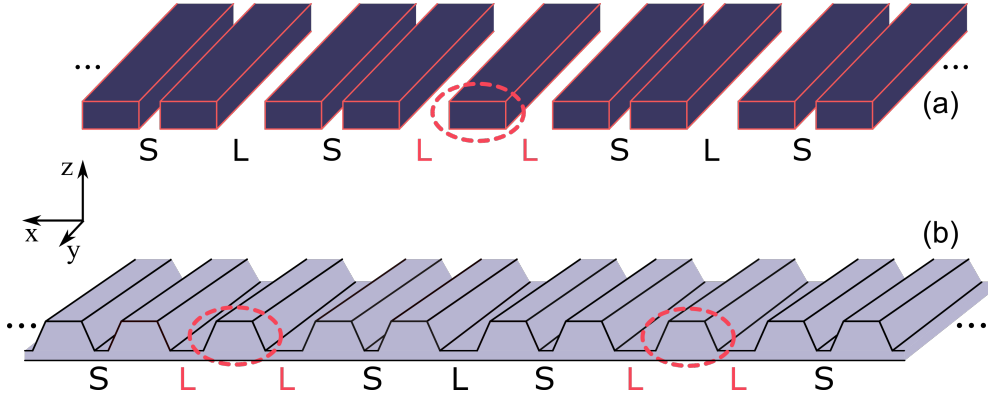


Figure 1.2: (a) Array of ridge silicon waveguides on silica with alternating short (S) and long (L) gaps. The topological mode is localized around the waveguide (dashed circle) separated by a L-L gap defect. (b) Array of rib waveguides made of lithium niobate over silica supporting two strongly coupled topological modes.

ported mode is the fundamental transverse-electric (TE₀) mode. The second structure is based, instead, on a lithium niobate over insulator (LNOI) platform, and is composed of an array of 42 identical trapezoidal rib waveguides. The rib geometry of the array is obtained, during the fabrication process, by partially etching a Z-cut lithium niobate (LN) film deposited on a silica substrate [26]. The trapezoidal waveguides have a top width $w = 1.2 \mu\text{m}$, a height $h = 460 \text{ nm}$, and a side angle of 75° . The residual non-etched film has a thickness $t = 100 \text{ nm}$ and acts as an additional LN support layer. The waveguides are separated by alternating short (S) and long (L) gaps having widths $d_S = 300 \text{ nm}$ and $d_L = 450 \text{ nm}$, respectively, measured at the base. In Fig. 1.2 (b) we show the portion of the array where we introduce two topological defects at a distance of a few waveguides. Because of the short distance between the two defects, the array supports two topological modes with symmetric and anti-symmetric field distributions, respectively. These two modes can be viewed as arising from the strong coupling of the two topological modes that would be supported by each defect when taken individually. Unlike silicon, LN is a material that possesses also a strong second order $\chi^{(2)}$ nonlinearity and this structure is intended for the study of photon pair generation by SPDC. Considering this, the modes in which we are interested are the second transverse-magnetic (TM₂) mode at $\lambda = 775 \text{ nm}$ and the fundamental TE₀ mode at $\lambda = 1550 \text{ nm}$. Further details on the modes related to the SFWM and SPDC processes are provided in Ch. 3 and 4 where we study the state of the generated photons.

To describe light propagation in both these structure we adopt a simplified mathematical model in which the key point is to assume that the waveguides are sufficiently far from each other that their guided modes can be considered *orthogonal*. Of course, this hypothesis must hold even when the structures are modified by disorder, and this has been verified for all the levels of positional disorder considered in this work. Under this assumption, the field inside each structure can be written as a superposition of fundamental modes of each waveguide. In particular, the electric displacement $\mathbf{D}(\mathbf{r}, t)$, which is our fundamental field [27], can be written as

$$\mathbf{D}(\mathbf{r}, t) = \frac{1}{\sqrt{2\pi}} e^{i(k_0 y - \omega t)} \left[\sum_{i=1}^N c_i(y) \mathbf{d}_i(x, z) \right], \quad (1.1)$$

where k_0 is the propagation constant of the supported mode under consideration, which is factored out since the waveguides are identical, ω is the angular frequency, and $\mathbf{d}_i(x, z)$ is the transverse field distribution centered on the i -th waveguide. Finally, $c_i(y)$ are amplitude coefficients that depend on the position y along the array due to the coupling between adjacent waveguides, allowing the transfer of energy. Energy conservation and normalization of the supermodes require that at each point y we have

$$\sum_{i=1}^N |c_i(y)|^2 = 1. \quad (1.2)$$

Under the hypothesis of orthogonal modes the coupling between the waveguides is small and light propagation along y can be described through coupled wave analysis in a tight-binding approach. Within this mathematical framework the amplitudes $c_i(y)$ depend from each others through a set of coupled linear differential equations

$$\frac{d}{dy} c_i(y) = -i\sigma_{i,i-1}(\omega) c_{i-1}(y) - i\sigma_{i,i+1}(\omega) c_{i+1}(y) \quad i = 1 \dots N, \quad (1.3)$$

where the real frequency dependent coefficients $\sigma_i(\omega)$ provide the coupling between the amplitudes $c_i(y)$ and satisfy the boundary condition

$$\sigma_0(\omega) = \sigma_{N+1}(\omega) = 0 \quad (1.4)$$

for an array with a finite number of waveguides.

To determine the values that $\sigma_i(\omega)$ can take in an array where the gaps between waveguides change, we fix the frequency for a moment and consider a simple structure consisting of just two identical waveguides running in parallel close to each other. If the propagation constant of the mode supported

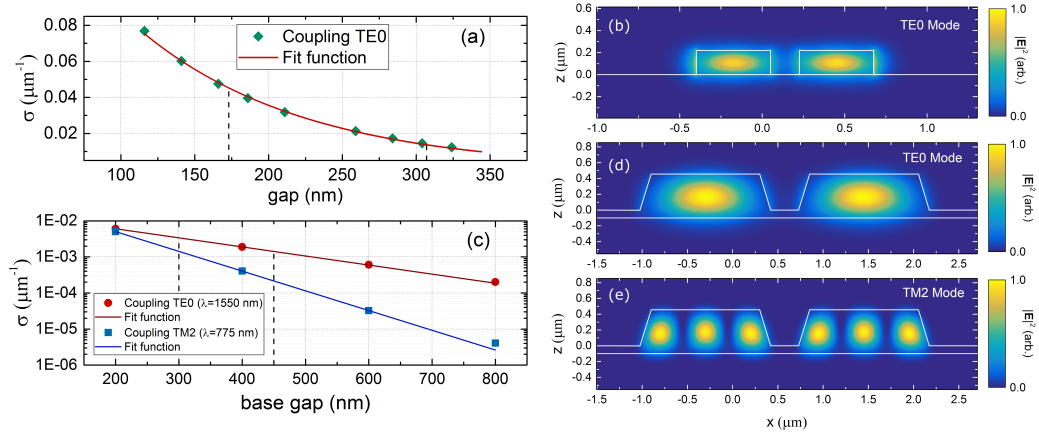


Figure 1.3: (a) Coupling constants σ as a function of the gap between two silicon waveguides for the TE0 mode (b); the unperturbed short and long gaps (dashed lines) are $d_S = 173$ nm and $d_L = 307$ nm. (c) Coupling σ between two LN waveguides for the TE0 (d) and TM2 (e) modes at $\lambda = 1550$ nm and $\lambda = 775$ nm, respectively. The unperturbed short and long gaps (dashed lines) are $d_S = 300$ nm and $d_L = 450$ nm.

by each isolated waveguide is k_0 , then it can be shown through coupled wave analysis that the coupling produces two modes with propagation constants $k_{\pm} = k_0 \pm \sigma$, where σ is the coupling coefficient. This means that for a frequency ω and a gap distance d between the waveguides we can calculate the coupling simply as

$$\sigma(\omega) = \frac{\Delta k(\omega)}{2}. \quad (1.5)$$

We performed this calculation using a numerical software (LUMERICAL MODE SOLVER) to simulate the modes supported by two parallel waveguides, and since our investigation on the effects of disorder involves the modification of the gaps, we repeat the simulation for different gap distances using (1.5) each time to recover the value of σ . In Fig. 1.3 (a) we show the results of the simulations for two silicon waveguides sampled at different gaps d using the TE0 mode at $\lambda = 1550$ nm. To fit the data points we rely again on the coupled wave analysis applied to a pair of waveguides in a perturbative approach. In this framework the presence of one waveguide slightly modifies the properties of the modes supported by the other, and one finds the exchange coupling coefficients σ_{21} describing the transfer of energy from the waveguide 1 to the waveguide 2 can be written as

$$\sigma_{21} \propto \int dx dz \mathbf{d}_2^*(x, z) \Delta \epsilon_2(x, z) \mathbf{d}_1(x, z), \quad (1.6)$$

Mode	A (μm^{-1})	κ (nm^{-1})
TE0 (silicon)	$(2.12 \pm 0.02) \times 10^{-1}$	$(8.91 \pm 0.05) \times 10^{-3}$
TE0 (LN)	$(1.93 \pm 0.02) \times 10^{-2}$	$(5.80 \pm 0.04) \times 10^{-3}$
TM2 (LN)	$(6.27 \pm 0.02) \times 10^{-2}$	$(1.261 \pm 0.001) \times 10^{-2}$

Table 1.1: Fitting parameters for the σ function of Eq. (1.7) approximating the trend showed in Fig. 1.3 for both structures.

where $\mathbf{d}_i(x, z)$ is the mode profile of the waveguide i and $\Delta\epsilon_2(x, z)$ is equal to the material ϵ in the space occupied by the waveguide 2 and 0 elsewhere. Approximating the mode profiles as $d_i(x, z) = h_i(z)g_i(x)$, where we also dropped the vectorial nature of the field for simplicity, and considering that $g_i(x)$ decays exponentially outside the waveguide i , we can write σ_{21} as

$$\sigma_{21}(d) \propto A \exp(-\kappa d), \quad (1.7)$$

for two waveguides separated by a gap d , which is the fitting function that we use in Fig. 1.3 (a-c) with A and κ the two fitting parameters. We note that this function reproduces correctly the physics of a null coupling at an infinite distance between the waveguides. In Fig. 1.3 (b) we show the field distribution resulting from the coupling of the waveguides for a gap distance $d_S = 173$ nm, and one can easily see that it closely resemble the superposition of the two TE0 modes centered on the respective waveguides, demonstrating that our approximation of Eq. (1.1) is valid around this range of short gaps. In Fig. 1.3 (c) we report the results of the same simulation performed on two LN waveguides at different gaps d for both TE0 and TM2 modes at wavelengths $\lambda = 1550$ nm and $\lambda = 775$ nm, respectively. In this case the data and the fitting function (1.7) are represented on a semi-logarithmic scale to better show the different confinement of the respective modes, which we expect to display a different behaviour in the formation of the topological mode. The validity of (1.1) holds also in this case as we show in Fig. 1.3 (d-e) for the TE0 and TM2 fields distribution resulting from the coupling of the waveguides at a distance $d_S = 300$ nm. The fitting parameters A and κ are reported in Table 1.1 for the three cases.

So far we have ignored the frequency dependence of the coupling coefficients, focusing only on their variation as a function of the gap length. In general this is a reasonable approximation if we study SFWM and SPDC within small bandwidths of photon pair generation. However in our investigation of the LN array we also want to know how σ_{21} is modified in a small range of frequencies around $\lambda = 1550$ nm and $\lambda = 775$ nm for a fixed gap length. Therefore, instead of building a 2-dimensional map that takes into

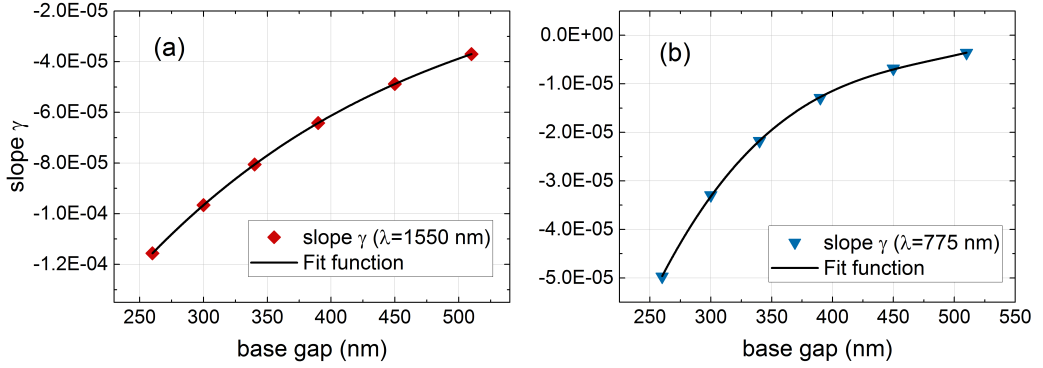


Figure 1.4: Slope γ of Eq. (1.8) as a function of the gap between two LN waveguides for (a) the TE0 mode and (b) the TM2 mode. The data is interpolated with a 3rd-order polynomial.

account both the frequency and the gap distance at the same time, we follow an approach that takes advantage of the results already obtained for the gap length. Because the bandwidths considered in this work are small, we expand in a Taylor series the function $\sigma_{21}(\nu)$ to the first order around the center frequencies as

$$\sigma_{21}(d, \nu) = \sigma_{21, \nu_0}(d) + \gamma_{\nu_0}(d) (\nu - \nu_0), \quad (1.8)$$

where $\sigma_{21}(d)_{\nu_0}$ is the coupling coefficient calculated using Eq. (1.7) and the slope $\gamma(d)$ is sampled at different gap lengths using the same numerical simulations as before. The data points are interpolated with a 3rd-order polynomial function as shown in Fig. 1.4

$$\gamma(x) = b_0 + b_1 x + b_2 x^2 + b_3 x^3, \quad (1.9)$$

and the fitting coefficients b_n are reported in Table 1.2.

Now that we have presented the methods to calculate $\sigma_{i,i+1}$ for every situation, we proceed by solving the system of linear differential equations in 1.3 using the unperturbed gap lengths d_S and d_L for the two structures in order to find the supported modes. To do so we rewrite the system in a matrix form

$$\frac{d}{dy} \mathbf{c}(y) = -i \mathbf{\Sigma} \mathbf{c}(y), \quad (1.10)$$

where we define a vector of coefficients

$$\mathbf{c}(y) = [c_1(y), \dots, c_N(y)]^T, \quad (1.11)$$

b_n (THz ⁻¹ nm ⁻ⁿ)	TE0 (LN)	TM2 (LN)
b_0	$(-3.38 \pm 0.03) \times 10^{-4}$	$(-3.5 \pm 0.1) \times 10^{-4}$
b_1	$(1.26 \pm 0.02) \times 10^{-6}$	$(2.0 \pm 0.1) \times 10^{-6}$
b_2	$(-1.81 \pm 0.06) \times 10^{-9}$	$(-4.0 \pm 0.3) \times 10^{-9}$
b_3	$(9.8 \pm 0.5) \times 10^{-13}$	$(2.8 \pm 0.3) \times 10^{-12}$

Table 1.2: Fitting parameters for the γ function of Eq. (1.9) approximating the trend showed in Fig. 1.4 for the LN array.

and Σ is a particular tridiagonal matrix

$$\Sigma = \begin{bmatrix} 0 & \sigma_S & 0 & \dots & 0 \\ \sigma_S & 0 & \sigma_L & \ddots & \vdots \\ 0 & \sigma_L & \ddots & \ddots & 0 \\ \vdots & \ddots & \ddots & 0 & \sigma_S \\ 0 & \dots & 0 & \sigma_S & 0 \end{bmatrix} \quad (1.12)$$

with null elements on the main diagonal, and the entries on the two minor diagonals are the coupling constants σ_S and σ_L corresponding to the distances d_S and d_L , respectively. In this form the equations are still coupled so we diagonalize Σ to find its eigenvalues λ_i and eigenvectors \mathbf{s}_i , which correspond to the propagation constants of the modes and their field distribution over the waveguides of the array, respectively. Then, the original matrix Σ can be decomposed as $\Sigma = \mathbf{S}\mathbf{\Lambda}\mathbf{S}^{-1}$ where $\mathbf{\Lambda}$ is a diagonal matrix containing the eigenvalues λ_i and the columns of \mathbf{S} are the eigenvectors. Defining a new vector of coefficients $\bar{\mathbf{c}}(y) = \mathbf{S}^{-1}\mathbf{c}(y)$, the system becomes

$$\frac{d}{dy}\bar{\mathbf{c}}(y) = -i\mathbf{\Lambda}\bar{\mathbf{c}}(y), \quad (1.13)$$

where the equations are now uncoupled and one can find immediately the solution as

$$\mathbf{c}(y) = \mathbf{S} \exp[-i\mathbf{\Lambda}y] \mathbf{S}^{-1} \mathbf{c}(0), \quad (1.14)$$

where the elements of the diagonal matrix $\exp[-i\mathbf{\Lambda}y]$ are $\exp(-i\lambda_i y) \delta_{ij}$. Using Eq. (1.14) together with (1.1) gives a complete description of the field propagation in the waveguide array given an initial amplitude distribution $\mathbf{c}(0)$. Moreover, the matrix \mathbf{S} and its inverse \mathbf{S}^{-1} provide a simple way to move from the base of orthogonal single waveguide modes to the base of the supermodes supported by the structure, and viceversa. Depending on the problem under investigation one can conveniently use either base.

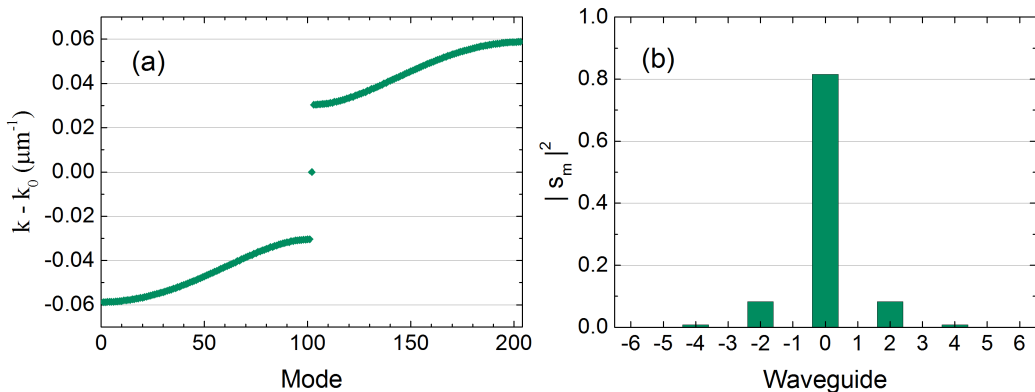


Figure 1.5: (a) Distribution of the eigenvalues of the matrix Σ representing the propagation constant of the modes. At the center of the gap the topological mode propagating with $k = k_0$. (b) Mode distribution of the topological mode with the characteristic null amplitude on the odd waveguides around the defect.

Now we turn our attention on the topological modes supported by the two structures, which can be found by diagonalizing their respective coupling matrix (1.12). In the case of the silicon waveguide array we introduced only a single topological defect, so we expect to find only a single supported topological mode. In Fig. 1.5 (a) we show the eigenvalues of the matrix, which represent the propagation constants of all the supported modes expressed as a shift from the propagation constant k_0 of the isolated silicon waveguide. As expected, the introduction of a defect in the otherwise perfectly periodical array splits the band of supported modes in two bands separated by a gap. At the center of the band gap the guided mode created by the topological defect has a propagation constant equal to k_0 and its field distribution is shown in Fig. 1.5 (b). The topological mode is localized around the defect waveguide, here labelled with the index 0, and its amplitude decreases exponentially with distance. A peculiar property of this mode is the amplitude equal to zero in the odd waveguides which, together with the value $k = k_0$ of the propagation constant, represents a topologically protected property.

The same analysis can be repeated for the LN waveguide array, but in this case there are two topological defects separated by a small number of waveguides, so we expect to find two topologically protected modes. In Fig. 1.6 (a) we show the propagation constants of the supported modes both at $\lambda = 1550 \text{ nm}$ (red) and $\lambda = 775 \text{ nm}$ (blue). As in the previous case the continuous band of guided modes is split in two bands separated by a band gap, and the width of both the gap and the bands increases with the

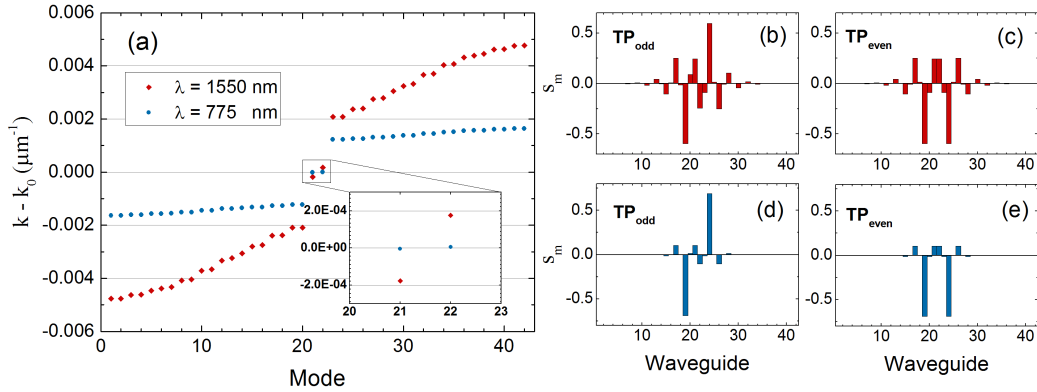


Figure 1.6: (a) Distribution of the propagation constants of the array modes for the TE0 and TM2 modes. At the center of the gap the two coupled topological modes. Field distribution of the odd (b) and even (c) topological modes at $\lambda = 1550$ nm and (d-e) at $\lambda = 775$ nm.

strength of the coupling constants between adjacent waveguides, which is larger (see Fig. 1.3) at $\lambda = 1550$ nm, where the TE0 mode is less confined, compared to the TM2 mode at $\lambda = 775$ nm. At the center of the gap we find the propagation constants of the two topological modes, but in this case their value is not exactly equal to k_0 and instead they are symmetrically split around this value because of their strong coupling. The effect is more evident at $\lambda = 1550$ nm as it depends on the spatial extension of the modes around the defect waveguides, which is determined by the TE0 mode confinement. The strong coupling produces also an effect on the symmetry of their field distribution, resulting in two modes with odd and even symmetry for both wavelengths as shown in Fig. 1.6 (b-c) and (d-e), respectively. In this case we also note that the two topological modes arising from the strong coupling don't display the same property of having a null field in the odd waveguides around the defects, which was characteristic of the isolated topological mode.

1.3 DISORDER AND TOPOLOGICAL PROTECTION

Our work revolves around the idea of that the topological nature of the modes created in these structures protects the properties of propagating light in the presence of disorder. It is important though to clarify what kind of disorder we are going to introduce, and what instead is not meant to be tested here. The type of disorder we are going to study is of *positional* nature,

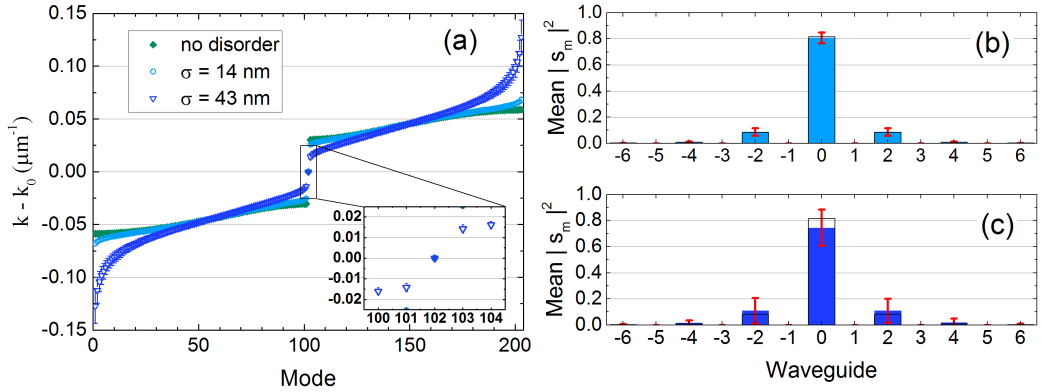


Figure 1.7: (a) Distribution of the eigenvalues with two significant levels of disorder. The propagation constant of the topological mode is protected against disorder. Field distribution of the topological mode with (b) $\sigma = 14$ nm and (c) $\sigma = 43$ nm disorder. The mode symmetry is protected against disorder.

which means that it affects the relative distance between the waveguides of the array and thus modifies the original gap distances d_S and d_L and the corresponding coupling constants σ_S and σ_L according to Eq. (1.7). Other types of disorder exist and could also be studied in principle, for example one that affects the geometry of the waveguides, but in this case it would be much more time-consuming to implement and it would not fit into the SSH model as it represents a modification of the array structure comparable to the substitution of the atoms in the molecule chain with other species. Moreover, we recall that the topological protection under investigation can be effective only against a kind of disorder that is on the same scale of the structure features responsible for the formation of the topological mode. This means that losses associated to Rayleigh scattering due to the roughness of the waveguide sidewalls, which work at the nanometer scale, will always be present and can be mitigated only by refining the fabrication processes.

To introduce the positional disorder we modify the relative position of the waveguides in the original structure by an amount that follows a Gaussian distribution with a mean $\mu = 0$ and a standard deviation σ that can range from 0 to 43 nm in the case of the silicon array and from 0 to 40 nm in the LN array. In the first case, since we take the experimental work by Blanco-Redondo et al. [17] as a reference, the values of $\sigma = 14$ nm and $\sigma = 43$ nm are of particular importance for comparison. In our study we compare the properties of the unperturbed structures with those affected by disorder, and this analysis is done by considering an appropriate number N_σ

of realizations for each level of disorder. We verified that, in the study of the linear properties of the topological modes, which is the focus of this chapter, the ensemble size $N_\sigma = 300$ is sufficient to obtain statistically meaningful results up to the maximum value of σ . This means that the calculated quantities in our statistical analysis are at convergence and do not require larger ensembles. These results constitute an important reference to which we will compare analogous quantities obtained in the following chapters, for the nonlinear regime of photon pair generation.

We start by commenting the results for the silicon array. In Fig. 1.7 (a) we show the propagation constants of the modes found for the unperturbed structure [Fig. 1.5 (a)] along with the average values obtained for $\sigma = 14$ nm and $\sigma = 43$ nm of disorder. In all the three cases one can observe that the major features of the distribution are preserved, with two bands separated by a gap containing the topological mode. When disorder is absent, the width of the gap is maximum, and the propagation constants are symmetrically distributed with respect to that of the topological mode. When disorder is introduced, the propagation constant of the topological mode is unchanged and continue to have the value k_0 as expected from topological protection and in agreement with [17]. Moreover, we note that this value doesn't oscillate, as shown in the inset of Fig. 1.7 (a) by the zero variance of the data point. On the contrary, the bands associated with the other modes are distorted and the gap is progressively reduced as disorder increases, as can be clearly seen in the case with $\sigma = 43$ nm where this effect is more pronounced.

Beside the protection of the topological mode propagation constant, it is important to verify whether the mode profile, which is contained in the associated eigenvector, is also stable with disorder. In Fig. 1.7 (b-c) we show the average of each eigenvector component for $\sigma = 14$ nm and $\sigma = 43$ nm of disorder, along with the values corresponding to the unperturbed structure (black frame). It is clear from the figure that even for $\sigma = 43$ nm the symmetry of the mode is well protected, with light confined only in the even waveguides. However, for large values of disorder the intensity distribution in these waveguides can vary significantly, as indicated by the large standard deviations in Fig. 1.7(c).

The case of the LN waveguide array is a bit different. Here, as we stressed above, there are two topological modes that are strongly coupled and we can't recognize the features observed for the isolated topological mode in terms of propagation constants and field distribution, which nonetheless would still be present if the two defects were created far enough from each other. Without loss of generality, we study the linear properties of the topological mode with odd symmetry (the even one being similar) and in Fig. 1.8 (a) we show the trend of its propagation constant both at $\lambda = 1550$ nm and $\lambda = 775$ nm.

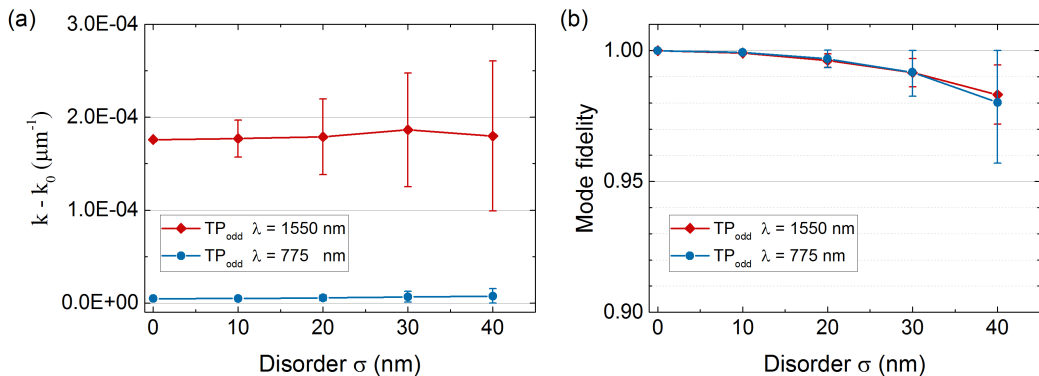


Figure 1.8: (a) Topological modes propagation constant as a function of disorder, the increasing variance is due to the varying coupling strength. (b) Field distribution fidelity showing strong robustness against disorder.

The average values are constant with increasing levels of disorder, confirming that they are topologically protected compared to the other modes, for which disorder introduce a distortion of the bands and thus of their average value, as shown for the other structure in Fig. 1.7 (a). The increasing variance of the average propagation constants is determined by the degree of coupling between the two topological modes, since disorder can move them closer or further to each other depending on the modification of the gaps between the waveguides separating them. In Fig. 1.8 (b) we show the average fidelity of the mode profile with the unperturbed one, computed as

$$\sum_m s_{m,0}^* s_{m,\sigma}, \quad (1.15)$$

where $s_{m,0}$ and $s_{m,\sigma}$ are the components of the eigenvector associated with the odd topological mode in the case of the unperturbed structure and with disorder σ , respectively. Here we see that the average fidelity is in general very high and decreases for large levels of disorder due to the significant variation of the field distribution. This was observed also for the isolated mode but in this case the mode coupling also contributes to this effect.

2 ELEMENTS OF QUANTUM NONLINEAR PHOTONICS

The study of light propagation in a medium deals with an optical regime in which the material interaction with the electric field of the light wave is *linear*, regardless the underlying description which can be either classical or quantum mechanical. This means that the macroscopic polarization of the medium $\mathbf{P}(\mathbf{r}, t)$, which describes the volume-averaged response of the material to the incident field $\mathbf{E}(\mathbf{r}, t)$, is proportional to it and oscillates at the same frequency. Thus, light is emitted without altering the spectral composition of the original light beam, but only its propagation direction.

Indeed, since $\mathbf{P}(\mathbf{r}, t)$ can be regarded as a source of the electric field in the Maxwell equations, it is clear that this physical quantity is associated also to the nonlinear optical processes responsible for the generation of light at new frequencies. The nonlinear terms proportional to higher orders of $\mathbf{E}(\mathbf{r}, t)$ arise from the nonlinear response of the material, which can be quite complicated to describe. To prove this point without unnecessary complications, we can resort to a demonstration based on the Lorentz model of the atom [28], which is a simple classical example that can help to clarify how these nonlinear terms appear. The linear version of this model describes a classical system in which one electron bound to the atom is treated as a damped oscillator in the presence of a driving force, which is provided by the external electric field. The restoring force exerted by the atom is a linear function of the electron displacement x from its equilibrium position and under this condition the steady-state solution for x is oscillating with the frequency of the field. If we allow the restoring force to include terms proportional to the second and third power of x , then it is possible to show in a perturbative approach that there are solutions for x proportional to higher powers of the driving electric field, and thus oscillate at frequencies that differ from that of the field. The physical nature of the material nonlinear response has its origin in the non-harmonic form of the true potential in which the electrons move. However we note that this is a simplified view since in general the

material response is a complicated function of the electric field and should take into account also their vector nature.

2.1 NONLINEAR OPTICAL PROCESSES

If the electric field is strong enough but not extremely intense, we can expand the macroscopic polarization $\mathbf{P}(\mathbf{r}, t)$ inside the material in a Taylor series as

$$P_i(\mathbf{r}, t) = \epsilon_0 \left\{ \chi_1^{ij} E_j(\mathbf{r}, t) + \chi_2^{ijk} E_j(\mathbf{r}, t) E_k(\mathbf{r}, t) + \chi_3^{ijkl} E_j(\mathbf{r}, t) E_k(\mathbf{r}, t) E_l(\mathbf{r}, t) + \dots \right\}, \quad (2.1)$$

where χ_1^{ij} is the usual linear susceptibility tensor with values in the order of unity or 10^1 , while χ_2^{ijk} and χ_3^{ijkl} are the second and third order nonlinear susceptibility tensors, respectively. These terms are at the base of the classical and quantum nonlinear processes that we discuss in this chapter and their typical values are in the range of $10^{-12} - 10^{-11}$ m/V for χ_2 and $10^{-22} - 10^{-18}$ m²/V² for χ_3 , which are orders of magnitude smaller than the linear response of the medium, suggesting that the nonlinear effects are much more attenuated and require strong light intensities to be observed. Large fields are typically achieved using laser beams as strong light sources, and further enhancement can be obtained by confining light spatially in the guided modes of waveguide structure, and temporally using resonant structures. Since we only study structures composed of waveguides, in our case the field enhancement comes only from the confinement in the guiding material due to total internal reflection, which is responsible for the formation of discrete modes when the waveguide section has dimensions comparable with the wavelength of light. Finally, concerning the materials considered in our work, we note that silicon is a typical material of integrated optics that has a fairly strong χ_3 but, since in its crystalline form it has a center-symmetric unitary cell with a strong symmetry, in the dipole approximation (long wavelengths) its second order tensor χ_2 is null. In contrast, lithium niobate has a unitary cell which is not center-symmetric and thus it displays a very strong χ_2 (4.5×10^{-12} m/V for our choice of the tensor element), typically exploited for photon pairs generation at the optical frequencies and for fast electro-optic modulation in the GHz range. Its χ_3 is also comparable to that of silicon and is exploited for frequency comb generation in ring resonators.

There is a broad variety of processes that can take place when the nonlinear response of the material is taken into account, and their effect depends on the order of the nonlinearity. However, integrated structures are typically

designed to favour only one of them due to energy and momentum conservation constraints. Here we briefly present the most relevant classical processes associated with the second and third order nonlinearity, namely *difference frequency generation* (DFG) and *four wave mixing* (FWM), respectively. We also motivate why classical fields can't describe what is observed in these processes under particular conditions, and why a quantum mechanical treatment of the electromagnetic field is necessary.

The DFG process can be described as arising from the χ_2 material response to the presence of a *pump* field at a frequency ω_P and a *seed* field at frequency ω_S . The result of the light-matter interaction is the appearance of a third field oscillating at an *idler* frequency ω_I , which is equal to $\omega_P - \omega_S$ because of energy conservation. In the FWM process driven by the χ_3 material response, two pump fields at a frequency ω_P and a seed field at frequency ω_S interact with the material and a third field at a frequency $\omega_I = 2\omega_P - \omega_S$ is generated. We note that in both cases if the pump and seed fields can be considered as monochromatic then the idler frequency is fixed by energy conservation, while the momentum conservation determines the efficiency of the process. We observe that, besides the pump field, there is always a seed field that stimulates the generation of the idler field, and indeed this is how we view these nonlinear processes within *classical electromagnetism*: a pump field produces a macroscopic polarization of the medium oscillating at the same frequency ω_P and the presence of the seed field modulates this polarization creating dipoles that oscillate at a new frequency ω_I . In this sense we identify these processes as being *stimulated*. Problems with the classical description of the fields arise when we remove the seed field for we continue to see the generation of new harmonic components, although with a different behaviour, at frequencies that can't be obtained by combining the frequencies of the classical pump fields. These new processes require a quantum mechanical description of the fields that involves the generation and destruction of *photons*, the elementary quantum excitation of the electromagnetic field, and are regarded as *spontaneous* since they don't require a stimulating field.

Before describing the quantum processes associated to DFG and FWM we recast Eq. (2.1) in terms of the electric displacement field $\mathbf{D}(\mathbf{r}, t)$, which is taken as our fundamental field [27]. We have

$$P_i(\mathbf{r}, t) = \Gamma_1^{ij}(\mathbf{r})D_j(\mathbf{r}, t) + \Gamma_2^{ijk}(\mathbf{r})D_j(\mathbf{r}, t)D_k(\mathbf{r}, t) + \Gamma_3^{ijkl}(\mathbf{r})D_j(\mathbf{r}, t)D_k(\mathbf{r}, t)D_l(\mathbf{r}, t) + \dots, \quad (2.2)$$

where the linear and nonlinear Γ 's response functions are related to the old

χ 's using the constitutive equation

$$\mathbf{D}(\mathbf{r}, t) = \epsilon_0 \mathbf{E}(\mathbf{r}, t) + \mathbf{P}(\mathbf{r}, t). \quad (2.3)$$

Here we have taken the Γ 's dependent on the position \mathbf{r} to allow for inhomogeneous dielectric structures, however the response is considered local both in space and time thus neglecting dispersion [29]. Under these conditions the tensors are invariant under permutation of the Cartesian indexes and one can build the total energy of the electromagnetic field [30] as

$$\begin{aligned} E = E_0 - \frac{1}{3\epsilon_0} \int d\mathbf{r} \Gamma_2^{ijk}(\mathbf{r}) D_i(\mathbf{r}, t) D_j(\mathbf{r}, t) D_k(\mathbf{r}, t) \\ - \frac{1}{4\epsilon_0} \int d\mathbf{r} \Gamma_3^{ijkl}(\mathbf{r}) D_i(\mathbf{r}, t) D_j(\mathbf{r}, t) D_k(\mathbf{r}, t) D_l(\mathbf{r}, t), \end{aligned} \quad (2.4)$$

where E_0 contains the energy of the linear part and we highlighted the second and third order nonlinear contributions. We now consider a simple structure like an isolated waveguide supporting a single propagating mode and we proceed to quantize the electric displacement field, introducing our field operator in the Schrödinger picture as

$$\mathbf{D}(\mathbf{r}) = \int_{-\infty}^{\infty} dk \sqrt{\frac{\hbar\omega_k}{2}} c_k \mathbf{D}_k(\mathbf{r}) + \text{H.c.}, \quad (2.5)$$

where H.c. stands for 'Hermitian conjugate', the operators c_k and c_k^\dagger destroy and create, respectively, a photon of energy $\hbar\omega_k$ in the radiation mode with wavevector k , and satisfy the canonical commutation relations

$$\begin{aligned} [c_k, c_{k'}] &= 0, \\ [c_k, c_{k'}^\dagger] &= \delta(k - k'). \end{aligned} \quad (2.6)$$

The mode fields $\mathbf{D}_k(\mathbf{r})$ at k and $-k$ are not independent but are related by

$$\mathbf{D}_{-k}(\mathbf{r}) = [\mathbf{D}_k(\mathbf{r})]^*, \quad (2.7)$$

and considering the waveguide extending along the y direction one can write the mode fields as

$$\mathbf{D}_k(\mathbf{r}) = \frac{\mathbf{d}_k(x, z)}{\sqrt{2\pi}} e^{iky}. \quad (2.8)$$

Using the quantized field (2.5) with (2.8) in place of the classical fields in the nonlinear terms of (2.4), we obtain the corresponding terms of the Hamiltonian describing the nonlinear light-matter interaction. In particular, the

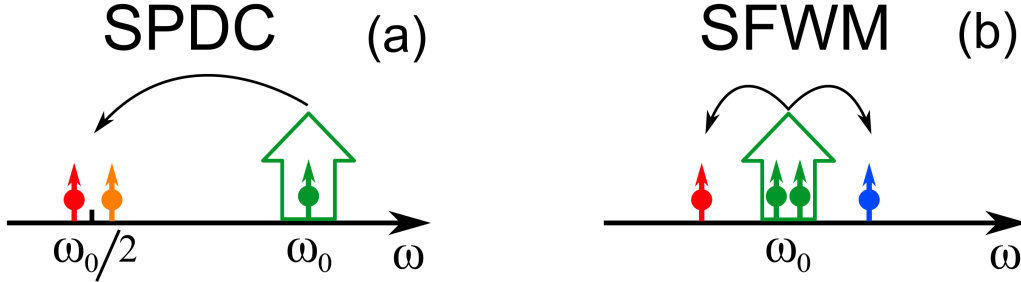


Figure 2.1: (a) SPDC process: a photon from a strong pump at ω_0 is destroyed and two photons are created over a bandwidth around $\omega_0/2$. (b) SFWM process: two photons from a strong pump at ω_0 are destroyed and two photons are created over a bandwidth around the same frequency.

two quantum processes associated to DFG and FWM that can only be described in terms of the creation and destruction operators are the *spontaneous parametric down-conversion* (SPDC) and the *spontaneous four-wave mixing* (SFWM), respectively.

The nonlinear Hamiltonian associated to the SPDC process is

$$H_{\text{NL}} = - \int dk_1 dk_2 dk S(k_1, k_2, k) c_{k_1}^\dagger c_{k_2}^\dagger c_k + \text{H.c.}, \quad (2.9)$$

and as we show in Fig. 2.1 (a) this process involves the destruction of a photon from a strong pump centered at a frequency ω_0 in the mode k and creates two photons at energies symmetrically positioned around $\omega_0/2$ in the modes k_1 and k_2 . Compared to the stimulated (classical) process, here the energy of the two generated photons is not fixed and because of energy conservation they can be created in principle from $\omega = 0$ to ω_0 . However, chromatic dispersion limits this process to a bandwidth that depends on how well the phase matching condition satisfies momentum conservation. The nonlinear coupling term $S(k_1, k_2, k)$ can be written as

$$S(k_1, k_2, k) = \sqrt{\frac{(\hbar\omega_{k_1})(\hbar\omega_{k_2})(\hbar\omega_k)}{(4\pi)^3 \epsilon_0} \frac{\bar{\chi}_2}{\bar{n}^3} \frac{e^{i\nu(k_1, k_2, k)}}{\sqrt{\mathcal{A}(k_1, k_2, k)}}} \times \int_0^L dy e^{i(k-k_1-k_2)y} \quad (2.10)$$

where

$$\frac{e^{i\nu(k_1, k_2, k)}}{\sqrt{\mathcal{A}(k_1, k_2, k)}} = \int dx dz \frac{\bar{n}^3 \chi_2^{ijk}(x, z) [d_{k_1}^i(x, z)]^* [d_{k_2}^j(x, z)]^* d_k^k(x, z)}{\epsilon_0^{3/2} \bar{\chi}_2 n_{k_1}^2(x, z) n_{k_2}^2(x, z) n_k^2(x, z)}, \quad (2.11)$$

and $\mathcal{A}(k_1, k_2, k)$ with units of an area is positive real and can be considered as an effective area of the nonlinear interaction of the field modes. The phase $\nu(k_1, k_2, k)$ is real, $\bar{\chi}_2$ and \bar{n} are typical values of the second order nonlinearity and local refractive index, respectively. Here as we mentioned previously, we used the relation

$$\Gamma_2^{ijk} \rightarrow \frac{\chi_2^{ijk}}{\epsilon_0 n_{k_1}^2 n_{k_2}^2 n_k^2}. \quad (2.12)$$

The integral in y over the waveguide length contains the phase matching term $(k - k_1 - k_2)$ for the SPDC process and integrating the phase one gets a factor proportional to

$$L \text{sinc} \{(k - k_1 - k_2)L/2\}, \quad (2.13)$$

with $\text{sinc}(x) = \sin(x)/x$, which leads to a generation efficiency of the SPDC process that scales with L^2 and $\text{sinc}^2\{(k - k_1 - k_2)L/2\}$ if we consider only the photons generated within a small bandwidth, as it is always throughout our work. In general one typically expands the wavevectors around $\omega_m = \omega_0$ and $k_m = k_0/2$ as

$$k = k(\omega_m) + \frac{1}{v_g(\omega_m)}(\omega - \omega_m) + \frac{\beta_2(\omega_m)}{2}(\omega - \omega_m)^2, \quad (2.14)$$

where v_g is the group velocity and β_2 is the group velocity dispersion. If we consider the generation of photon pairs over all the allowed frequencies then, assuming a pump strongly peaked around ω_0 approaching the continuous wave (CW) limit, the generation bandwidth is limited by $\beta_2(\omega_0/2)$ and the process efficiency scales with $L^{3/2}$ [31].

The nonlinear Hamiltonian associated to the SFWM process is

$$H_{\text{NL}} = - \int dk_1 dk_2 dk_3 dk_4 S(k_1, k_2, k_3, k_4) c_{k_1}^\dagger c_{k_2}^\dagger c_{k_3} c_{k_4} + \text{H.c.}, \quad (2.15)$$

and as we show in Fig. 2.1 (b) this process involves the destruction of two photons from a strong pump centered at a frequency ω_0 in the modes k_3 and k_4 and creates two photons at energies symmetrically positioned around ω_0 in the modes k_1 and k_2 , which can be effectively seen as a perfectly elastic scattering of two photons. As in the case of SPDC, in SFWM the energy of the two generated photons is not fixed compared to the stimulated (classical) process, and because of energy conservation they can be created in principle from $\omega = 0$ to $2\omega_0$. However, also here chromatic dispersion limits the process to a bandwidth that depends on the phase matching condition satisfying

momentum conservation. The nonlinear coupling term $S(k_1, k_2, k_3, k_4)$ can be written as

$$S(k_1, k_2, k_3, k_4) = \frac{3}{2} \sqrt{\frac{(\hbar\omega_{k_1})(\hbar\omega_{k_2})(\hbar\omega_{k_3})(\hbar\omega_{k_4})\bar{\chi}_3}{(4\pi)^4\epsilon_0^2\bar{n}^4}} \times \frac{e^{i\nu(k_1, k_2, k_3, k_4)}}{\mathcal{A}(k_1, k_2, k_3, k_4)} \int_0^L dy e^{i(k_3+k_4-k_1-k_2)y} \quad (2.16)$$

and

$$\frac{e^{i\nu(k_1, k_2, k_3, k_4)}}{\mathcal{A}(k_1, k_2, k_3, k_4)} = \int dx dz \frac{\bar{n}^4 \chi_3^{ijkl}(x, z)}{\bar{\chi}_3} \times \frac{[d_{k_1}^i(x, z)]^* [d_{k_2}^j(x, z)]^* d_{k_3}^k(x, z) d_{k_4}^l(x, z)}{\epsilon_0^2 n_{k_1}^2(x, z) n_{k_2}^2(x, z) n_{k_3}^2(x, z) n_{k_4}^2(x, z)}, \quad (2.17)$$

is an effective area of the nonlinear interaction of the field modes, where also in this case we used the relation

$$\Gamma_3^{ijkl} \rightarrow \frac{\chi_3^{ijkl}}{\epsilon_0^2 n_{k_1}^2 n_{k_2}^2 n_{k_3}^2 n_{k_4}^2}. \quad (2.18)$$

The considerations we made for SPDC on the scaling of the process with the waveguide length and the phase matching also apply for SFWM, while the additional properties that distinguish the two processes will be visible later when the nonlinear Hamiltonian is used to calculate the quantum state of the generated photons.

2.2 THE ASYMPTOTIC FIELDS METHOD

So far we have used a simple structure, consisting of an isolated waveguide, to formulate a quantum mechanical treatment of the electromagnetic field and introduce the two quantum nonlinear processes of SPDC and SFWM. Although a waveguide is sufficient for this purpose, the growing interest in these quantum processes as reliable sources of entangled photons has led to the design of integrated photonic circuit of increasing dimension and complexity. These structure typically include many channel waveguides, that can be coupled to each other for the manipulation of both classical and quantum light, and one or more quantum sources where the nonlinear interaction takes place. These sources can be the waveguide channels themselves or resonating structures like cavities or micro-ring resonators, if the enhancement of the process is required. Even in the case of a simple structure such as a resonator

coupled to a channel waveguide, resorting to a fully quantum treatment of the electromagnetic field would require to consider a linear Hamiltonian describing the energy in the channel modes, in the resonator modes, and their coupling to account for the energy exchange. Then, depending on the process a nonlinear Hamiltonian term would be added to form the full Hamiltonian required for the time evolution of the quantum state

$$\begin{aligned} H_L &= H_{\text{channel}} + H_{\text{resonator}} + H_{\text{coupling}}, \\ H &= H_L + H_{\text{NL}}. \end{aligned} \tag{2.19}$$

This type of construction is referred to as the *Gardiner-Collett* Hamiltonian [15], however it is clear that extending this method to more complicated structure such as the waveguide arrays studied here would rapidly lead to a very large Hamiltonian that is difficult to deal with.

A different approach [32], that completely bypass the limits imposed by the large number of integrated optical elements, considers the whole dynamics of the electromagnetic field as a scattering problem in which the integrated structure acts as a scattering center. The idea take inspiration from the theory of scattering in quantum mechanics [33], where *asymptotic-in* and *asymptotic-out* states are constructed as full solutions of the linear Schrödinger equation that includes the scattering potential. The superposition of these solutions is such that they describe an incident wave packet at the asymptotic time $t = -\infty$ and an outgoing wave packet at the asymptotic time $t = \infty$. In a similar way the asymptotic field method introduces *asymptotic-in* and *asymptotic-out* fields that are full solution of the linear Maxwell equations and form a basis for the solutions of the nonlinear scattering problem. As shown in Fig. 2.2 we can idealize the nonlinear process as restricted to a well defined region connected with channels that bring energy in and out of it. In our specific case we consider the whole array as the nonlinear region with waveguides ideally extending out of it and treated as the channels of Fig. 2.2. The asymptotic-in and -out fields are constructed such that their superposition corresponds to an incoming and outgoing waves, respectively, with the field localized in one specific channel. At the same time the dynamic of coupling between the integrated elements and the energy stored in their modes is captured by the field distribution of the asymptotic fields.

We now briefly explain the main concepts of this method taking Fig. 2.2 as reference. The channels can be of any type supporting guided modes and identify all the possible "ways" in which energy moves in and out of the interaction region. To each channel we associate a local reference frame (x_n, y_n, z_n) directed towards the interaction region with $y_n = 0$ at the center

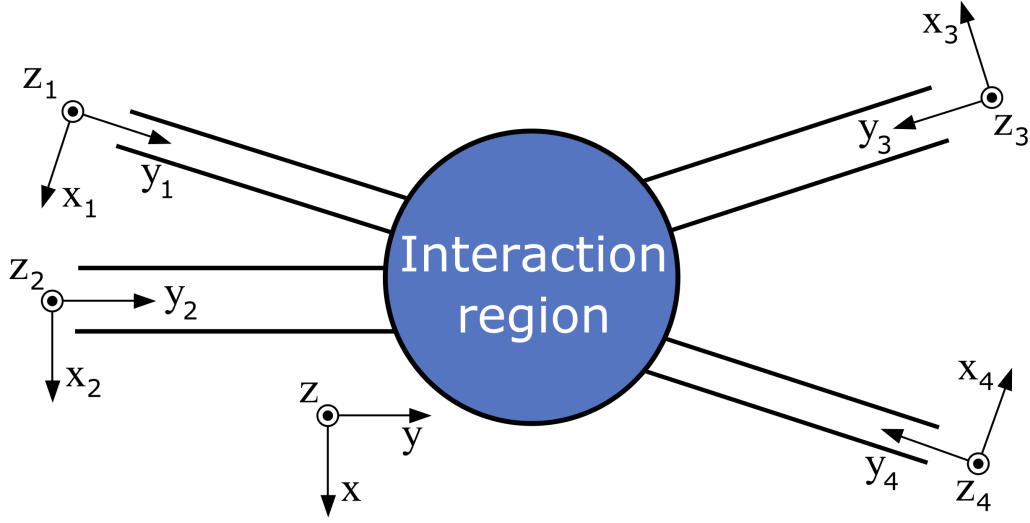


Figure 2.2: In the asymptotic field method the nonlinear interaction region, representing the structure under study, is connected by different channels with local reference frames in which energy can flow from and to the interaction region.

of the interaction region. It is assumed that functions expressed in these frames are truncated to 0 in the interaction region and further. The laboratory frame (x, y, z) is also centered in the interaction region. Assuming that the I modes supported by all the channels n are known, we express the quantized electric displacement field in the Schrödinger picture as

$$\mathbf{D}(\mathbf{r}) = \sum_{n,I} \int_{-\infty}^{\infty} dk \sqrt{\frac{\hbar\omega_{n,I,k}}{2}} c_{n,I,k} \mathbf{D}_{n,I,k}(\mathbf{r}) + \text{H.c.}, \quad (2.20)$$

and we note that in our case of a waveguide array the structure can be seen as composed of many channels formed by identical single waveguides with their supported modes (if more than one is supported) or as a single channel supporting n modes, which are essentially the supermodes of the structure calculated in Ch. 1 from the coupling matrix. The mode fields $\mathbf{D}_{n,I,k}(\mathbf{r})$ satisfy the same properties (2.7) and (2.8) and the similar relations to (2.6) apply for the operators $c_{n,I,k}$. We look for field modes solution of the Maxwell equation that, far from the interaction region, can be written in the form

$$\mathbf{D}_{n,I,k}^{asy-in}(\mathbf{r}) = \mathbf{D}_{n,I,k}(\mathbf{r}_n) + \mathbf{D}_{n,I,-k}^{out}(\mathbf{r}_n), \quad (2.21)$$

where the second term, for positive k , is

$$\mathcal{D}_{n,I,-k}^{out}(\mathbf{r}_n) = \sum_{n',I'} \int_0^\infty dk' T_{n,I;n',I'}^{out}(k, k') \mathbf{D}_{n',I',-k'}(\mathbf{r}_{n'}) \quad (2.22)$$

and the functions $T_{n,n'}^{out}(k, k')$ are same-frequency coupling terms that connect the different channels. The mode fields $\mathbf{D}_{n,I,k}^{asy-in}(\mathbf{r})$ are the *asymptotic-in mode fields* corresponding to incoming wave in the channel n and outgoing waves in all the n' channels, such that a superposition of them corresponds to field modes propagating towards the interaction region and positioned away from it at times $t \ll 0$, when the contributions from $\mathcal{D}_{n,I,-k}^{out}(\mathbf{r}_n)$ cancel out because of destructive interference. At times $t \gg 0$ the field modes $\mathbf{D}_{n,I,k}(\mathbf{r}_n)$ vanish and only the contributions $\mathcal{D}_{n,I,-k}^{out}(\mathbf{r}_n)$ remain, propagating away from the interaction region. A similar reasoning can be done introducing *asymptotic-out mode fields* written as

$$\mathbf{D}_{n,I,k}^{asy-out}(\mathbf{r}) = \mathbf{D}_{n,I,-k}(\mathbf{r}_n) + \mathcal{D}_{n,I,k}^{in}(\mathbf{r}_n), \quad (2.23)$$

where the second term, for positive k , is

$$\mathcal{D}_{n,I,k}^{in}(\mathbf{r}_n) = \sum_{n',I'} \int_0^\infty dk' T_{n,I;n',I'}^{in}(k, k') \mathbf{D}_{n',I',k'}(\mathbf{r}_{n'}), \quad (2.24)$$

with similar interpretation for the terms and the dynamics of the field modes. The two sets both form a base for the operator $\mathbf{D}(\mathbf{r})$, hence we can expand it in either one of the two forms.

$$\mathbf{D}(\mathbf{r}) = \sum_{n,I} \int_0^\infty dk \sqrt{\frac{\hbar\omega_{n,I,k}}{2}} a_{n,I,k} \mathbf{D}_{n,I,k}^{asy-in}(\mathbf{r}) + \text{H.c.}, \quad (2.25)$$

$$\mathbf{D}(\mathbf{r}) = \sum_{n,I} \int_0^\infty dk \sqrt{\frac{\hbar\omega_{n,I,k}}{2}} b_{n,I,k} \mathbf{D}_{n,I,k}^{asy-out}(\mathbf{r}) + \text{H.c.}, \quad (2.26)$$

where the operators $a_{n,I,k}, b_{n,I,k}$ and their adjoints follow similar relations to (2.6). These two sets aren't independent, as the following relations hold if we compare (2.21) and (2.23)

$$\begin{aligned} \mathbf{D}_{n,I,k}^{asy-out}(\mathbf{r}) &= [\mathbf{D}_{n,I,k}^{asy-in}(\mathbf{r})]^*, \\ T_{n,I;n',I'}^{in}(k, k') &= [T_{n,I;n',I'}^{out}(k, k')]^*. \end{aligned} \quad (2.27)$$

It is also possible to put the two sets in a direct relation using their property of completeness of the base as

$$\mathbf{D}_{n,I,k}^{asy-out}(\mathbf{r}) = \sum_{n',I'} \int_0^\infty dk' T_{n,I;n',I'}^{in}(k, k') \mathbf{D}_{n',I',k'}^{asy-in}(\mathbf{r}), \quad (2.28)$$

and similar relations follow for the destruction operators

$$\begin{aligned} a_{n,I,k} &= \sum_{n',I'} \int_0^\infty dk' T_{n,I;n',I'}^{in}(k, k') b_{n',I',k'} \\ b_{n,I,k} &= \sum_{n',I'} \int_0^\infty dk' T_{n,I;n',I'}^{out}(k, k') a_{n',I',k'}. \end{aligned} \quad (2.29)$$

2.3 THE BACKWARD HEISENBERG PICTURE FOR QUANTUM STATE EVOLUTION

Now that the problem of formulating an Hamiltonian treatment of the electromagnetic field in complex structure is solved with the use of the asymptotic field modes, we are left with an Hamiltonian consisting of only two terms: a linear part describing the propagation of energy in the photonic circuit and a nonlinear part describing either the SPDC or SFWM process. What we are left to do is describing the dynamical evolution of the quantum state of light under the action of this Hamiltonian, and the general idea is that at the end of the evolution we should be able to clearly identify a state describing the two photons generated by SPDC or SFWM. To perform this task we adopt an approach called *backward Heisenberg picture* [34].

Typically, when the nonlinear process is considered sufficiently weak such that there is only a very small probability of creating a pair of photons, the state of the generated light can be written, with good approximation as

$$|\psi\rangle = |\text{vac}\rangle + \beta C_{\text{II}}^\dagger |\text{vac}\rangle + \dots, \quad (2.30)$$

where $|\text{vac}\rangle$ is the vacuum state, C_{II}^\dagger is the operator that creates the two photons and is defined as

$$C_{\text{II}}^\dagger |\text{vac}\rangle = \frac{1}{\sqrt{2}} \int dk_1 dk_2 \phi(k_1, k_2) c_{k_1}^\dagger c_{k_2}^\dagger |\text{vac}\rangle, \quad (2.31)$$

with $\phi(k_1, k_2)$ the biphoton wave function (BWF), which captures the information related to the quantum correlation of the photons. The value $|\beta|^2$ is very small compared to unity when this approximation is valid, and can be considered by all means the probability of generating a pair. A generalization of this result to a regime where the excitation pump is stronger and multiple pairs can be generate, leads to a definition of the state $|\psi\rangle$ of the form

$$|\psi\rangle = e^{\beta C_{\text{II}}^\dagger - \text{H.c.}} |\text{vac}\rangle, \quad (2.32)$$

which remains valid as long as the amplitude of the pump is not excessively diminished by the generation of new photon pairs, in this case one assumes to be in the *undepleted pump approximation* and in this work we always consider it to be valid, since the structures investigated are not even resonant and the generation rate is comparable of that obtained in a waveguide. The method described here has the goal of calculating (2.32) as an approximate solution of the operator describing the excitation pump, relying on asymptotic-in and -out *states* to eliminate the trivial evolution of the initial state that occurs due to the linear part of the Hamiltonian. In the following we consider nonlinear Hamiltonian terms in the form (2.9) and (2.15), where field modes (2.8) are used, but it is clear from the previous section that asymptotic fields can be used in combination with this method depending on the complexity of the structure considered, and that is what we do in our work.

Using a reasoning similar to that of the asymptotic fields, we consider the nonlinear region to be delimited in space and imagine an input state $|\psi(t_0)\rangle$ for $t_0 \ll 0$ describing light incident towards it and electromagnetic energy localized far away of the region. What we seek to build is an output state $|\psi(t_1)\rangle$ for $t_1 \gg 0$ moving away from the region with energy also localized away from it. Following an approach typically used in scattering theory, we introduce the *asymptotic-in state* $|\psi_{in}\rangle$ that is obtained from the evolution of $|\psi(t_0)\rangle$ from $t = t_0$ to $t = 0$ under the linear Hamiltonian

$$|\psi_{in}\rangle = e^{-iH_L(0-t_0)/\hbar} |\psi(t_0)\rangle, \quad (2.33)$$

and similarly the *asymptotic-out state* $|\psi_{out}\rangle$ that evolves into the state $|\psi(t_1)\rangle$ from $t = 0$ to $t = t_1$ under the same linear Hamiltonian.

$$|\psi(t_1)\rangle = e^{-iH_L(t_1-0)/\hbar} |\psi_{out}\rangle. \quad (2.34)$$

The states $|\psi(t_1)\rangle$ and $|\psi(t_0)\rangle$ are of course related to each other through the time evolution under the full Hamiltonian of the system

$$|\psi(t_1)\rangle = e^{-iH(t_1-t_0)/\hbar} |\psi(t_0)\rangle, \quad (2.35)$$

and the three equations allow us to put in relation the asymptotic-in and -out states as

$$|\psi_{out}\rangle = U(t_1, t_0) |\psi_{in}\rangle, \quad (2.36)$$

where the operator U defined for two generic times t' and t is

$$U(t', t) = e^{iH_L t'/\hbar} e^{-iH(t'-t)/\hbar} e^{-iH_L t/\hbar}. \quad (2.37)$$

and its time evolution, from (2.37) is

$$-i\hbar \frac{\partial U(t', t)}{\partial t} = U(t', t) V(t), \quad (2.38)$$

with $U(t, t) = 1$ and $V(t)$ defined as

$$V(t) = e^{iH_L t/\hbar} H_{\text{NL}} e^{-iH_L t/\hbar}. \quad (2.39)$$

This approach, in which we study only the dynamics that leads from $|\psi_{\text{in}}\rangle$ to $|\psi_{\text{out}}\rangle$, allows us to neglect all the trivial linear evolution and focus on the nonlinear scattering problem. The method is very generic and the initial asymptotic state can be defined in a very generic way as

$$|\psi_{\text{in}}\rangle = f(\{O_i\}) |\text{vac}\rangle, \quad (2.40)$$

where $f(\{O_i\})$ is a generic function of a set of Schrödinger operators. In our case we will always consider the initial state to be a *coherent quantum state* in the form

$$|\psi_{\text{in}}\rangle = e^O |\text{vac}\rangle, \quad (2.41)$$

with O specified later in the text. Considering that the action of $U(t', t)$ and $U^\dagger(t', t)$ is unitary on the vacuum state we can recast (2.36) as

$$\begin{aligned} |\psi_{\text{out}}\rangle &= U(t_1, t_0) e^O U^\dagger(t_1, t_0) |\text{vac}\rangle \\ &= e^{U(t_1, t_0) O U^\dagger(t_1, t_0)} |\text{vac}\rangle \\ &= e^{\bar{O}(t_0)} |\text{vac}\rangle, \end{aligned} \quad (2.42)$$

where it is evident from the second line the definition of the operator $\bar{O}(t_0)$, which satisfies the final boundary condition $\bar{O}(t_1) = O$ and its time evolution is

$$i\hbar \frac{\partial \bar{O}(t)}{\partial t} = [\bar{O}(t), \hat{V}(t)], \quad (2.43)$$

with $\hat{V}(t) = U(t_1, t) V(t) U^\dagger(t_1, t)$. The next step consists in integrating the Heisenberg equation (2.43) from $t = t_1$ back to $t = t_0$ to express the output state (2.42) in the form of Eq. (2.32). To do so we first explicit the operator in Eq. (2.42) to represent a coherent state

$$O = \alpha A^\dagger - \text{H.c.}, \quad (2.44)$$

where $|\alpha|^2$ is the average number of photons in the incoming pulse, considered constant in the undepleted pump approximation adopted here, and the operator

$$A^\dagger = \int dk \phi_P(k) c_k^\dagger, \quad (2.45)$$

contains the amplitude $\phi_P(k)$ of the pump spectrum function, normalized as

$$\int dk |\phi_P(k)|^2 = 1, \quad (2.46)$$

with c_k^\dagger the usual creation operator. In Appendix we report the full calculation for both processes, where we also move from the space of wavevectors k to the space of positive frequencies ω , assuming that the pump pulse spectrum $\phi_P(k)$ is peaked enough around a value of k such that all the non-negligible values are positive. The asymptotic-out state can then be written as

$$|\psi_{\text{out}}\rangle = e^{\alpha A^\dagger - \text{H.c.}} |\psi_{\text{out}}\rangle_{\text{gen}}, \quad (2.47)$$

where we see that because of the undepleted pump approximation the operator describing the pump is unchanged, and $|\psi_{\text{out}}\rangle_{\text{gen}}$ is the state of the generated photons

$$|\psi_{\text{out}}\rangle_{\text{gen}} = e^{\beta C_{\text{II}}^\dagger - \text{H.c.}} |\text{vac}\rangle, \quad (2.48)$$

in which C_{II}^\dagger is the two-photon creator operator. When $|\beta|^2 \ll 1$ we can expand the exponential to the first order

$$|\psi_{\text{out}}\rangle_{\text{gen}} \approx |\text{vac}\rangle + \beta |\text{II}\rangle + \dots, \quad (2.49)$$

and now $|\beta|^2$ assumes the meaning of pair generation probability per pulse. Finally, the two-photon state $|\text{II}\rangle$ is

$$|\text{II}\rangle = \frac{1}{\sqrt{2}} \int_0^\infty d\omega_1 d\omega_2 \tilde{\phi}(\omega_1, \omega_2) \tilde{c}_{\omega_1}^\dagger \tilde{c}_{\omega_2}^\dagger |\text{vac}\rangle. \quad (2.50)$$

where the BWF $\tilde{\phi}(\omega_1, \omega_2)$ is normalized as

$$\int_0^\infty d\omega_1 \int_0^\infty d\omega_2 |\tilde{\phi}(\omega_1, \omega_2)|^2 = 1, \quad (2.51)$$

and $|\tilde{\phi}(\omega_1, \omega_2)|^2 d\omega_1 d\omega_2$ represents the probability of finding a photon pair with one photon generated about $\omega_1 + d\omega_1$ and the other about $\omega_2 + d\omega_2$. Depending on the process involved, the form of the BWF has some meaningful differences. In the case of SPDC we find

$$\begin{aligned} \tilde{\phi}(\omega_1, \omega_2) &= \frac{2\sqrt{2}i\pi\alpha}{\hbar\beta} \sqrt{\frac{dk(\omega_1)}{d\omega_1}} \sqrt{\frac{dk(\omega_2)}{d\omega_2}} \sqrt{\frac{dk(\omega_1 + \omega_2)}{d(\omega_1 + \omega_2)}} \\ &\times \phi_P(\omega_1 + \omega_2) S(\omega_1, \omega_2, \omega_1 + \omega_2), \end{aligned} \quad (2.52)$$

where

$$\frac{dk(\omega_i)}{d\omega_i} \equiv [v_g(\omega_i)]^{-1}, \quad (2.53)$$

are group velocities introduced in the Appendix. In the case of SFWM we find

$$\begin{aligned}
 \tilde{\phi}(\omega_1, \omega_2) &= \frac{2\sqrt{2}i\pi\alpha^2}{\hbar\beta} \sqrt{\frac{dk(\omega_1)}{d\omega_1}} \sqrt{\frac{dk(\omega_2)}{d\omega_2}} \\
 &\times \int_0^\infty d\omega \left\{ \sqrt{\frac{dk(\omega)}{d\omega}} \sqrt{\frac{dk(\omega_1 + \omega_2 - \omega)}{d(\omega_1 + \omega_2 - \omega)}} \right. \\
 &\left. \times \phi_P(\omega)\phi_P(\omega_1 + \omega_2 - \omega)S(\omega_1, \omega_2, \omega) \right\}, \tag{2.54}
 \end{aligned}$$

where we see that the BWF involves a convolution integral of the pump spectrum and since it is $\propto \alpha^2$ the SFWM process scales with $|\alpha|^4$, i.e with the square of the pump power, in contrast to the SPDC process which is linear in the pump power as it scales with $|\alpha|^2$.

In the presentation of the backward Heisenberg picture approach we used the two nonlinear Hamiltonian of Eq. (2.9) and (2.15) introduced for a single waveguide, but the method can be used in conjunction with the asymptotic fields to treat the generation of photon pairs in a more complicated structure. This is what we do in our work where we are interested in the generation of photon pairs in an array of N waveguides, and in general we will see that the two-photon state can be written in a more general way as

$$|\text{II}\rangle = \frac{1}{\sqrt{2}} \sum_{i,j} \int_0^\infty d\omega_1 d\omega_2 \tilde{\phi}_{i,j}(\omega_1, \omega_2) \tilde{c}_{i,\omega_1}^\dagger \tilde{c}_{j,\omega_2}^\dagger |\text{vac}\rangle, \tag{2.55}$$

where i and j run over all the waveguides and $\tilde{c}_{i,\omega_1}^\dagger$ is the operator that creates a photon in the waveguide i at a frequency ω_1 . One can also view the state (2.55) as having a BWF that is a coherent superposition of BWFs over all the (i, j) combinations. In general, considering that the structures we are investigating are formed by waveguides, we don't expect to observe a particularly different behaviour in the *spectral* properties of the BWF compared to that one can observe in a single waveguide. Most of our attention will be focused on the *path* properties of the BWF as they tell us from which waveguides the two photons will exit from the structure, and what quantum path correlations exist. Nevertheless we will report both properties in our works.

2.4 FIGURES OF MERIT

In our investigation of the topological protection of generated quantum light, we calculate the two-photon state (2.55) both for the unperturbed structure and for every realization in which disorder is introduced. Thus, it is very important to find quantitative methods to establish the effects of disorder on the properties of the two-photon state. In this way we can both compare the results with the linear properties described in Ch. 1 to establish if the topological protection is transferred to the generated photons, and track change of the state properties with increasing levels of disorder. To this end we consider some figures of merit that can be typically defined for quantum states.

We start by noting that in the backward Heisenberg picture we took as our initial (coherent) state a *pure* state. This is immediately clear by the simple fact that the state is defined as a *ket* state and not in a more general way as a density matrix. Further, the dynamical evolution under the nonlinear Hamiltonian produces the state (2.55), which is also obviously pure. Nevertheless one can certainly introduce for the two-photon state the corresponding *density matrix* defined as

$$\rho_{\text{II}} = |\text{II}\rangle \langle \text{II}|, \quad (2.56)$$

which is a positive defined operator with unitary trace

$$\text{Tr} [\rho_{\text{II}}] = 1. \quad (2.57)$$

Writing the state (2.55) in a density matrix formulation is useful to study the *entanglement* between the two degrees of freedom (DOFs) of frequency and path. In fact, one can build the *reduced density matrix* in one DOF by tracing ρ_{II} over the other DOF as

$$\rho_{\text{path}} = \text{Tr}_{\text{freq}} [\rho_{\text{II}}] \quad \rho_{\text{freq}} = \text{Tr}_{\text{path}} [\rho_{\text{II}}], \quad (2.58)$$

and, picking one of the two, from the reduced density matrix we can calculate the *purity* of the reduced state as

$$P = \text{Tr} [\rho_{\text{path}}^2]. \quad (2.59)$$

This is the first figure of merit we introduce and it tells us the degree of entanglement between frequency and path. The upper value of P is 1, defined by $\text{Tr} [\rho_{\text{path}}] = 1$, while the lower bound is $1/\dim(\mathcal{H})$, determined by the Hilbert space dimension $\dim(\mathcal{H})$. When P is very close to unity one can

consider with good approximation the state (2.55) as separable, i.e we can write it as the product of a path state and a frequency state

$$|\text{II}\rangle = |\Xi\rangle_{\text{path}} \otimes |\Psi\rangle_{\text{freq}}, \quad (2.60)$$

with

$$|\Psi\rangle_{\text{freq}} = \frac{1}{\sqrt{2}} \int d\omega_1 d\omega_2 \tilde{\psi}(\omega_1, \omega_2) |\omega_1, \omega_2\rangle, \quad (2.61)$$

and

$$|\Xi\rangle_{\text{path}} = \tilde{\xi}_{i,j} |i, j\rangle, \quad (2.62)$$

Moreover, since a purity $P \approx 1$ guarantees that the two reduced states are pure we can compute another figure of merit: the **Schmidt number** (SN) [35]. Considering for example the reduced density matrix in path, the SN is defined as

$$SN = \frac{1}{\text{Tr}_i [\rho_{\text{path}}^2]}, \quad (2.63)$$

where we traced over one of the two indices i running over the waveguides. The SN gives us an estimate of the entanglement between the two generated photons in the DOF considered. Its values range from $SN = 1$ for photons that are not entangled in path, and thus can be factorized in a state $|\text{II}\rangle_{\text{path}} = |i\rangle |j\rangle$, to values $\gg 1$ indicating strong path correlation between the two photons. A similar reasoning also applies for the frequency DOF.

Another figure of merit that we consider for a qualitative comparison is the diagonal of the path reduced density matrix, the elements of which, $|\tilde{\xi}_{i,j}|^2$, represent the probabilities of finding the two photons exiting the array from all the (i, j) combinations of waveguides. These elements can be arranged in a square matrix called **joint path intensity** (JPI) which has a specific shape that can be connected to the path correlations. With a similar reasoning we can also consider in a qualitative way the diagonal of the frequency reduced density matrix, where the elements are now represented by $|\tilde{\psi}(\omega_1, \omega_2)|^2$. One can discretize this quantity on a grid with equally spaced points and then arrange them in a matrix called **joint spectral density** (JSD). In our work the JSD plays a minor role in the study of disorder, which has a minimal influence on the spectral part of the state. Hence the modifications in the JSD are negligible to observe qualitatively and it is worth reporting it only for the unperturbed structure when required.

Finally we introduce the **fidelity** of the generated state compared to the unperturbed one. This quantity is defined in a simple way as

$$F = |\langle \text{II}_0 | \text{II} \rangle|^2, \quad (2.64)$$

with values ranging from 0 to 1 and it gives an estimate of how similar the state $|\text{II}\rangle$ is to a reference state $|\text{II}_0\rangle$, with $F = 1$ when the states are in fact identical. The fidelity defined in (2.64) is the most general we can compute in our calculations, however if we are interested only in the fidelity of the path part of the state F_{path} the definition is identical but with $|\text{II}_0\rangle_{\text{path}}$ and $|\text{II}\rangle_{\text{path}}$.

3 PATH STATES IN A SINGLE TOPOLOGICAL MODE

The generation of nonclassical light is central to the development of photonic quantum technologies. Among the different approaches that can be used to generate nonclassical light, spontaneous four-wave mixing (SFWM) is arguably the most widely implemented in photonic integrated circuits (PIC) that are fabricated using center-symmetric material like silicon, in which the second order nonlinear response is extremely weak.

The use of PICs, whose fabrication is compatible with complementary metal-oxide semiconductor technologies, is strategic for quantum photonics, because it allows one to take advantage of the technology and the know-how at the core of the electronic industries. In the last ten years, there have been several demonstrations of SFWM in PICs, from simple ridge waveguides [36, 37] and ring resonators [38, 39] to more complex structures, such as photonic crystal cavities [40] and coupled resonators [41–43]. In all these systems, one benefits from light confinement at the microscale to achieve a significant enhancement of the light-matter interaction, up to 8–10 orders of magnitude compared to SFWM in bulk. However, the advantages of sources of nonclassical light based on PICs go beyond the large efficiency. In fact, PICs grant a precise control over the properties of the generated quantum states [44] and allow for scalability [45] of optical quantum systems with tens, or even hundreds, of optical elements integrated on the same chip. Finally, the use of PICs is also interesting from a fundamental point of view, for example to study the interaction of multiple sources of nonclassical light [46].

Although the integration of photonic structures in PICs offers many improvements in terms of control of the quantum state properties, this ability inevitably clashes with the problems that arise in the fabrication process, namely the introduction of defects in the geometrical features of the integrated elements. A recent work by Blanco-Redondo [17] suggests that the quantum properties of nonclassical light can be protected if the generation

process involves a topologically protected mode supported by the PIC. Yet, a rigorous experimental study of the role played by disorder in SFWM requires characterizing the generated pairs in hundreds of samples and is today unpractical. Fortunately, an integrated structure like that of [17] can be easily studied also theoretically, opening the way to a thorough statistical analysis of the effects of disorder carried out through simulations [47]. We note, however, that the topological protection considered here is effective only for certain kinds of disorder that do not alter the structure topology, and all these systems can still be subjected to significant losses due to Rayleigh scattering. Still, the study of parametric processes involving topologically protected modes is interesting from a fundamental point of view, because it is not obvious to what extent topological protection of linear properties persists in the case of nonlinear interactions.

3.1 STRUCTURE AND FIELD PROPAGATION

We start by recalling the structure under investigation for the generation of photon pairs by SFWM, noting that it is chosen to make a direct comparison of our theoretical results based on simulations with the experimental results obtained in [17]. The structure is a silicon over insulator (SOI) platform, composed of an array of 203 identical ridge silicon waveguides fabricated over a silica substrate. The waveguides have typical geometrical parameters for a silicon PIC, with a height $h = 220$ nm and a width $w = 450$ nm, and are separated by short (S) and long (L) gaps of width $d_S = 173$ nm and $d_L = 307$ nm, respectively. In Fig. 3.1 (a) we show a sketch representing a portion of the array where the defect responsible for the topological mode is localized (dashed circle), which is created when two consecutive long gaps are introduced in the periodic sequence of the array. The effective index of the fundamental transverse-electric (TE₀) mode, which is the only one supported by the waveguides, is $n_{\text{eff}} = 2.48$ at 1550 nm and we assume a quadratic dispersion with group velocity $v_g = 6.8 \times 10^{13}$ $\mu\text{m}/\text{s}$ and the group velocity dispersion $\text{GVD} = 2.65 \times 10^{-30}$ $\text{s}^2/\mu\text{m}$, which have been obtained by means of finite-difference time-domain (FDTD) simulations. The array has a length $L = 1$ mm, which is compatible with typical sample sizes used to generate photon pairs by SFWM and allows us to neglect the effects of propagation losses, which are typically 1 dB/cm or less.

To describe light propagation in the array structure we adopt the model presented in Ch.1, which gives a simplified mathematical descriptions of the field propagation inside the array. In this model the key point is to assume that the waveguides are sufficiently far from each other that their guided

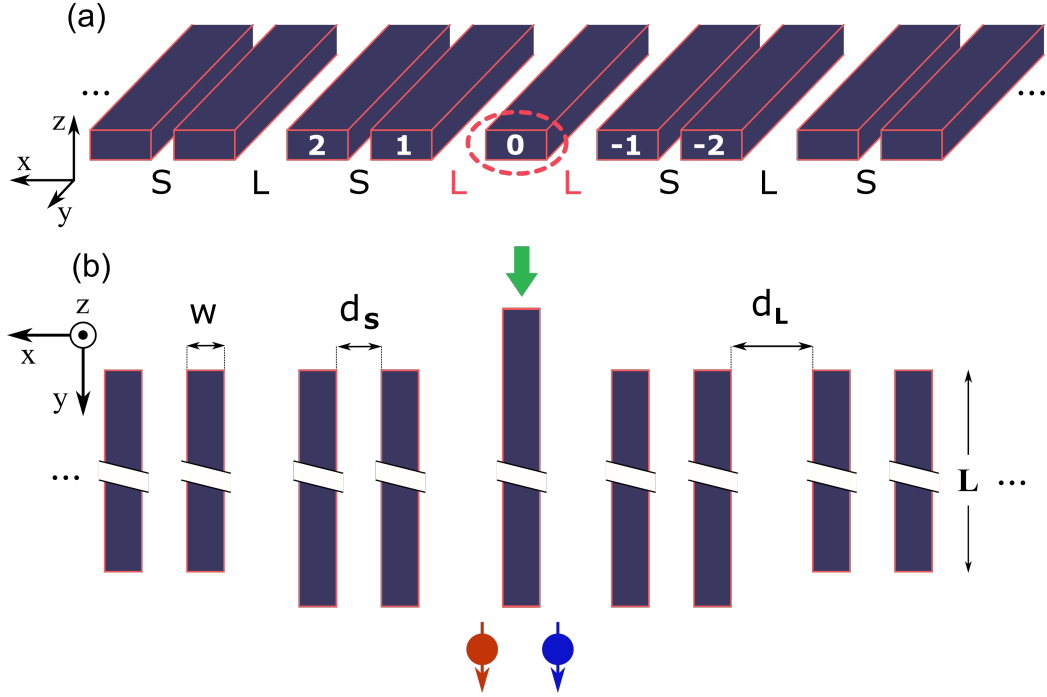


Figure 3.1: (a) Sketch of the array portion with the topological defect (dashed circle) around which the topological mode is localized. The waveguides are labelled starting from the defect. (b) Top view of the same section of the array showing the pumping scheme used in the SFWM process and the relevant geometrical parameters.

modes can be considered orthogonal, and to guarantee that the hypothesis of the model holds also when the structure is modified by disorder we verified it for all the levels of positional disorder considered in this work. Under this assumption the electric displacement field can be written as in (1.1)

$$\mathbf{D}(\mathbf{r}, t) = \frac{1}{\sqrt{2\pi}} e^{i(k_0 y - \omega t)} \left[\sum_{i=1}^N c_i(y) \mathbf{d}_i(x, z) \right], \quad (3.1)$$

where k_0 is the propagation constant of the supported mode under consideration, which is common for each mode since the waveguides are identical, ω is the angular frequency, and $\mathbf{d}_i(x, z)$ is the transverse field distribution centered on the i -th waveguide. Finally, the $c_i(y)$ are coefficients that depend on the position y along the array due to the coupling between adjacent waveguides and allows for energy to be transferred among the waveguides as the field propagate in the array, and at every point y satisfy the normalization

condition (1.2)

$$\sum_{i=1}^N |c_i(y)|^2 = 1. \quad (3.2)$$

If the waveguides are separated enough for modes to be considered orthogonal, then the coupling between the waveguides is small and the fraction of field in each of them, represented by the $c_i(y)$, can be described using a tight-binding approach in which the set of $c_i(y)$ depend from each other through coupling coefficients and satisfy the system of N coupled differential equations (1.10)

$$\frac{d}{dy} \mathbf{c}(y) = -i \mathbf{\Sigma} \mathbf{c}(y), \quad (3.3)$$

where $\mathbf{c}(y) = [c_1(y), \dots, c_N(y)]^T$, and $\mathbf{\Sigma}$ is the tridiagonal matrix of (1.12) containing the coupling constants σ_S and σ_L associated to the d_S and d_L gaps and, considering the small frequency range assumed in this work for the generation of photons, we can consider them as being independent of frequency.

We now proceed to define the asymptotic-in mode fields that will be used for the description of the nonlinear process. Since the construction of the biphoton wave function (BWF) in the SFWM involves four fields $\mathbf{D}(\mathbf{r})$ and requires also an integral over frequency, we decided to use a description of the asymptotic fields in terms of waveguide channels with a single mode to take advantage of the locality of the nonlinear interaction. The downside is that the $c_i(y)$ must be computed at every y for every input channel considered. We recall that the solution of the system (3.3) are in the form

$$\mathbf{c}(y) = \mathbf{S} \exp[-i \mathbf{\Lambda} y] \mathbf{S}^{-1} \mathbf{c}(0), \quad (3.4)$$

where $\mathbf{\Lambda}$ and \mathbf{S} are the diagonal matrix containing the eigenvalues of $\mathbf{\Sigma}$ and the matrix of the eigenvectors, respectively, and for a single $c_i(y)$ this becomes

$$c_i(y) = S_{i,l} e^{-i \lambda_l y} S_{l,k}^{-1} c_k(0), \quad (3.5)$$

where we made use of the diagonal form of $\mathbf{\Lambda}$, with λ_l its eigenvalues, and the repeated indexes are to be summed over. We consider an input field at the beginning of the array $y = 0$ entering in the waveguide I . This is found by setting $c_k(0) = \delta_{k,I}$ in (3.5) which now becomes

$$c_i(y) = S_{i,l} e^{-i \lambda_l y} S_{l,I}^{-1}, \quad (3.6)$$

where and finally we find that the asymptotic-in mode field entering the array structure from the left at the position $y = 0$ can be written as

$$\mathbf{D}_I^{\text{asy-in}}(\mathbf{r}) = \frac{1}{\sqrt{2\pi}} e^{ik_0 y} \sum_i S_{i,l} e^{-i \lambda_l y} S_{l,I}^{-1} \mathbf{d}_i(x, z). \quad (3.7)$$

We now consider the opposite case of an input entering the structure from the right at the end of the array in the position $y = L$ in the waveguide J . This can be found by setting $c_k(0) = e^{-i\phi}\delta_{k,J}$ in (3.5), where now the correct phase ϕ must be determined to be consistent with the choice of our reference frame. To this end we note that the relation (3.5) can be put in a more general form to connect the $c_i(y)$ between any two points y_0 and y_1 as

$$c_i(y) = S_{i,l}e^{-i\lambda_l(y_1-y_0)}S_{l,k}^{-1}c_k(0), \quad (3.8)$$

and thus, setting $y_0 = L$ and $y_1 = y$ we can momentarily write the asymptotic-in mode as

$$\mathbf{D}_J^{\text{asy-in}}(\mathbf{r}) = \frac{1}{\sqrt{2\pi}}e^{-i(k_0y+\phi)}\sum_i S_{i,l}e^{-i\lambda_l(y-L)}S_{l,J}^{-1}\mathbf{d}_i(x,z). \quad (3.9)$$

To find the correct value for the phase ϕ one considers first the case of a single waveguide and observes that

$$\mathbf{D}_{\text{left}}^{\text{asy-in}}(\mathbf{r}) = e^{ik_0L}\mathbf{D}_{\text{right}}^{\text{asy-out}} = e^{ik_0L}\left[\mathbf{D}_{\text{right}}^{\text{asy-in}}\right]^*, \quad (3.10)$$

from which we get

$$e^{ik_0y} = e^{ik_0L}e^{i(k_0y+\phi)}, \quad (3.11)$$

and the value of the phase $\phi = -k_0L$ is determined, so that finally we have the asymptotic-in field mode entering from the right in a waveguide J

$$\mathbf{D}_J^{\text{asy-in}}(\mathbf{r}) = \frac{1}{\sqrt{2\pi}}e^{-ik_0(y-L)}\sum_i S_{i,l}e^{-i\lambda_l(y-L)}S_{l,J}^{-1}\mathbf{d}_i(x,z). \quad (3.12)$$

3.2 TWO-PHOTON STATE GENERATION

To build the state of the generated photons we consider the pumping scheme shown in Fig. 3.1 (b) reporting the experimental situation studied in [17], in which the pump field enters the structure from the central waveguide to provide a very efficient coupling predominantly with the topological mode [see Fig. 1.5 (b)], and the generated photons are collected from the five central waveguides labelled from -2 to 2 in Fig. 3.1 (a). In our simulations we consider a pump pulse centered at $\lambda = 1550$ nm with a 7 ps wide top-hat shape in time, corresponding to a spectral width of $\delta\lambda = 0.4$ nm. The peak power is 1 mW and the collection bandwidth for the generated photons is $\Delta\lambda = 2$ nm around the pump, which is small enough for the coupling coefficients $\sigma_{S(L)}$ to be considered independent of frequency since their variation is less than 1%.

Following our construction of the asymptotic-in fields the quantized $\mathbf{D}(\mathbf{r})$ fields going into the nonlinear Hamiltonian for the SFWM process are

$$\begin{aligned}\mathbf{D}(\mathbf{r}) &= \int_0^\infty dk \sqrt{\frac{\hbar\omega_{I,k}}{2}} c_{I,k} \mathbf{D}_{I,k}^{\text{asy-in}}(\mathbf{r}) + \text{H.c.}, \quad (\text{left}) \\ \mathbf{D}(\mathbf{r}) &= \sum_J \int_0^\infty dk \sqrt{\frac{\hbar\omega_{J,k}}{2}} c_{J,k} \mathbf{D}_{J,k}^{\text{asy-in}}(\mathbf{r}) + \text{H.c.}, \quad (\text{right})\end{aligned}\tag{3.13}$$

where the channel I is fixed to the waveguide labelled 0 and the channels J cover the set of waveguides labelled from -2 to 2 . Using the backward Heisenberg picture approach in the limit of undepleted pump and small probability of generating a photon pair per pulse, the two-photon state can be written as

$$|\text{II}\rangle = \frac{1}{\sqrt{2}} \sum_{p,q} \int_0^\infty d\omega_1 d\omega_2 \phi_{p,q}(\omega_1, \omega_2) c_{p,\omega_1}^\dagger c_{q,\omega_2}^\dagger |\text{vac}\rangle, \tag{3.14}$$

where $c_{q,\omega}^\dagger$ is the creation operator for a photon in the waveguide q at the frequency ω , $|\text{vac}\rangle$ is the vacuum state, and $\phi_{p,q}(\omega_1, \omega_2)$ is the BWF, which contains all the information about the generated state and has the usual form

$$\begin{aligned}\phi_{p,q}(\omega_1, \omega_2) &= \frac{2\sqrt{2}i\pi\alpha^2}{\hbar\beta} \sqrt{v_g^{-1}(\omega_1) v_g^{-1}(\omega_2)} \\ &\times \int_0^\infty d\omega \left\{ \sqrt{v_g^{-1}(\omega) v_g^{-1}(\omega_2 + \omega_1 - \omega)} \right. \\ &\times \left. \phi_P(\omega) \phi_P(\omega_2 + \omega_1 - \omega) S_{p,q}(\omega_1, \omega_1, \omega) \right\},\end{aligned}\tag{3.15}$$

where, as specified in Ch. 2 and in the Appendix, β is the constant that normalized the BWF and in the limit in which the state (3.14) is valid $|\beta|^2$ gives the average pair generation probability per pump pulse, $|\alpha|^2$ is the average number of photons in the pump, $\phi_P(\omega)$ is the pump spectral amplitude, and $v_g(\omega_i)$ are the group velocities at ω_i . Of particular importance in this case is the nonlinear term $S_{p,q}$, which is defined as

$$\begin{aligned}S_{p,q}(\omega_1, \omega_2, \omega) &= \frac{3}{2} \sqrt{\frac{(\hbar\omega_1)(\hbar\omega_2)(\hbar\omega)\hbar(\omega_2 + \omega_1 - \omega)\bar{\chi}_3}{(4\pi)^4 \epsilon_0^2 \bar{n}^4}} \\ &\times J_{p,q}(\omega_1, \omega_2, \omega)\end{aligned}\tag{3.16}$$

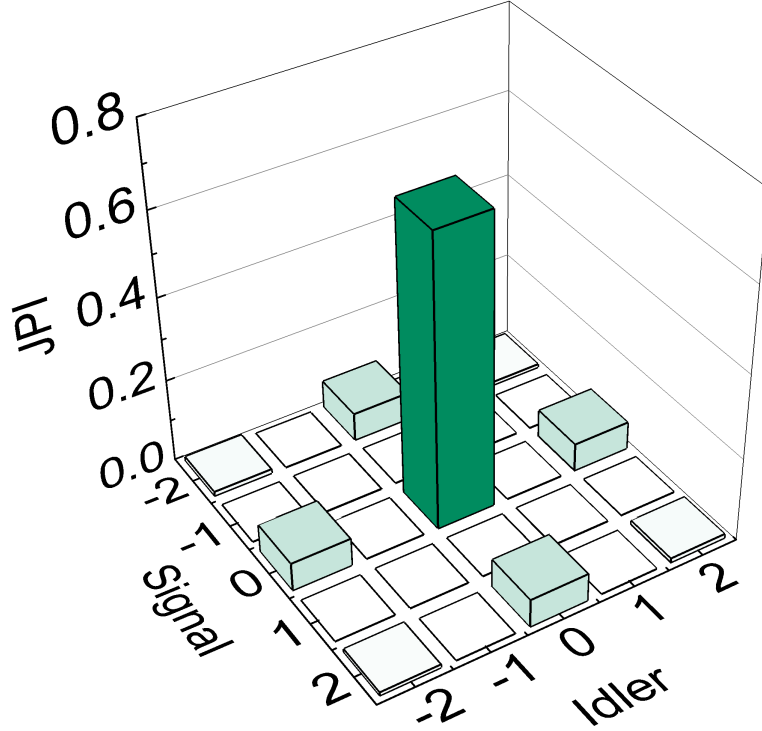


Figure 3.2: Joint path intensity (JPI) matrix of the signal and idler generated photons for the unperturbed structure. The shape is consistent with the symmetry of the topological mode field distribution.

and contains the superposition integral $J_{p,q}$ of the asymptotic-in fields

$$\begin{aligned}
 J_{p,q}(\omega_1, \omega_2, \omega) &= \sum_{r=1}^N \frac{e^{-i(k_0(\omega_1)+k_0(\omega_2))L}}{\mathcal{A}(\omega_1, \omega_2, \omega)} \int_0^L dy \left\{ (M_{rl} e^{-i\lambda_l y} M_{ll}^{-1}) \right. \\
 &\quad \times (M_{rl} e^{-i\lambda_l y} M_{ll}^{-1}) (M_{rl} e^{-i\lambda_l(y-L)} M_{lp}^{-1})^* \\
 &\quad \left. \times (M_{rl} e^{-i\lambda_l(y-L)} M_{lq}^{-1})^* e^{i\Delta k_0(\omega_1, \omega_2, \omega)y} \right\}
 \end{aligned} \tag{3.17}$$

where $\mathcal{A}^{-1}(\omega_1, \omega_2, \omega)$ is the effective nonlinear interaction area defined in (2.17), $\Delta k_0(\omega_1, \omega_2, \omega)$ is the SFWM process phase matching function

$$\Delta k_0(\omega_1, \omega_2, \omega) = k_0(\omega) + k_0(\omega_1 + \omega_2 - \omega) - k_0(\omega_1) - k_0(\omega_2), \tag{3.18}$$

and the sum on r runs over all the waveguides once since the waveguide transverse modes contained in $\mathcal{A}(\omega_1, \omega_2, \omega)$ are assumed to be orthogonal and the nonlinear interaction is *local*.

The *spectral* and *path* degrees of freedom (DOF) on which the BWF depends are intertwined together in the superposition integral, but considering the small collection bandwidth $\Delta\lambda$ we can assume that the process is phase-matched across all the range of corresponding frequencies and thus consider (3.18) and the phase involving $k_0(\omega_i)$ to be practically constant, as well as the effective area \mathcal{A} . Under this hypothesis we can factorize the BWF (3.15) as

$$\phi_{p,q}(\omega_1, \omega_2) = b_{p,q} f(\omega_1, \omega_2), \quad (3.19)$$

where $|b_{p,q}|^2$ is the probability of detecting one photon in the p -th waveguide with the other photon exiting the q -th waveguide, while $f(\omega_1, \omega_2)$ is the so-called joint spectral amplitude. Going a bit further, we distinguish photons in frequency by defining a new two-photon state in *path* as

$$|\text{II}\rangle_{\text{path}} = \sum_{p,q} \alpha_{p,q} |S_p, I_q\rangle \quad (3.20)$$

where $|\alpha_{p,q}|^2$ is the probability of generating a photon pair with the *signal photon* (S) exiting the p -th waveguide and the *idler photon* (I) exiting the q -th waveguide, where the photon is labeled signal (idler) if its energy is smaller (greater) than that of the pump photons. Finally,

$$\begin{aligned} |S_p, I_q\rangle = & \frac{1}{\beta\sqrt{2}} \int_{\omega_P}^{\infty} d\omega_1 \int_{-\infty}^{\omega_P} d\omega_2 [f(\omega_1, \omega_2) + f(\omega_2, \omega_1)] \\ & \times c_{p,\omega_2}^\dagger c_{q,\omega_1}^\dagger |\text{vac}\rangle, \end{aligned} \quad (3.21)$$

is the corresponding state, with $|\beta|^2$ being the probability of having an idler and a signal photon exiting the structure.

We start investigating the properties of the generated path state (3.20) by constructing the joint path intensity (JPI), which gives the joint probabilities that idler and signal photons exit two of the five waveguides considered here. Since in (3.20) we are dealing with a pure state, these probabilities are simply $|\alpha_{p,q}|^2$, which can be arranged in a 5×5 matrix. In Fig. 3.2 we show the JPI in the case of the unperturbed structure, where we can see that with the pumping scheme considered, in which the system is pumped through the central waveguide, photons exit the structure from the even waveguides 0 and ± 2 , with most of them exiting from the central waveguide. The heights of the different peaks and the symmetry of the elements different from zero closely resemble those associated with the intensity distribution of the topologically protected mode we showed in Ch. 1 [Fig. 1.5 (b)]. From the state (3.20) we can calculate also another important quantity, the path Schmidt number,

which is useful to measure in a quantitative way the level of entanglement (in path) between the two generated photons, and is defined as

$$\text{SN}_{\text{path}} = \left(\text{Tr} [\rho_{\text{path}}^2] \right)^{-1}, \quad (3.22)$$

and our calculations give a value $\text{SN}_{\text{path}} = 1.003$, which is very close to 1 meaning that the generated photons are practically not entangled in the path DOF, and that the state can be written in term of a single Schmidt mode. This property is also reflected in the symmetry of the JPI elements, which are, in fact, symmetrical along the two axis and our analysis suggests that both photons are generated only in the topologically protected mode. Finally we report that the generation probability per pump pulse is about $|\beta|^2 \approx 8 \times 10^{-9}$ with the pump parameters and sample length indicated above.

3.3 TOPOLOGICAL PROTECTION OF THE QUANTUM STATE

In this section we analyze the effects of disorder on the properties of the generated photons quantum state. We recall from Ch. 1, when we studied the effect of disorder on the linear properties of the topological modes, that the type of disorder considered is *positional* in nature, i.e. it modifies the relative position of the waveguides along the horizontal direction x [Fig. 3.1 (a)] and thus the gaps between each pair of waveguides. As consequence the relative coupling constants σ_i in the matrix Σ of Eq. (3.3) change. To introduce positional disorder in our simulation, we modify the relative position of the waveguides in the original structure by an amount that follows a Gaussian distribution with a mean $\mu = 0$ and a standard deviation σ ranging from 0 to 43 nm, and for each level of disorder considered we create an ensemble of 300 realizations so that all the quantities calculated are statistically meaningful. The values of $\sigma = 14$ nm and $\sigma = 43$ nm are especially significant because they are the same considered in [17] and allow us to directly compare the results.

We start our analysis of disorder by considering the JPI calculated from the state (3.20). In Fig. 3.3 (a) we show the average JPI obtained for an ensemble of 300 realizations with $\sigma = 14$ nm of disorder in the waveguide displacement, where the error bars indicate the standard deviation for each mean value of the element $|\alpha_{p,q}|^2$. The overall shape of the JPI is very similar to the case with no disorder, and even the small standard deviation confirms that for such a level of disorder path correlations are robust and hence topologically protected. In this sense our findings are in good agreement with the

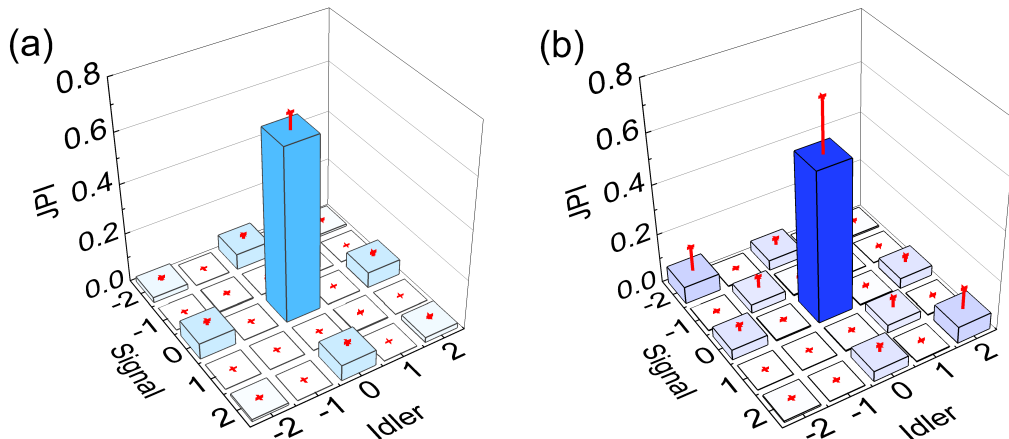


Figure 3.3: Average joint path intensity (JPI) matrix of the signal and idler generated photons in structures affected by disorder with (a) $\sigma = 14$ nm and with (b) $\sigma = 43$ nm. Error bars correspond to one standard deviation.

experimental results shown in [17]. Now we observe the average JPI, shown in Fig. 3.3 (b), obtained with $\sigma = 43$ nm. In this case, with the increase of disorder one can notice a considerable growth of the elements corresponding to the waveguide combinations $(-2, -2)$ and $(2, 2)$, with the error bars indicating that the JPI is on average appreciably affected by the random variation in the waveguide displacement. Yet the most surprising result is the appearance of non-zero elements corresponding to the waveguide combinations $(-1, -1)$ and $(1, 1)$, which is somewhat unexpected because our analysis of the linear properties of the topological mode clearly showed that the symmetry of its field distribution are protected against disorder also for $\sigma = 43$ nm. Our result on the JPI for this level of disorder is in some way reminiscent of the experimental data reported in [17], however in their case measurements were performed on a single sample and the occurrence of the unexpected terms were attributed not to a degradation of the topological protection but to inhomogeneity in the waveguide widths, which are known to affect the linear properties of the topological mode. In contrast, in our theoretical study we are absolutely sure to consider identical waveguides, with disorder affecting only their position. Thus, our results show that, for such high level of disorder, the *quantum correlations of the generated photons are less robust than the linear properties of the topological mode*.

To shed some light on the origin of this discrepancy between the linear properties of the topological mode and the quantum properties of photon pairs generated in it, we study the effects of disorder on the generated state

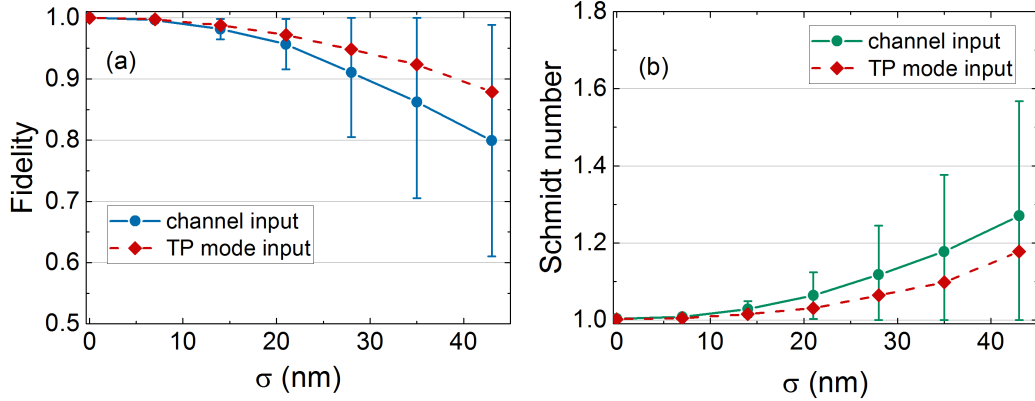


Figure 3.4: Average joint path intensity (JPI) matrix of the signal and idler generated photons in structures affected by disorder with (a) $\sigma = 14$ nm and with (b) $\sigma = 43$ nm. Error bars correspond to one standard deviation. The dashed lines represents average values calculated by suppressing intra-mode SFWM in non-topological modes.

(3.20) in terms of both the fidelity with respect to the unperturbed state $|\Pi_0\rangle_{\text{path}}$

$$F_{\text{path}} = \left| \langle \Pi_0 | \Pi \rangle_{\text{path}} \right|^2, \quad (3.23)$$

and the path Schmidt number SN_{path} . In Fig. 3.4 we show the trend of their average value (solid curves) calculated on the ensemble of 300 realizations for each level of disorder. Clearly when disorder is absent $\sigma = 0$ the fidelity is 1 and the value of the Schmidt number is that reported previously (≈ 1). As disorder increases to $\sigma = 14$ nm the fidelity in Fig. 3.4 (a) remain well above 0.95 and SN_{path} in Fig. 3.4 (b) continue to be very close to 1, meaning that we are in a situation in which the effects of disorder do not alter the properties of photons generated in the topological state. In this range of disorder level, the change in the relative position of the waveguides certainly modifies the structure but the effects on the array modes is minimal and the results are almost the same as the case with no disorder, with photon pairs generated almost always in the topological mode. This is confirmed by the JPI in Fig. 3.3 (a) which doesn't differ appreciably from that of the unperturbed structure and has a low variance in the averaged matrix elements. When disorder increases to $\sigma = 43$ nm we see a clear drop in fidelity to 0.79 with an increased variance, while at the same time the Schmidt number grows to $\text{SN}_{\text{path}} = 1.3$. In this case, although the level of disorder is far higher than before, the structure doesn't lose its topological nature as demonstrated in Ch. 1 for the linear properties, but the process of photon pair generation is

strongly affected. First of all we can say that the average JPI of Fig. 3.3 (b) does not differ that much from that of the unperturbed structure only because we have averaged each matrix element over many realizations. However, each realization of the ensemble can lead to a quite different generated state, as shown by the large standard deviation in the fidelity. Moreover, a non negligible number of these path states is responsible for the appearance of the large $(\pm 2, \pm 2)$ terms on the diagonal and, most importantly, the $(\pm 1, \pm 1)$ that represent a clear break with the symmetry of the topological mode. This process is explained well by the increase in SN_{path} which means that other modes of the array, beside the topological mode, become gradually more relevant in the nonlinear interaction.

INTRA- AND INTER-MODE SFWM

We divide the contribution of non-topological modes to the generation of pairs into two mechanisms, *intra*-mode and *inter*-mode SFWM, depending on how they enter the nonlinear process. To help understanding this part, here we briefly adopt a description of the field $\mathbf{D}(\mathbf{r})$ on the basis of the structure supermodes $\mathbf{d}_a(\mathbf{r})$, and thus we can write it as

$$\mathbf{D}(\mathbf{r}) = \sum_a \alpha_a \mathbf{d}_a(x, z) e^{ik_a y}, \quad (3.24)$$

where $\mathbf{d}_a(x, z)$ is the mode transverse field distribution, k_a its propagation constant, and α_a are real coefficients.

The first mechanism of intra-mode SFWM includes all those contributions in the nonlinear Hamiltonian that have the form

$$H_{\text{NL}} \propto \alpha_a^2 \int d\mathbf{r} \chi_{(3)}(\mathbf{r}) \mathbf{d}_a(x, z) \mathbf{d}_a(x, z) \mathbf{d}_a^*(x, z) \mathbf{d}_a^*(x, z) e^{i\Delta k y}, \quad (3.25)$$

excluding the case in which the index a indicates the topological mode. Since they only involve one supermode at a time the spatial overlap on the xz plane is always maximum, while the Δk is always equal to zero for the SFWM process. The only relevant figure for this mechanism is the value assumed by the α_a^2 term, which depends on the amount of light coupled to each non-topological mode at the beginning of the array. In fact, when we pump light in the waveguide numbered with 0, we excite in principle all the modes with different weights, as indicated by (3.24) where the coefficients

$$\boldsymbol{\alpha} = [\alpha_T, \alpha_1, \dots, \alpha_{N-1}], \quad (3.26)$$

which include α_T corresponding to the topological mode, are determined by

$$\alpha_a = \int dx dz \mathbf{d}_{\text{WG0}}(x, z) \mathbf{d}_a^*(x, z), \quad (3.27)$$

with $\mathbf{d}_{\text{WG0}}(x, z)$ the single waveguide mode profile. In the case of the perfect structure α_T is almost 1 and all the others α_a are close to 0. When disorder is introduced the coefficient α_T is still dominant thanks to the protection of the field profile ($\mathbf{d}_{T,\sigma}(x, z) \approx \mathbf{d}_T(x, z)$); but this is not true for the other non-topological modes which can change quite significantly, leading in some cases to a more efficient coupling in (3.27) and larger values of α_a^2 .

The second mechanism of inter-mode SFWM includes the other remaining contributions in which photon pairs are generated in modes that are distinct from those of the pump photons. The nonlinear Hamiltonian terms now have the form

$$H_{\text{NL}} \propto \alpha_a \alpha_b \int d\mathbf{r} \chi_{(3)}(\mathbf{r}) \mathbf{d}_a(x, z) \mathbf{d}_b(x, z) \mathbf{d}_c^*(x, z) \mathbf{d}_d^*(x, z) e^{i\Delta k y}, \quad (3.28)$$

and the variety of combinations is large. Despite this, they all share a relevant aspect, that is the spatial overlap of the modes and the phase matching condition now dominate the efficiency of the process instead of the product $\alpha_a \alpha_b$. To explain this mechanism we consider as an example the case where the two pump photons are both in the topological mode, which is the one more likely to give a substantial contribution. For the perfect structure the generation of photons in a pair of other non-topological modes depends on how well $\mathbf{d}_{c,d}^*(x, z)$ overlaps with the field profile $\mathbf{d}_T(x, z)$ of the topological mode. In addition, since Δk should be as close to 0 as possible, the most efficient combinations involve the generation of photon pairs in modes having their propagation constants symmetrically distributed around that of the topological mode, i.e. $k_{c,d} = k_0 \pm \delta$ [see Fig.1.5(a)]. These two conditions are very hard to satisfy at the same time, as demonstrated by $\text{SN}_{\text{path}} = 1$. When disorder is introduced the mode profiles $\mathbf{d}_{c,d}^*(x, z)$ can change significantly and improve the spatial overlap in (3.28). While the coupling constant also change due to disorder [see Fig. 1.7(a)], this effect has minimal impact on Δk for symmetrically distributed modes and the generation of photons in other non-topological modes becomes, in general, more efficient.

To evaluate the relative contribution of these two mechanisms responsible for the breakdown of the topological protection, we have performed another statistical analysis using a pump coupled exclusively to the topological mode, thus suppressing intra-mode SFWM for all the non topological modes. From the mathematical point of view of the asymptotic-in fields, this is done by considering the whole array as a single channel supporting N modes. For the field describing pump light coupled from the left, we set the initial condition $\mathbf{c}(0)$ equal to the eigenvector of the topological mode, and this stays constant in the propagation along y . All the calculations for the average fidelity and Schmidt number under this condition are reported in Fig. 3.4 (dashed line)

and allow us to verify that in our structure inter-mode SFWM is the main process contributing to the change in fidelity and Schmidt number as disorder increases, accounting for an effect on the properties of the generated photons state that is twice more likely than that of intra-mode SFWM, when disorder is large. In the end even if we have the best coupling option for the pump, which can be achieved with a clever scheme if desired, the protection against disorder observed for the linear properties of the topological mode is not completely transferred to the quantum properties of the two-photon state generated through nonlinear interaction.

3.4 CONCLUSIONS

Putting together the results on the linear properties reported in Ch. 1 and the nonlinear properties just presented here, our work represents a systematic study of the generation of photon pairs by SFWM in a topologically protected mode supported by a one-dimensional silicon waveguide array. We investigated the effect of positional disorder up to levels of $\sigma = 43$ nm on the path quantum correlations of the generated photons by means of a statistical analysis and the calculation of JPI, fidelity of the two-photon state, and path Schmidt number.

We showed that, for $\sigma = 14$ nm topological protection of the generated state is in general *robust* for this type of structure, in agreement with a previous experimental study on the same system [17]. However, such a protection can decrease substantially for larger values of disorder and, since this happens with continuity, one cannot define precisely a sharp threshold, and the acceptable level of disorder depends on the requirements set by applications. A quantitative analysis in terms of fidelity and SN_{path} revealed that in our system quantum correlations can arise from *inter*-mode and *intra*-mode SFWM, which involve modes supported by the waveguide array that are not topologically protected. To the best of our knowledge, these contributions have not been considered in previous studies [17], where the authors attributed the appearance of unexpected spurious elements in the JPI to undesired modifications of the waveguides width in the fabrication step, which are known to break the structure chirality. Also, the difficulties in performing a statistical experimental analysis greatly limited the number of samples and, consequently, the ability to spot these effects which emerge only at the statistical level. Here instead, we showed that these nonlinear mechanisms can play a central role in the SFWM process when disorder increases, reducing the topological protection of the biphoton state.

Our results are important, because they demonstrate that topological pro-

tection of the linear properties of an optical system does not extend equally to the case of nonlinear interactions. Thus, in general, care must be taken in seeking for topological protection of biphoton states, because such a protection might be less effective than what one would assume solely from an analysis of the linear properties of the system. Similar results are expected for other photonic systems and second-order nonlinear interactions, but further investigations are needed to determine the role of topological protection in these cases. The next chapter investigates precisely the role of the nonlinear interaction process in the topological protection, focusing on SPDC for the generation of photon pairs.

4 HYPER-ENTANGLED STATES IN COUPLED TOPOLOGICAL MODES

Recently, topological photonics has been indicated as a possible approach to mitigate disorder in integrated photonics structures [7, 8, 48–50], the idea being based on the experimental evidence that topological properties are inherently more robust with respect to disorder and/or fabrication imperfection that do not alter the structure topology [16]. Topological protection has been studied also in the field of integrated quantum photonics [17], in which one looks for solutions to protect quantum correlations of photonic states, usually generated by parametric fluorescence.

Initial studies in this direction have focused on the generation of nearly uncorrelated photon pairs via spontaneous four-wave mixing (SFWM) in waveguide arrays supporting a single guided mode arising from a topological discontinuity [17], or coupled ring resonators [51], in which topology provides spectral robustness for the generated photon pair. Similar studies on correlated pairs, instead, relied on waveguide arrays with two *isolated* topological defects [17, 52]. Experimental results suggested that the robustness of topological modes is, in part, transferred to the generated state, whose properties remain unaffected for small perturbations of the photonic structure. On the other hand, as we have demonstrated in the previous chapter, a theoretical analysis relying on a statistical approach has revealed that, in general, topological protection of the linear properties of an optical system does not equally extend to the case of nonlinear interactions [47]. In particular, we showed that this is due to the nonlinear coupling of topologically protected and unprotected modes.

The above-mentioned studies deal with the generation of nearly uncorrelated photons generated via SFWM in which photon correlations involve only one degree of freedom (DOF), either path or energy. However, recent developments in integrated photonics based on thin-films lithium niobate (LN) [53] encourage to extend the study of topological protection to second-order nonlinear processes such as spontaneous parametric down conversion

(SPDC). This is not a simple generalization of the SFWM case, as in SPDC energy conservation requires to work with fields at very different frequencies, with the pump field having an energy that is the sum of the energy of the generated photons. This means that the structure properties at the pump frequency can be quite different from those at the frequency of the generated photons, as shown in Fig. 1.6 of Ch.1. Thus, topological properties are expected to play a very different role with respect to the SFWM case.

Here we study the generation of photon pairs by SPDC in an integrated waveguide array supporting *two* topological guided modes [54] and focus our attention on the simultaneous occurring of *path and energy entanglement*. We study the purity of the generated state once projected on either Hilbert subspace and analyze the robustness of the photon correlations when disorder is introduced in the structure.

4.1 STRUCTURE AND FIELD PROPAGATION

We start also here by recalling the properties of the structure considered for the generation of photon pairs by SPDC. The structure is based on a lithium niobate over insulator (LNOI) platform formed by an array of 42 identical trapezoidal rib waveguides that can be fabricated by partial etching of a Z-cut LN film deposited on a silica substrate [26]. The waveguides have a top width $w = 1.2 \mu\text{m}$, a height $h = 460 \text{ nm}$, and a side angle of 75° . The partial etching of the LN film leaves an underlying LN layer of thickness $t = 100 \text{ nm}$ that forms the rib geometry and supports the waveguides. The geometrical parameters are engineered to achieve the condition of phase matching for the type-I SPDC process involving the strong χ_2^{zxx} component of the nonlinear tensor, in which a pump photon at $\lambda_P = 775 \text{ nm}$ from the second transverse-magnetic (TM2) mode is annihilated, and a photon pair is created at the fundamental wavelength $\lambda_F = 1550 \text{ nm}$ in the fundamental transverse-electric (TE0) mode. The effective index of the TE0 and TM2 mode is $n_{eff} = 1.94$ at phase matching, and we assume a quadratic dispersion with group velocity $v_g = 1.25 \times 10^{14} \mu\text{m/s}$ and group velocity dispersion $\text{GVD} = 6.26 \times 10^{-30} \text{ s}^2/\mu\text{m}$ for the TE0 mode, and $v_g = 1.20 \times 10^{14} \mu\text{m/s}$, $\text{GVD} = 2.25 \times 10^{-30} \text{ s}^2/\mu\text{m}$ for the TM2 mode. The waveguides are separated by alternating short (S) and long (L) gaps having widths, measured at the base, equal to $d_S = 300 \text{ nm}$ and $d_L = 450 \text{ nm}$, respectively, and the total length of the array is $L = 2.5 \text{ mm}$. In Fig. 4.1 (a) we show the portion of the array where we introduced two separate topological defects by repeating the long gap in the periodic sequence at a distance of a few waveguides. Because of the short distance between the two defects, the array supports two

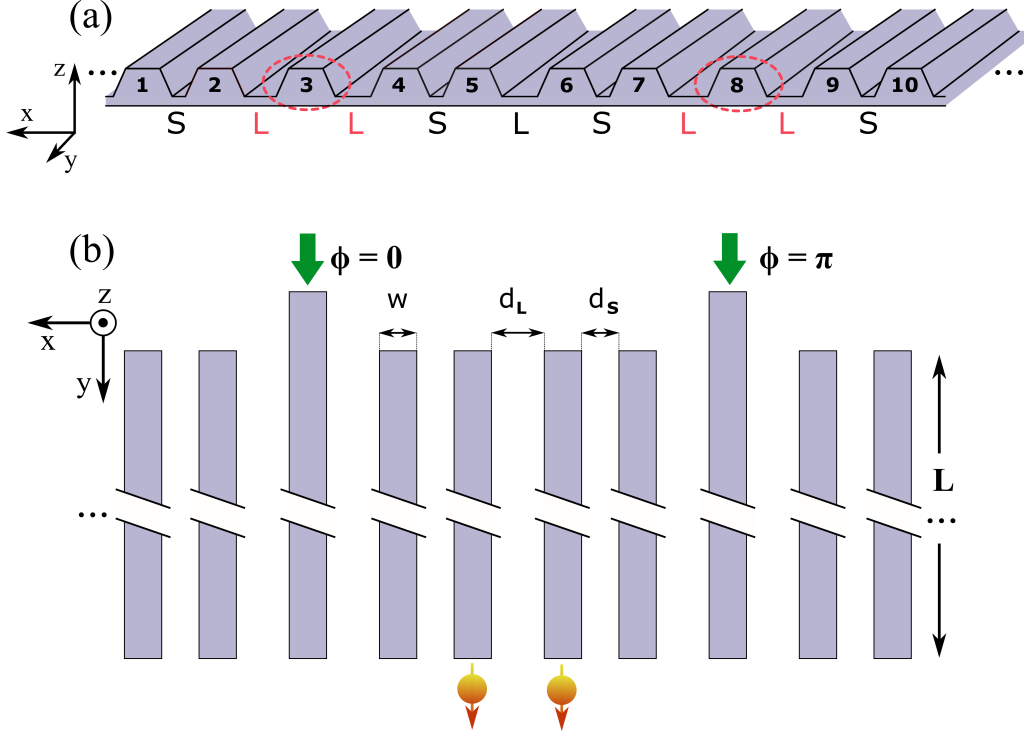


Figure 4.1: (a) Sketch of the array portion with the topological defect (dashed circle) around which the topological mode is localized. The waveguides are labelled starting from the defect. (b) Top view of the same section of the array showing the pumping scheme used in the SFWM process and the relevant geometrical parameters.

topological modes with symmetric and anti-symmetric field distributions, respectively. This is valid at both λ_P and λ_F , respectively for the TM2 and TE0 modes, as shown in 1.6 (b-e). These two modes can be viewed as arising from the strong coupling of the two topological modes that would be supported by each defect when taken individually.

To describe light propagation in the array we adopt also here the model presented in Ch.1, in which we assume that the waveguides are sufficiently far from each other that their guided modes can be considered orthogonal. This hypothesis has been verified for the TE0 mode at all levels of positional disorder considered in this work, which automatically guarantees that the hypothesis holds also for the more confined TM2 mode. Under this assumption the electric displacement field at the frequency ω corresponding to either

λ_P or λ_F can be written as in (3.1)

$$\mathbf{D}(\mathbf{r}, t) = \frac{1}{\sqrt{2\pi}} e^{i(k_0(\omega)y - \omega t)} \left[\sum_{i=1}^N c_i(y) \mathbf{d}_{\omega,i}(x, z) \right], \quad (4.1)$$

where $k_0(\omega)$ is the propagation constant of the supported TE0 or TM2 mode under consideration, common for each waveguide since they are identical, ω is the angular frequency, and $\mathbf{d}_{\omega,i}(x, z)$ is the transverse field distribution of the mode centered on the i -th waveguide. At every y the sum of $|c_i(y)|^2$ over all the waveguides i is normalized to 1. Under the hypothesis of orthogonal modes the coupling between the waveguides is small enough to consider the evolution in space of the $c_i(y)$ in a tight-binding approach in which the set of $c_i(y)$ depend from each other through coupling coefficients and satisfy the system of N coupled differential equations (3.3)

$$\frac{d}{dy} \mathbf{c}(y) = -i\mathbf{\Sigma}(\omega) \mathbf{c}(y), \quad (4.2)$$

where $\mathbf{c}(y) = [c_1(y), \dots, c_N(y)]^T$, and $\mathbf{\Sigma}(\omega)$ is the tridiagonal matrix of Eq. (1.12) whose elements are the coupling constants $\sigma_S(\omega)$ and $\sigma_L(\omega)$ associated to the d_S and d_L gaps, respectively, which are now considered dependent on the frequency following Eq. (1.8). The vector solution $\mathbf{c}(y)$ of the system (4.2) is then also dependent on the frequency, and this reasoning applies equally to both frequency ranges around ω_P and ω_F

Now we define the asymptotic-in mode fields that will be used for the description of the nonlinear process. In the case of SPCD, compared to the previous SFWM process, the construction of the biphoton wave function (BWF) is much simpler as it involves three fields $\mathbf{D}(\mathbf{r})$ and no additional integral over frequencies. Thus we decided to use a description of the asymptotic field modes in terms of the supermodes supported by the array as a whole. In this representation the structure is effectively connected by only two channels, one on the left and one on the right, each supporting N modes. Following this approach we are not interested in the solution of the system (4.2) but we only need to find the supermodes by diagonalizing $\mathbf{\Sigma}(\omega)$. As reported in Ch. 1 the matrix $\mathbf{\Sigma}(\omega)$ can be decomposed with a similarity transformation as $\mathbf{\Sigma}(\omega) = \mathbf{S}(\omega) \mathbf{\Lambda}(\omega) \mathbf{S}^{-1}(\omega)$ where $\mathbf{\Lambda}(\omega)$ is the diagonal matrix containing the frequency dependent eigenvalues $\lambda_i(\omega)$ and the column vectors $\mathbf{s}_i(\omega)$ of $\mathbf{S}(\omega)$ are the corresponding frequency dependent eigenvectors.

Considering an input field in the supermode I entering from the left channel at the beginning of the array $y = 0$, the corresponding asymptotic-in field mode is

$$\mathbf{D}_I^{\text{asy-in}}(\mathbf{r}) = \frac{1}{\sqrt{2\pi}} e^{ik_I(\omega)y} \bar{\mathbf{d}}_{\omega,I}(x, z), \quad (4.3)$$

where $k_I(\omega)$ is the propagation constant of the array supermode I at the frequency (ω) , defined as

$$k_I(\omega) = k_0(\omega) + \lambda_I(\omega), \quad (4.4)$$

and $\bar{\mathbf{d}}_{\omega,I}(x, z)$ is the transverse field profile of the array supermode. Under the hypothesis of orthogonal single waveguide modes we can rewrite $\bar{\mathbf{d}}_{\omega,I}(x, z)$ as

$$\bar{\mathbf{d}}_{\omega,I}(x, z) = \sum_i^N s_{i,I}(\omega) \mathbf{d}_{\omega,i}(x, z), \quad (4.5)$$

where $s_{i,I}$ is the i -th component of the eigenvector $\mathbf{s}_I(\omega)$ associated to the supermode I , with the sum running over all the waveguides, and $\mathbf{d}_{\omega,i}(x, z)$ is the usual single waveguide mode transverse field. Finally, we can write the asymptotic-in field (4.3) as

$$\mathbf{D}_I^{\text{asy-in}}(\mathbf{r}) = \frac{1}{\sqrt{2\pi}} e^{ik_I(\omega)y} \sum_i^N s_{i,I}(\omega) \mathbf{d}_{\omega,i}(x, z), \quad (4.6)$$

and with a similar procedure the asymptotic-in field mode corresponding to an input field in the supermode J entering from the right channel at the end of the array $y = L$ is

$$\mathbf{D}_J^{\text{asy-in}}(\mathbf{r}) = \frac{1}{\sqrt{2\pi}} e^{-ik_J(\omega)(y-L)} \sum_i^N s_{i,J}(\omega) \mathbf{d}_{\omega,i}(x, z). \quad (4.7)$$

4.2 TWO-PHOTON STATE GENERATION

Here we carry out the calculations for the state of the generated photons using our description of the asymptotic fields in terms of array supermodes and then we translate the results back on the basis of single waveguides to match the pumping scheme and photon collection of Fig. 4.1 (b). Following our construction of the asymptotic-in field modes, the quantized $\mathbf{D}(\mathbf{r})$ fields entering the nonlinear Hamiltonian for the SPDC process are

$$\begin{aligned} \mathbf{D}(\mathbf{r}) &= \int_0^\infty dk \sqrt{\frac{\hbar\omega_{I,k}}{2}} c_{I,k} \mathbf{D}_{I,k}^{\text{asy-in}}(\mathbf{r}) + \text{H.c.}, \quad (\text{left}) \\ \mathbf{D}(\mathbf{r}) &= \sum_J \int_0^\infty dk \sqrt{\frac{\hbar\omega_{J,k}}{2}} c_{J,k} \mathbf{D}_{J,k}^{\text{asy-in}}(\mathbf{r}) + \text{H.c.}, \quad (\text{right}) \end{aligned} \quad (4.8)$$

where we fixed the input field to one supermode I and we let the field of the generated photons to span over all the supermodes J . Following the backward Heisenberg picture approach in the limit of undepleted pump approximation and small generation probability, the two-photon state $|\text{II}\rangle_t$ generated by a pump photon in the supermode t is

$$|\text{II}\rangle_t = \frac{1}{\sqrt{2}} \sum_{p,q} \int_0^\infty d\omega_1 d\omega_2 \phi_{p,q;t}(\omega_1, \omega_2) c_{p,\omega_1}^\dagger c_{q,\omega_2}^\dagger |\text{vac}\rangle, \quad (4.9)$$

where $c_{q,\omega}^\dagger$ is the creation operator for a photon in the supermode q at the frequency ω , $|\text{vac}\rangle$ is the vacuum state, and $\phi_{p,q;t}(\omega_1, \omega_2)$ is the biphoton wave function (BWF) of two photons created in the supermodes p and q at frequencies ω_1 and ω_2 , respectively, given a pump photon in the supermode t at frequency $\omega_1 + \omega_2$. The BWF can be written as

$$\begin{aligned} \phi_{p,q;t}(\omega_1, \omega_2) &= \frac{2\pi\sqrt{2}i\alpha}{\beta\hbar} \sqrt{v_{g,p}^{-1}(\omega_1)v_{g,q}^{-1}(\omega_2)} \\ &\times \sqrt{v_{g,t}^{-1}(\omega_1 + \omega_2)} \phi_P(\omega_1 + \omega_2) S_{p,q;t}(\omega_1, \omega_1, \omega), \end{aligned} \quad (4.10)$$

where $|\alpha|^2$ is the average number of photons in the pump pulse, β is a constant that normalizes the modulus squared of the BWF, $v_{g,p}(\omega)$ is the group velocity of the supermode p at frequency ω , $\phi_P(\omega_1 + \omega_2)$ is the spectral amplitude function of the pump pulse, and $S_{p,q;t}(\omega_1, \omega_1, \omega)$ is

$$\begin{aligned} S_{p,q;t}(\omega_1, \omega_2) &= \sqrt{\frac{(\hbar\omega_1)(\hbar\omega_2)\hbar(\omega_2 + \omega_1)\bar{\chi}_2}{(4\pi)^3\epsilon_0}} \frac{1}{\bar{n}^3} \\ &\times J_{p,q;t}(\omega_1, \omega_2) \end{aligned} \quad (4.11)$$

where this time the superposition integral $J_{p,q;t}(\omega_1, \omega_2)$ is defined as

$$\begin{aligned} J_{p,q;t}(\omega_1, \omega_2) &= \sum_{r=1}^N \frac{e^{-i(k_p(\omega_1) + k_q(\omega_2))L}}{\sqrt{\mathcal{A}(\omega_1, \omega_2)}} s_{r;t}(\omega_1 + \omega_2) s_{r;p}^*(\omega_1) s_{r;q}^*(\omega_2) \\ &\times \int_0^L dy e^{i(k_t(\omega_1 + \omega_2) - k_p(\omega_1) - k_q(\omega_2))y} \end{aligned} \quad (4.12)$$

where $\mathcal{A}(\omega_1, \omega_2)$ is the effective nonlinear interaction area defined in (2.11) for an isolated waveguide, and the sum on r runs over all the waveguides once since we assumed waveguide modes to be orthogonal and the nonlinear interaction χ_2 is *local*.

Now we consider SPDC in the waveguide array following the pumping scheme shown in Fig. 4.1 (b), where we assume to work in the case of a dual-pump coupling in which two coherent square pulses centered at λ_P , having a duration $\tau = 0.5$ ns and total power of 1 mW, are injected in the array from the two defect waveguides, labelled 3 and 8, to have efficient coupling with the topological modes [see Fig. 1.6(d-e)]. A relative phase shift $\phi = \pi$ is applied to the pulses before entering the array to excite only the odd topological mode. This choice guarantees that, starting with a pump photon in the odd topological mode, the SPDC process results in the generation of a pair in which the two photons are generated in the odd and even topological modes, respectively. The symmetry constrain is enforced by the product of the coefficients $s_{r,i}(\omega)$, which carry the symmetry distribution of the modes, summed over all the waveguides in the overlap integral $J_{p,q;t}(\omega_1, \omega_2)$. Moreover, since the odd and even topological modes have propagation constants symmetrically distributed around k_0 [see Fig. 1.6(a)], this SPDC generation scheme is better phase-matched compared to the other possible case in which the two coherent pump pulses have the same phase and excite the even topological mode, resulting in the generation of photon pairs both in the even or the odd topological mode. Finally, we assume that photon pairs are collected from all the waveguides labelled from 1 to 10 over a bandwidth of 50 GHz ($\Delta\lambda = 0.4$ nm), resulting in a calculated generation rate of about 1.8×10^{-5} pairs/pulse. To write an expression for the two-photon state representing this excitation-collection scheme we start by noting that, with our pumping scheme, the output state is a coherent superposition of states like (4.9) that can be written as

$$|\text{II}\rangle_{\text{all-t}} = \frac{1}{\sqrt{2}} \sum_{p,q} \int_0^\infty d\omega_1 d\omega_2 \Phi_{p,q}(\omega_1, \omega_2) |p, \omega_1\rangle |q, \omega_2\rangle, \quad (4.13)$$

with $\Phi_{p,q}(\omega_1, \omega_2)$ the coherent superposition of the BWFs of Eq. (4.9), defined as

$$\Phi_{p,q}(\omega_1, \omega_2) = \sum_t b_t(\omega_1, \omega_2) \phi_{p,q;t}(\omega_1, \omega_2) \quad (4.14)$$

and the frequency dependent coefficients $b_t(\omega_1, \omega_2) \equiv b_t(\omega_1 + \omega_2)$ are found from

$$b_t(\omega_1 + \omega_2) = S_{t,l}^{-1}(\omega_1 + \omega_2) v_l \quad (4.15)$$

where $\mathbf{S}^{-1}(\omega)$ is the inverse eigenvector matrix calculated at ω and \mathbf{v} is the input vector with elements $v_3 = \sqrt{2}/2$ and $v_8 = -\sqrt{2}/2$, according to the pumping scheme, and all the others equal to zero. The next step is to move from the space of array supermodes to the space of waveguides, and

we recall from Ch. 1 that \mathbf{S} represents exactly the matrix that performs this operation since its columns are the supermodes written on the basis of single waveguides. The state 4.13 is then transformed accordingly and can be finally expressed in terms of the *frequency* and *path* DOFs as

$$|\text{II}\rangle_{\text{all-WG}} = \frac{1}{\sqrt{2}} \sum_{i,j} \int_0^\infty d\omega_1 d\omega_2 \Psi_{i,j}(\omega_1, \omega_2) |i, \omega_1\rangle |j, \omega_2\rangle, \quad (4.16)$$

where i and j now run over all the waveguides of the array and $\Psi_{i,j}(\omega_1, \omega_2)$ is defined in matrix form as

$$\Psi(\omega_1, \omega_2) = \mathbf{S}(\omega_F) \Phi(\omega_1, \omega_2) \mathbf{S}^{-1}(\omega_F), \quad (4.17)$$

where, for all the combinations of ω_1 and ω_2 , we use the eigenvector matrix computed at the central frequency ω_F of the collection bandwidth, corresponding to $\lambda_F = 1550$ nm. Finally, we restrict the *path* Hilbert space to the 10 waveguides labelled in Fig. 4.1 (b) and the state of generated photons becomes

$$|\text{II}\rangle = \frac{1}{\sqrt{2}} \sum_{i,j=1}^{10} \int_0^\infty d\omega_1 d\omega_2 \psi_{i,j}(\omega_1, \omega_2) |i, \omega_1\rangle |j, \omega_2\rangle, \quad (4.18)$$

where $\psi_{i,j}(\omega_1, \omega_2)$ is now correctly normalized as

$$\sum_{i,j=1}^{10} \int_0^\infty d\omega_1 d\omega_2 |\psi_{i,j}(\omega_1, \omega_2)|^2 = 1, \quad (4.19)$$

such that $|\psi_{i,j}(\omega_1, \omega_2)|^2 d\omega_1 d\omega_2$ represents the probability of finding a pair with one photon exiting the array from waveguide i and frequency between ω_1 and $\omega_1 + d\omega_1$, and one photon exiting the array from waveguide j and frequency between ω_2 and $\omega_2 + d\omega_2$.

We now begin to study the properties of the generated state (4.18) in the case of the unperturbed structure. As in the previous case of SFWM here in the SPDC process we start from a pure coherent state and, following the backward Heisenberg picture approach, the state of the photons generated at the fundamental field frequency is also pure, and the corresponding density matrix can be constructed simply as

$$\rho = |\text{II}\rangle \langle \text{II}|. \quad (4.20)$$

Although the collection bandwidth is very small also in this case here we are interested in both the spectral and path correlations contained in the BWF

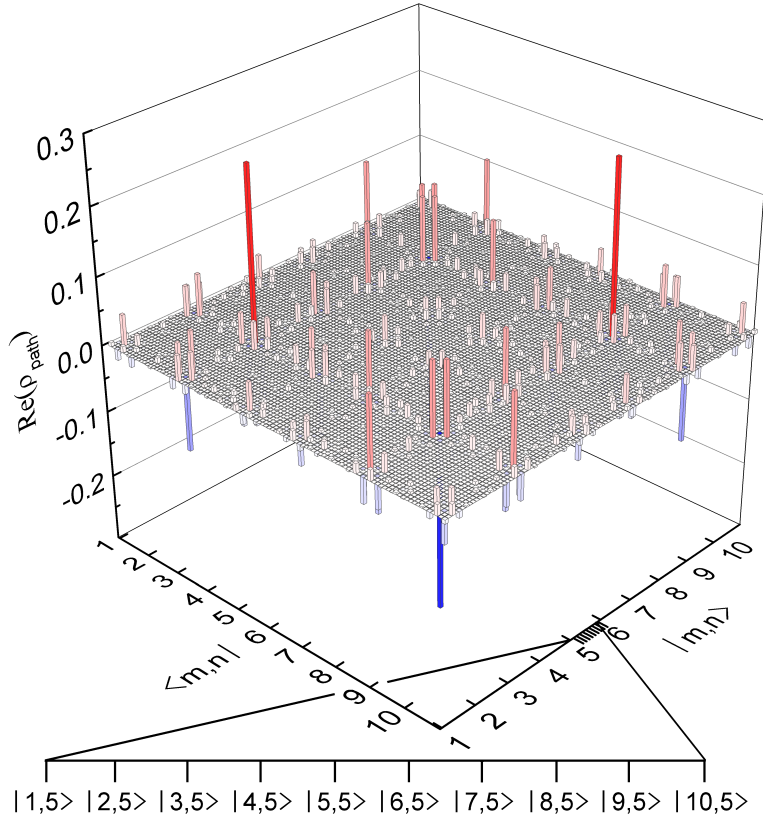


Figure 4.2: Real part of the reduced path density matrix in the case of the unperturbed structure

$\psi_{i,j}(\omega_1, \omega_2)$, thus the first property that we study is the level of entanglement between these two DOFs. As discussed at the end of Ch. 2 a direct measure of this entanglement is given by the *purity* of the reduced state in either one of the DOFs. In our simulation we follow this method and calculate the reduced density matrix in path ρ_{path} defined as

$$\rho_{\text{path}} = \int d\omega_1 d\omega_2 \langle \omega_1, \omega_2 | \rho | \omega_1, \omega_2 \rangle, \quad (4.21)$$

by tracing over the frequencies. In Fig. 4.2 we show the real part of ρ_{path} and from it the purity of the path-only state can be readily calculated as

$$P_{\text{path}} = \text{Tr} [\rho_{\text{path}}^2]. \quad (4.22)$$

In general, when the BWF of the full state (4.18) cannot be factorized, tracing over one of the DOFs lead to a reduced mixed state and this is reflected by

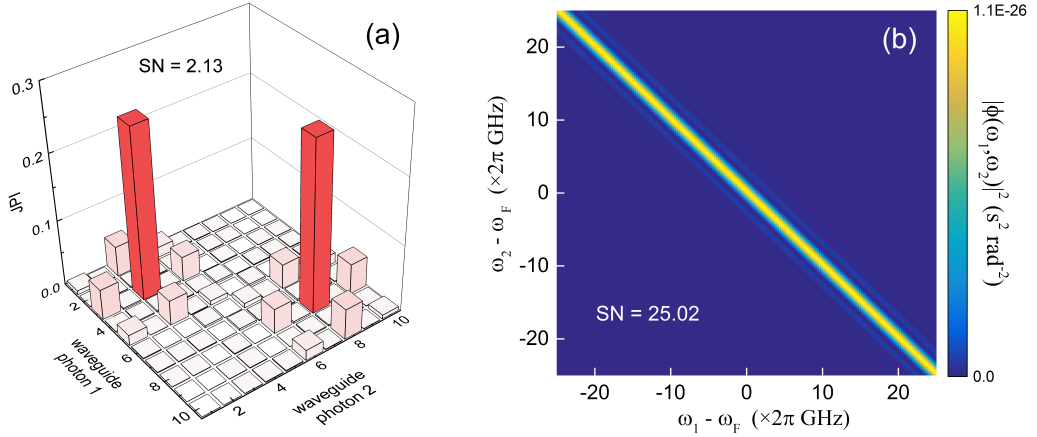


Figure 4.3: (a) Joint path intensity giving the probability of finding two photons in the waveguides i and j regardless their energy. (b) Joint spectral density of the generated photons over the collection bandwidth. Photon pairs are entangled both in *path* and *frequency* as indicated by their respective Schmidt numbers.

a value of its purity that is appreciably different from unity. In contrast, a purity equal to 1 corresponds to a separable state that can be written as the direct product of two pure states in their respective Hilbert spaces, since the two DOFs are not entangled. In our case we find $P_{\text{path}} = 0.999997$, indicating that the state in the *path* Hilbert space can be considered pure, and the same is therefore true for the state in the *frequency* Hilbert space. Thus, we can rewrite the state (4.18) as

$$|\text{II}\rangle = \frac{1}{\sqrt{2}} \int_0^\infty d\omega_1 d\omega_2 \bar{\psi}(\omega_1, \omega_2) |\omega_1, \omega_2\rangle \otimes \sum_{i,j=1}^{10} \xi_{ij} |i, j\rangle, \quad (4.23)$$

where the ξ_{ij} describe the path correlations and enter into the matrix elements $(\rho_{\text{path}})_{lm}$ as $\xi_{lj}\xi_{im}^*$, with implicit summation over the repeated index. The function $\bar{\psi}(\omega_1, \omega_2)$ is the BWF describing the spectral correlations of any of the generated photon pairs, regardless the exiting waveguides.

Since the path and frequency states composing (4.23) are pure we can study their properties independently, analyzing the entanglement between the two photons in each DOF. For a pure state this can be measured in terms of the Schmidt number (SN) [35], which assumes values larger than 1 when the generated photons are entangled. Focusing on the path DOF, for our pumping conditions we find $\text{SN}_{\text{path}} = 2.13$, which demonstrate *path entanglement* between at least two modes. This value is expected when looking

at the joint path intensity (JPI) reported in Fig. 4.3 (a), which describes the joint probability of measuring one photon exiting the i -th waveguide with the other one exiting the j -th waveguide, and whose elements correspond to the diagonal entries of ρ_{path} rearranged in a 10×10 matrix. Its shape suggests strong *path correlations* of the generated photons exiting the waveguides 3 and 8. This result resembles that reported in [17], in which an array with two isolated topological defects, each of which is associated with a topological mode, has been studied. Blanco-Redondo and coworkers predicted that path-entangled photons can be generated by SFWM when these two uncoupled modes are pumped coherently. Beside the process used for the generation of photon pairs (i.e SPDC vs. SFWM), in our work the situation is different for at least two reasons: (i) the dual-pump scheme we adopt is used to pump a *single* topological mode, the odd one; (ii) in our case the two photons are generated in two different topological modes, which are the result of strong coupling of the two topological defects.

Turning to the spectral properties of the generated photons, we can study directly the correlations contained in $\bar{\psi}(\omega_1, \omega_2)$, which is by all means equivalent to the spectral BWF describing the pairs that would be generated in one of the waveguides of the array taken as isolated. In Fig. 4.3 (b) we show the joint spectral density (JSD) (i.e. $|\bar{\psi}(\omega_1, \omega_2)|^2$), where $|\bar{\psi}(\omega_1, \omega_2)|^2 d\omega_1 d\omega_2$ gives the joint probability of finding two photons with frequency between ω_1 and $\omega_1 + d\omega_1$ and between ω_2 and $\omega_2 + d\omega_2$, respectively. As usual, the properties of the JSD are determined by the spectral width of the pump and the phase matching bandwidth. The first one is tiny since we considered a long pump pulse, while the second one is very large compared to both the generation bandwidth and the pump spectral width. This results in the stretched shape of the JSD reported in Fig. 4.3 (b), which is typical of photons correlated in energy. With the parameters considered in our simulation we find a $\text{SN}_{\text{freq}} = 25$, confirming that the generated photons are also *frequency entangled*. These results together demonstrate that, in this specific structure, one can generate photon pairs that are entangled in both path and frequency but at the same time these two DOFs are uncorrelated. Thus, the state in (4.23) is an *hyper-entangled state* [55, 56].

4.3 TOPOLOGICAL PROTECTION OF THE QUANTUM STATE

It has been demonstrated theoretically[47] in Ch. 3 that in the case of SFWM and in the presence of disorder that preserves the structure topology, quan-

tum correlations of the generated pairs are less robust than the linear properties of the system. This could be explained in terms of the nonlinear coupling of the topological modes with the other modes supported by the structure. Here we want to understand what happens in the case of photons generated by SPDC and in an hyper-entangled state. We perform an analysis of disorder on the properties of the generated state focusing on three main quantities: (i) state purity, which is central in the definition of the hyper-entangled state; (ii) state fidelity with respect to the state generated in the unperturbed structure; (iii) state SNs. We recall from the study of the linear properties of the topological modes that the type of disorder is *positional*, and thus it modifies the relative position of the waveguides, and thus the gaps, along the horizontal direction x [Fig. 4.1 (a)]. As consequence, the relative coupling constants $\sigma(\omega)$ in the matrix $\Sigma(\omega)$ change as [see Eq. (1.8)]

$$\sigma(d, \omega) = \sigma_{\omega_0}(d) + \gamma_{\omega_0}(d) (\omega - \omega_0), \quad (4.24)$$

where ω_0 is either the fundamental or the pump frequency corresponding to λ_F and λ_P , respectively, and the coefficients $\sigma_{\omega_0}(d)$ and $\gamma_{\omega_0}(d)$ follow the fit curves of Fig. 1.3 (c) and Figs. 1.4 (a-b), respectively. The positional disorder modifies the relative position of the waveguides in the original structure by an amount that follows a Gaussian distribution with a mean $\mu = 0$ and a standard deviation σ ranging from 0 to 40 nm. For each level of disorder we create an ensemble with the appropriate number of realizations so that all the quantities calculated are statistically meaningful. In practice, we consider ensembles of $N_\sigma = 300$, $N_\sigma = 750$, and $N_\sigma = 1000$ realizations for disorder $0 < \sigma < 20$ nm, $\sigma = 30$ nm, and $\sigma = 40$ nm, respectively.

We start by studying the effects of disorder on the purity of the reduced path state calculated from ρ_{path} in (4.22). In Fig. 4.4 (a) we show the trend for the average purity, which overall maintains a high value for all levels of disorder. In particular, for $\sigma < 20$ nm the effects are barely noticeable and the average purity is above 0.99, thus demonstrating that the separability of the full state is well-preserved. In this range of disorder the frequency dependence of the coupling constants is not yet evident on the properties of the generated state when averaged on the ensemble, however the variance starts to increase considerably, suggesting that in a small number of cases in the ensemble there is a moderate modification of the coupling constants within the collection bandwidth (50 GHz). On the contrary, for larger values of σ the average purity starts decreasing down to 0.98. This trend can be explained by observing that, as σ increases so does the probability of having waveguides closer to each others. In this case, the frequency dependence of the coupling coefficients becomes significant within our collection bandwidth,

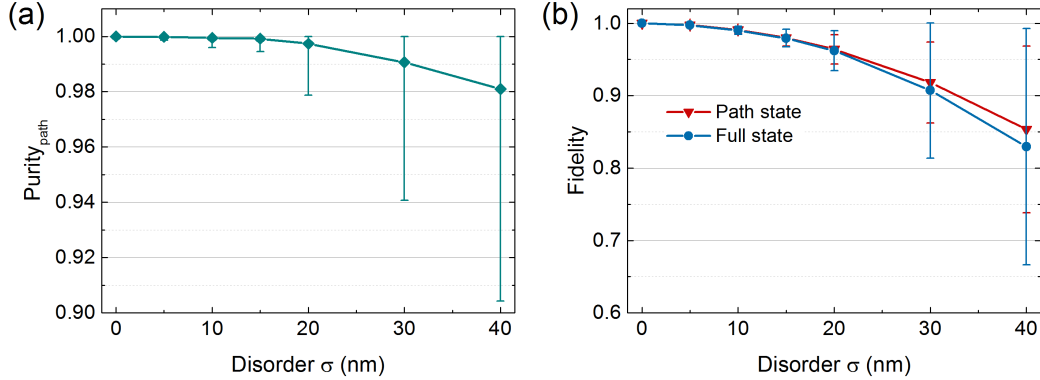


Figure 4.4: (a) Average purity calculated from the reduced path density matrix ρ_{path} , the values are well above 0.99 for low levels of disorder. (b) Average fidelities of the reduced path state and the complete state showing that almost all of the effect of disorder impact the path DOF.

leading to observable weak path and frequency correlations.

More information on the effect of disorder on both the path and frequency DOFs comes from the fidelity of the generated state with respect to the case with no disorder. In Fig. 4.4 (b) we show the average fidelity of the full state of Eq. (4.18) and the reduced path state. The first striking feature is that path and full fidelity are almost the same and perfectly overlapping for low levels of disorder, which means that the full fidelity is determined only by that of the path state, while energy correlations are essentially unaffected in the range of disorder considered here. These results are consistent with what discussed above for the purity. The second important result is that for $\sigma < 20$ nm fidelities are above 0.95 and with a small variance, while they reduce down to around 0.85 with larger variances as σ increases. The fidelity trend is similar to what observed in Ch. 3 [47] for SFWM, in which a change of fidelity was related to the nonlinear coupling of the topologically protected mode with other modes of the waveguide array. However, a deeper analysis reveals that in the case of SPDC the situation is different.

Investigating the distribution of the path fidelity and SN_{path} gives an insight of what is happening in the generated state as disorder in the structure increases. In Fig. 4.5 we show the distribution of all the elements in the ensembles for $\sigma = 10, 20, 30$, and 40 nm. The first feature that we note is that, unlike the case of SFWM treated in Ch. 3 [47], in which the average SN_{path} was increasing with disorder, here the average $\text{SN}_{\text{path}} \simeq 2.13$ and is independent of σ , with values indicating either higher or lower path correlation. One can observe that for $\sigma < 20$ nm the points of the ensemble are tightly

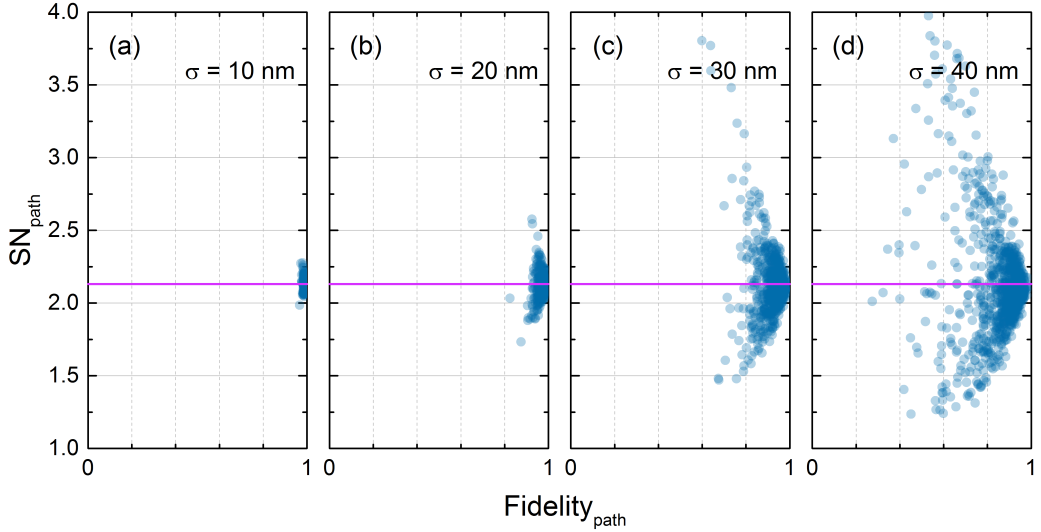


Figure 4.5: Distribution of path fidelity and SN_{path} of the ensembles for increasing levels of disorder. The ensemble sizes are $N_\sigma = 300$ for $\sigma = 10, 20$ nm (a) and (b), $N_\sigma = 750$ for $\sigma = 30$ nm (c), and $N_\sigma = 1000$ for $\sigma = 40$ nm (d). In each graph the solid line indicates the average SN for each ensemble.

clustered around their average, which is consistent with an SPDC process in which photon pairs are essentially all generated in the topological modes and their state is hyper-entangled. On the contrary, for larger values of σ the cluster begins to spread and realizations of the ensemble with fidelity lower than 0.95 can lead to generated states with lower or higher SN_{path} . This is the reason for the stability in the average SN_{path} compared to the case of SFWM, where we start from an unperturbed path state with $SN_{\text{path}} = 1$ and disorder can only modify this value upwards.

By Schmidt decomposing each state of the ensembles, we find that photons pairs are essentially always generated in the two topologically protected modes regardless the level of disorder. Thus, the effect of disorder is mainly that of reducing the structure symmetry and changing the weight of each topological mode in the Schmidt decomposition. This effect is illustrated in Fig. 4.6 where we show the coefficients of the Schmidt decomposition for the unperturbed structure and for $\sigma = 40$ nm. Even for the largest value of disorder the first two coefficients together accounts, on average, for almost all the weight in the decomposition. Their corresponding Schmidt modes have the same field distribution of the topological modes when the structure is unperturbed. However when disorder modifies the structure their symmetry is reduced and one of them is favoured to the other in the generation

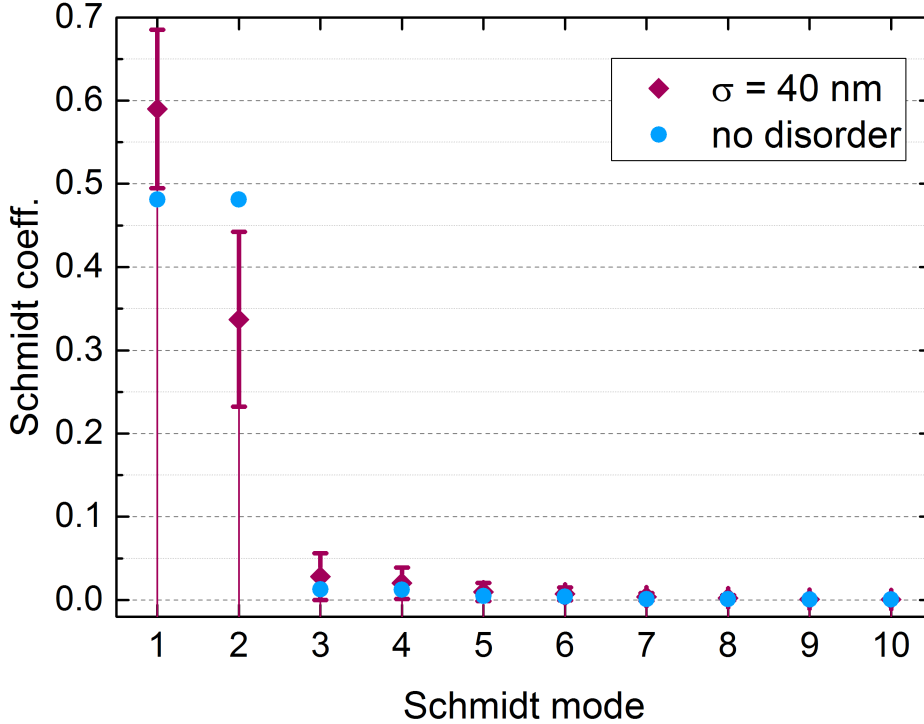


Figure 4.6: Schmidt coefficients in the decomposition without disorder and for $\sigma = 40$ nm. Photons are generated, on average, in the two Schmidt modes associated to the topological modes, however disorder reduces the structure symmetry and the relative weight of the Schmidt modes.

of the photon pair. This mechanism leads to lower SN_{path} corresponding to realizations in which the JPI presents uneven peaks associated to photons exiting the waveguides 3 and 8. Naturally, the generation of photon pairs in other modes of the structure is still possible, but less probable, as suggested by the average value of the other coefficients in the decomposition with respect to the unperturbed case. Indeed, in SPDC phase-matching condition and efficient nonlinear overlap of the fields involved in the process are more difficult to achieve simultaneously than in the SFWM case [47]. This becomes clear by noting that the SPDC process involving only non topological modes is completely suppressed, compared to its SFWM analog, because the different distribution of the propagation constants at λ_P and λ_F leads to a large phase mismatch. This suggests that, in the degradation of the hyper-entangled state, the spurious nonlinear coupling that is dominant involves the topological mode at λ_P and non-topological modes at λ_F , for in this case the different distribution in the propagation constant has a minimal impact,

since the topological mode always sits at the center of the band gap, both at λ_P and λ_F , with the other modes symmetrically distributed around it.

4.4 CONCLUSIONS

The results presented in this chapter, together with those on the linear properties in Ch. 1, constitute an additional step towards the understanding of the topological properties of a photonic system. Our work is based on a systematic study of the generation of photon pairs by SPDC in a one-dimensional array, composed of lithium-niobate waveguides, that supports two strongly coupled topologically protected modes. The quantum state representing each generated photon pair is described in the path and frequency DOFs, and we demonstrate that the two photons are entangled in both of them, but the DOFs are not correlated to each other, thus resulting in an hyper-entangled state whose properties are expected to be topologically protected since photons are generated mainly in the two topological modes.

We investigated the effect of positional disorder up to $\sigma = 40$ nm, taking into account also the frequency dependence of the coupling coefficients between waveguides. We focused on both the path and frequency quantum correlations of the generated photons by means of a statistical analysis on different figures of merit which included: the purity of the reduced state in path, which is of fundamental importance for the definition of the hyper-entanglement; the fidelity of the full and path two-photon state; and the path Schmidt number. We showed that, for $\sigma < 20$ nm topological protection of the generated state is *robust* against positional disorder for this type of structure, displaying a behaviour similar to our findings in the SFWM case. For larger values of σ , however, such a protection can decrease substantially as shown by the rapid degradation of fidelity and the spread in the cluster distribution of the SN_{path} and fidelity. In particular, the quantitative analysis of these two quantities, together with the Schmidt decomposition of the path state, showed that correlations either decrease due to disorder lowering the symmetry of the structure, or increase due to the small probability of SPDC involving other modes that are not topological.

In conclusion we demonstrated also in this case that the topological protection is far more effective in the linear regime than in the nonlinear interaction, although in principle we hoped that the much stringent constraints in SPDC could mitigate the problems observed in the SFWM case. This appeared to be only partially true, for a different phenomenon was responsible for the degradation of the generated state, and it was connected to the symmetry of the structure and the weight of the Schmidt modes in which

photons are generated. Finally, since topological protection diminish with continuity as disorder is increased, one can still find it useful if the expected level of disorder falls in a range where the properties of the generated state can still be considered acceptable for practical application.

5 BEYOND PHOTON PAIRS: SQUEEZED STATES

The generation of photon pairs by parametric fluorescence, either via spontaneous four-wave mixing (SFWM) or spontaneous parametric down conversion (SPDC), is certainly one of the most studied nonlinear optical processes for the generation of quantum states of light. This interest stems from the accessibility of the physical process, which makes photon pairs a convenient tool to study quantum correlations, and from the viability of photon pairs quantum state as the building block on which new quantum technologies can be developed in many fields, from communication and computation to sensing and metrology. Although photon pair generation has been the main focus in photonics starting from the second half of the past century, around the same years the theoretical development on more general quantum states of light was already well established. In particular, a large literature on so-called *squeezed states* of light was present despite experimental challenges prevented their direct observation, which was first achieved only in 1985 using four-wave mixing in an atomic vapour of atoms [12].

Squeezed states are characterized by a very peculiar property, for they allow to perform measurements on one observable with a level of noise below the quantum limit imposed by the Heisenberg uncertainty principle, at the expense of the noise on other non-commuting observables. Initial studies focused on the squeezing of conjugated quadrature amplitudes representing the real and imaginary part of the light field, but squeezing of other quantities, such as the photon number, has also been studied. The use of squeezed state has been envisaged as promising method to perform sensible detection of weak forces like gravitational waves[57], which remains the most prominent application, although other interesting uses include continuous variable quantum computing[58], and quantum imaging techniques[59].

Here we present an approach to treat the generation of squeezed states via SPDC in a simple waveguide, which represents the first step towards the study of squeezed light generation in waveguide array supporting topological

modes.

5.1 INTRODUCTION TO SQUEEZED STATES

We have seen in the previous chapters that, as a result of the nonlinear light-matter interaction, photon pairs can be created either by SFWM or SPDC when a strong pump field propagates in the medium. The meaning of the term 'strong' was used to put in perspective the weakness of these nonlinear processes and the necessity to use coherent light sources, such as lasers, to achieve large field intensities into the material. The enhancement of the pump field is then further increased in integrated photonics by confining light spatially in guided modes and, if necessary, also temporally in resonating structures. Although these techniques are useful to enhance the generation of photon pairs, the possibility to define a quantum state describing the two generated photon is valid only when the generation probability per pump pulse is very small compared to 1. Indeed, we have seen in Ch. 2 that starting from an initial coherent state that describes the pump photons, following the backward Heisenberg picture the generated state is

$$|\psi_{\text{gen}}\rangle = e^{\beta C_{\text{II}}^\dagger - \text{H.c.}} |\text{vac}\rangle, \quad (5.1)$$

where $|\text{vac}\rangle$ is the vacuum state, C_{II}^\dagger is the operator that creates two photons, and β is the constant that normalizes the bi-photon wave function inside C_{II}^\dagger . The Eq. (5.1), which is valid assuming that the pump field is not depleted, can be approximated to the more familiar form

$$|\psi_{\text{gen}}\rangle \approx |\text{vac}\rangle + \beta C_{\text{II}}^\dagger |\text{vac}\rangle + \dots, \quad (5.2)$$

when $|\beta|^2 \ll 1$, and this was effectively the case in our work where $|\beta|^2 \approx 10^{-5} - 10^{-6}$. In this regime most of the times the generated state is the vacuum with no photons and occasionally a pair is generated by the pump pulse, with negligible probability of observing the generation of additional pairs since these events scale with $|\beta|^4$, $|\beta|^6$ and so on. However when we begin to increase significantly the pump power and thus the average number of photons $|\alpha|^2$ contained in it, the values assumed by $|\beta|^2$ also start to increase, either linearly or quadratically with $|\alpha|^2$ if the process considered is SPDC or SFWM, respectively. At some point, if the values are not very far from unity, approximations of the kind (5.2) are incorrect and one has to consider (5.1) again.

A state like that of Eq. (5.1) is a generalization of a particular quantum state of light called *squeezed state*, which is very well known in quantum optics

and has some very peculiar properties that we now expose. To simplify the explanation we consider the generation of two degenerate photons in the same frequency mode, which for example one can think as the result of the degenerate SPDC process. In this case the associated Hamiltonian can be written as

$$\mathcal{H} = i\hbar \left(ga^{\dagger 2} - g^* a^2 \right), \quad (5.3)$$

where g is a complex number and a is the usual annihilation operator. Following the time evolution of the initial vacuum state $|\text{vac}\rangle$ in the Schrödinger picture we can then define [60] a unitary squeezing operator

$$S(\xi) = \exp \left(\frac{1}{2} \xi^* a^2 - \frac{1}{2} \xi a^{\dagger 2} \right), \quad (5.4)$$

that acting on $|\text{vac}\rangle$ produce the squeezed state

$$|\xi\rangle = \exp \left(\frac{1}{2} \xi^* a^2 - \frac{1}{2} \xi a^{\dagger 2} \right) |\text{vac}\rangle \quad (5.5)$$

where $\xi = r e^{i\theta}$ is a complex value. To understand what is actually 'squeezed' in $|\xi\rangle$ we consider the single mode electric field operator

$$\mathbf{E}(t) = \mathcal{E} \hat{\mathbf{e}} \left(a e^{-i\nu t} + a^\dagger e^{i\nu t} \right), \quad (5.6)$$

at the frequency ν , with amplitude \mathcal{E} , where $\hat{\mathbf{e}}$ is a versor and a, a^\dagger satisfy the commutation relation $[a, a^\dagger] = 1$. Then, we define a pair of Hermitian *quadrature* operators X_1 and X_2 as

$$\begin{aligned} X_1 &= \frac{1}{2} (a + a^\dagger) \\ X_2 &= \frac{1}{2i} (a - a^\dagger), \end{aligned} \quad (5.7)$$

that satisfy the commutation relation $[X_1, X_2] = i/2$ and represent the two quadrature amplitudes of the field operator, which can be rewritten as

$$\mathbf{E}(t) = 2\mathcal{E} \hat{\mathbf{e}} (X_1 \cos(\nu t) + X_2 \sin(\nu t)). \quad (5.8)$$

If we apply the Heisenberg uncertainty principle to this pair of Hermitian operators we have that

$$\begin{aligned} \Delta X_1 \Delta X_2 &\geq \frac{1}{2} |\langle [X_1, X_2] \rangle| \\ &\geq \frac{1}{4}, \end{aligned} \quad (5.9)$$

and if the equality relation applies, then the state on which the ΔX_i are calculated is of *minimum uncertainty*. This lower bound identified by the Heisenberg uncertainty principle represents a limit in the measurement process of two non-commuting observables of a quantum system. It is intrinsically connected to the quantum nature of the physical object and does not depend on our ability to build more precise instruments. In practice, quantum mechanics prevents us from knowing, at the same time and with arbitrary precision, some properties of a physical object, thus putting a *quantum limit* to the uncertainty of our measurements. Despite this limitation there are situations where we are interested in just one of the two conjugate observables. In all these cases we can play with the Heisenberg principle, without violating it, to attain a better condition for the observable that we want to measure, while we give up on the other. An example of this is found for a state called "squeezed", where the uncertainty in one of the two quadratures is lowered below the quantum limit, that is we have

$$(\Delta X_i)^2 \equiv \langle X_i^2 \rangle - (\langle X_i \rangle)^2 < \frac{1}{4}, \quad (5.10)$$

with quantum noise removed from one observable at the expense of more uncertainty in the other one, which increases in order to satisfy the Heisenberg uncertainty principle. For a *coherent* state $|\alpha\rangle$, which is the quantum state of radiation that most closely describe a classical field and is defined as the eigenstate of the annihilation operator

$$a|\alpha\rangle = \alpha|\alpha\rangle, \quad (5.11)$$

the expectation values of X_1 and X_2 give the real and imaginary parts of α , so the state effectively describes a field of intensity $|\alpha|^2$ as we used for our laser pump. The uncertainties $(\Delta X_i)^2$ are both equal to $1/4$ so the coherent state is of minimum uncertainty as it is expected for the quantum description of a "classical" field. In contrast, for Fock number states $|n\rangle$, which are eigenstates of the number operator $a^\dagger a$, the expectation values $\langle X_1 \rangle$ and $\langle X_2 \rangle$ are equal to 0 and their uncertainties $(\Delta X_i)^2$ grow with n . If we focus on our squeezed vacuum state (5.5) we can calculate all the needed quantities if we know how the operators a and a^\dagger are transformed by $S(\xi)$, one can find expanding the exponentiated operator

$$\begin{aligned} S^\dagger(\xi)aS(\xi) &= a \cosh r - a^\dagger e^{i\theta} \sinh r \\ S^\dagger(\xi)a^\dagger S(\xi) &= a^\dagger \cosh r - a e^{-i\theta} \sinh r. \end{aligned} \quad (5.12)$$

Since the result is just a superposition of the original a and a^\dagger operators we see that the expectation values of $\langle X_1 \rangle$ and $\langle X_2 \rangle$ are also equal to 0, and

then the uncertainties $(\Delta X_i)^2$ are determined only by $\langle X_i^2 \rangle$. Without loss of generality we can put $\theta = 0$ (or consider rotated quadrature operators) to find

$$\begin{aligned} (\Delta X_1)^2 &= \frac{1}{4}e^{-2r} \\ (\Delta X_2)^2 &= \frac{1}{4}e^{2r}. \end{aligned} \quad (5.13)$$

For values different from 0 of the squeezing parameter r one of the two quadratures is reduced by a factor $\exp(-2r)$ compared to the minimum quantum noise while the other increases by the same amount. Typically, in literature a *squeezing factor* is defined as

$$-10 \log_{10} \left(\frac{(\Delta X)_\xi^2}{(\Delta X)_{\text{vac}}^2} \right) \equiv -10 \log_{10} (e^{-2r}), \quad (5.14)$$

for the rotated quadrature X with the lowest uncertainty, which is X_1 in our example with squeezing angle $\theta = 0$. Finally, we note using Eqs. (5.12) that the squeezed vacuum state has photons since the average number

$$\langle \xi | a^\dagger a | \xi \rangle = \sinh^2 r, \quad (5.15)$$

is different from zero.

5.2 CHANNEL OPERATOR FORMALISM

To introduce the formalism of channel operators we refer to the case of SPDC process in a lithium niobate waveguide with the same geometric parameters as that forming the array studied in the previous chapter, and propagating in the y direction. We take $\mathbf{D}(\mathbf{r}, t)$ as the fundamental field and we consider the strong field $\mathbf{D}_c(\mathbf{r}, t)$ propagating at the second harmonic (S) frequency as classical, while the field at the fundamental (F) frequency $\mathbf{D}_q(\mathbf{r}, t)$ is quantized in the usual way. We have

$$\begin{aligned} \mathbf{D}_q(\mathbf{r}, t) &= \int \sqrt{\frac{\hbar\omega_F(k)}{4\pi}} a(k, t) \mathbf{d}_F(x, z; k) e^{iky} dk + \text{H.c.} \\ \mathbf{D}_c(\mathbf{r}, t) &= \alpha \int \sqrt{\frac{\hbar\omega_S(k)}{4\pi}} p(k, t) \mathbf{d}_S(x, z; k) e^{iky} dk + \text{c.c.} \end{aligned} \quad (5.16)$$

where $\mathbf{d}_{F(S)}(x, z; k)$ is the normalized field distribution in the plane orthogonal to the propagation direction, k is the wavevector ranging on positive

numbers, and $a(k, t)$ is the usual annihilation operator satisfying the equal-time commutation relations

$$\begin{aligned} [a(k, t), a(k', t)] &= 0, \\ [a(k, t), a^\dagger(k', t)] &= \delta(k - k'), \end{aligned} \quad (5.17)$$

and $p(k, t)$ is a complex function with the same units as $a_F(k, t)$ that describes the amplitude spectrum of the pump field, and $|\alpha|^2$ has the meaning of average number of photons in the pump field. Finally, the Hamiltonian of the system is

$$\mathcal{H} = \int \hbar\omega_F(k) a^\dagger(k, t) a(k, t) dk + E_c \quad (5.18)$$

where E_c is a real number corresponding to the energy of the classical field

$$E_c = |\alpha|^2 \int \hbar\omega_S(k) |p(k, t)|^2 dk. \quad (5.19)$$

If the dispersion of the modes considered at the fundamental and second harmonic frequency is not so strong we can expand it to the second order in k as

$$\omega(k) = \omega(k_0) + v_g(k - k_0) + \frac{1}{2}\bar{\beta}(k - k_0)^2, \quad (5.20)$$

where $k_0 = k(\omega_0)$ for either the fundamental $\omega_0 = \omega_F$ or second harmonic $\omega_0 = \omega_S$ central frequency, $v_g = (d\omega/dk)|_{k_0}$ is the group velocity at k_0 , and $\bar{\beta}$ is connected to the usual group velocity dispersion parameter $\beta_2 = (d^2k/d\omega^2)|_{\omega_0}$ through the relation $\bar{\beta} = -\beta_2 v_g^3$. The zeroth order approximation the fields with this dispersion can be written as

$$\begin{aligned} \mathbf{D}_q(\mathbf{r}, t) &\approx \sqrt{\frac{\hbar\omega_F}{2}} \mathbf{d}_F(x, z; k_{\omega_F}) \int a(k, t) \frac{e^{iky}}{\sqrt{2\pi}} dk + \text{H.c.}, \\ \mathbf{D}_c(\mathbf{r}, t) &\approx \alpha \sqrt{\frac{\hbar\omega_S}{2}} \mathbf{d}_S(x, z; k_{\omega_S}) \int p(k, t) \frac{e^{iky}}{\sqrt{2\pi}} dk + \text{c.c.}, \end{aligned} \quad (5.21)$$

and we can introduce the *channel field operator* for the quantized field at fundamental frequency as

$$\psi(y, t) = \int \frac{dk}{\sqrt{2\pi}} a(k, t) e^{i(k - k_{\omega_F})y}, \quad (5.22)$$

and in the same way we define

$$p(y, t) = \int \frac{dk}{\sqrt{2\pi}} p(k, t) e^{i(k - k_{\omega_S})y}, \quad (5.23)$$

which can be considered the real space amplitude of the pump along the waveguide. Both (5.22) and (5.23) have units of $[L^{-1/2}]$ and we can use them to rewrite the fields in (5.21) as

$$\begin{aligned} \mathbf{D}_q(\mathbf{r}, t) &\approx \sqrt{\frac{\hbar\omega_F}{2}} \mathbf{d}_F(x, z; k_{\omega_F}) \psi(y, t) e^{ik_{\omega_F}y} + \text{H.c.} \\ \mathbf{D}_c(\mathbf{r}, t) &\approx \alpha \sqrt{\frac{\hbar\omega_S}{2}} \mathbf{d}_S(x, z; k_{\omega_S}) p(y, t) e^{ik_{\omega_S}y} + \text{c.c.} \end{aligned} \quad (5.24)$$

For our purpose of studying photons generated in a squeezed state, we are interested in the time evolution of the channel field operators (5.22). This follows the usual operator evolution in the Heisenberg picture, that is

$$\frac{d\psi(y, t)}{dt} = \frac{1}{i\hbar} [\psi(y, t), \mathcal{H}], \quad (5.25)$$

where, using (5.17), the channel operators satisfy the commutation relations

$$\begin{aligned} [\psi(x, t), \psi(x', t)] &= 0, \\ [\psi(x, t), \psi^\dagger(x', t)] &= \delta(x - x'), \end{aligned} \quad (5.26)$$

and the full Hamiltonian is composed of a linear piece describing the energy in the waveguide, which can be written in terms of channel operators as

$$\begin{aligned} \mathcal{H}_L &= \hbar\omega_F \int \psi^\dagger(y, t) \psi(y, t) dy + E_c \\ &\quad - \frac{1}{2} i\hbar v_g \int \left(\psi^\dagger(y, t) \frac{\partial \psi(y, t)}{\partial y} - \frac{\partial \psi^\dagger(y, t)}{\partial y} \psi(y, t) \right) dy \\ &\quad - \frac{\hbar}{4} \bar{\beta} \int \frac{\partial^2 \psi^\dagger(y, t)}{\partial y^2} \psi(y, t) + \psi^\dagger(y, t) \frac{\partial^2 \psi(y, t)}{\partial y^2} dy, \end{aligned} \quad (5.27)$$

and a nonlinear piece, derived from the second order nonlinear Hamiltonian of Ch. 2, that describes the SPDC interaction. We can write it as

$$\mathcal{H}_{\text{NL}} = f_{\text{NL}} \int p(y, t) \psi^\dagger(y, t) \psi^\dagger(y, t) dy + \text{H.c.}, \quad (5.28)$$

where the nonlinear term f_{NL} is

$$f_{\text{NL}} = -\sqrt{\frac{(\hbar\omega_F)^2 (\hbar\omega_S)}{8\epsilon_0}} \frac{\alpha \bar{\chi}_2}{\bar{n}^3 \sqrt{\mathcal{A}}} \quad (5.29)$$

with all the terms having the same meaning already presented in Ch. 2 and in the appendix. Applying the dynamical equation (5.25) we find a linear differential equation describing the evolution in time of the channel operator

$$\frac{d\psi(y, t)}{dt} + i\omega_F\psi(y, t) + v_g \frac{\partial\psi(y, t)}{\partial y} - \frac{i\bar{\beta}}{2} \frac{\partial^2\psi(y, t)}{\partial y^2} = \frac{2f_{\text{NL}}}{i\hbar} p(y, t)\psi^\dagger(y, t). \quad (5.30)$$

We see that, besides involving time and space derivatives, the equation also couples the channel operator $\psi(y, t)$ with its Hermitian conjugate through the nonlinear interaction. This means that we will have to solve it together with the differential equation for $\psi^\dagger(y, t)$ analogous to (5.30). To simplify a bit this task we perform two transformations of the channel operators to reduce the terms on the left of (5.30). First, we explicitly write the fast oscillating part in $\psi(y, t)$ and $p(y, t)$ as

$$\begin{aligned} \psi(y, t) &= \bar{\psi}(y, t)e^{-i\omega_F t}, \\ p(y, t) &= \bar{p}(y, t)e^{-i\omega_S t}, \end{aligned} \quad (5.31)$$

to remove the term with the frequency factor, then we move to a reference frame shifting along the waveguide at the group velocity of the photons generated at the fundamental frequency. This is simply done by defining a new coordinate $y' = y - v_g t$ and then, applying the derivatives, the terms with the group velocity is removed. The final version of the linear differential equation is

$$\frac{\partial\phi(y, t)}{\partial t} - \frac{i\bar{\beta}}{2} \frac{\partial^2\phi(y, t)}{\partial y^2} = -im_S(y + v_g t)\phi^\dagger(y, t), \quad (5.32)$$

where we have renamed the operators in the moving frame $\psi(y, t) \rightarrow \phi(y, t)$ and the term $m_S(y + v_g t)$ containing the nonlinear interaction leads to squeezing.

5.3 GREEN FUNCTION SOLUTION

The resolution of equation (5.32) is clearly quite complicated also after the applied simplifications, moreover it's coupled with its sister Hermitian conjugate equation and, most importantly, it's a differential equation for an Hermitian operator and not for a standard complex-valued function, forcing us to adopt a strategy for its resolution. To do so, we write the system of equations as

$$\frac{\partial}{\partial t} \begin{bmatrix} \phi(y, t) \\ \phi^\dagger(y, t) \end{bmatrix} = \begin{bmatrix} \frac{i\bar{\beta}}{2} \frac{\partial^2}{\partial y^2} & -im_S(y + v_g t) \\ im_S^*(y + v_g t) & -\frac{i\bar{\beta}}{2} \frac{\partial^2}{\partial y^2} \end{bmatrix} \begin{bmatrix} \phi(y, t) \\ \phi^\dagger(y, t) \end{bmatrix} \quad (5.33)$$

and we put it in the following form

$$\frac{\partial}{\partial t} \begin{bmatrix} \phi(y_2, t) \\ \phi^\dagger(y_2, t) \end{bmatrix} = \int K^t(y_2, y_1) \begin{bmatrix} \phi(y_1, t) \\ \phi^\dagger(y_1, t) \end{bmatrix} dy_1, \quad (5.34)$$

where the kernel operator matrix $K^t(y_2, y_1)$ is

$$K^t(y_2, y_1) = \begin{bmatrix} \frac{i\bar{\beta}}{2} \frac{\partial^2}{\partial y_2^2} & -im_S(y_2 + v_g t) \\ im_S^*(y_2 + v_g t) & -\frac{i\bar{\beta}}{2} \frac{\partial^2}{\partial y_2^2} \end{bmatrix} \delta(y_2 - y_1). \quad (5.35)$$

To find a solution for the system of equations we resort to a typical method that involves the resolution of the associated system for the Green function, which in this case is a matrix itself. That is, we now want to solve the corresponding differential equation

$$\frac{\partial}{\partial t_2} G^{t_2 t_1}(y_2, y_1) = \int K^{t_2}(y_2, y_3) G^{t_2 t_1}(y_3, y_1) dy_3, \quad (5.36)$$

where we have introduced the 2×2 Green function matrix

$$G^{t_2 t_1}(y_2, y_1) = \begin{bmatrix} g_{11}^{t_2 t_1}(y_2, y_1) & g_{12}^{t_2 t_1}(y_2, y_1) \\ g_{21}^{t_2 t_1}(y_2, y_1) & g_{22}^{t_2 t_1}(y_2, y_1) \end{bmatrix}, \quad (5.37)$$

in which the elements $g_{ij}^{t_2 t_1}(y_2, y_1)$ are complex functions of y_1, y_2, t_1 and t_2 , and the equation is subjected to the equal-time initial condition

$$G^{t,t}(y_2, y_1) = \begin{bmatrix} \delta(y_2 - y_1) & 0 \\ 0 & \delta(y_2 - y_1) \end{bmatrix}. \quad (5.38)$$

The powerful idea behind this method takes advantage of the linearity of the operator and the property of the Dirac delta $\delta(y_2 - y_1)$. Since the Green function of equation (5.36) is the solution of the linear system for an impulse initial condition centered in y_1 , one can recover the solution of the original system of equation for the operators by summing all the contribution obtained varying the position of the initial Delta function. We find

$$\begin{bmatrix} \phi(y_2, t) \\ \phi^\dagger(y_2, t) \end{bmatrix} = \int G^{t, t_0}(y_2, y_1) \begin{bmatrix} \phi(y_1, y_0) \\ \phi^\dagger(y_1, y_0) \end{bmatrix} dy_1, \quad (5.39)$$

where t_0 and t are the initial and final time of the operators evolution.

Now we focus on solving the equation (5.36), which can be written explicitly in matrix form as

$$\frac{\partial}{\partial t} \begin{bmatrix} g_{11} & g_{12} \\ g_{21} & g_{22} \end{bmatrix} = \begin{bmatrix} \frac{i\bar{\beta}}{2} \frac{\partial^2}{\partial y_2^2} & -im_S(y_2, t) \\ im_S^*(y_2, t) & -\frac{i\bar{\beta}}{2} \frac{\partial^2}{\partial y_2^2} \end{bmatrix} \begin{bmatrix} g_{11} & g_{12} \\ g_{21} & g_{22} \end{bmatrix}, \quad (5.40)$$

where g_{ij} is a lighter notation for $g_{ij}^{t_2 t_1}(y_2, y_1)$. This task is performed numerically by resorting to the split-step method, which is a pseudospectral numerical technique commonly used for solving the nonlinear Schrödinger equation [61] and similar differential equations. All these equations are characterized by a linear differential operator, describing the dispersive part of the dynamical evolution, and a multiplicative operator which in the nonlinear Schrödinger equation is proportional to the modulus squared of the function itself. In our case it is evident that the two operators are those connected with the group velocity dispersion $\bar{\beta}$ and $m_S(y_2, t)$, respectively. As the name suggests, the split-step method advances the solution at each discretized time step by considering the evolution due to the presence of the dispersive and nonlinear parts separately, as if they acted independently. In the simplest implementation of the method, one first performs in direct space the step involving the nonlinear part. Then, the intermediate result is Fourier-transformed and the second step is performed in the reciprocal space, where the differential operator becomes multiplicative. The final result of the time step is recovered by Fourier-transforming back to the direct space.

In our numerical calculation we consider a real space domain in the y_2 variable of length $d_2 = 6$ mm. This guarantees that the Green functions g_{ij} are completely contained in it as they evolve in time and their value is ≈ 0 at the boundaries to avoid numerical artifacts. The initial condition delta function is swept over a real space window in the y_1 variable of length $d_1 = 400$ μm , and centered with respect of d_2 . Only inside this window the numerical results are meaningful. Since in (5.32) we describe a situation in which we are riding a moving reference frame shifting at a velocity v_g , the nonlinear term $m_S(y_2 + v_g t)$ moves from right to the left, passing through the d_1 window. We take $m_S(y_2 + v_g t)$ to have a length $L = 500$ μm , corresponding to a waveguide of the same length, while the pump $p(y_2 + v_g t)$ is a long square pulse of duration $\tau = 0.3$ ns and power 1 mW, which is constant over the length L . At $t_0 = 0$ the left edge of $m_S(y_2 + v_g t_0)$ is 200 μm on the right of the d_1 window, and the final simulation time t is chosen such that the right edge of $m_S(y_2 + v_g t)$ ends 200 μm on the left of d_1 . Finally, the delta function is approximated with a normalized Gaussian with $\sigma = 5 \times 10^{-2}$ μm , which we verified analytically to give a consistent result in the limit of null width, and the domain d_2 is discretized in 2^{19} points to have a good resolution of the initial Gaussian function and make use of the Fast Fourier Transform (FFT) algorithm.

At each step in time we perform the two split steps described above. The first one involves the nonlinear part and we have

$$\frac{\partial}{\partial t} \mathbf{G} = \mathbf{M} \mathbf{G}, \quad (5.41)$$

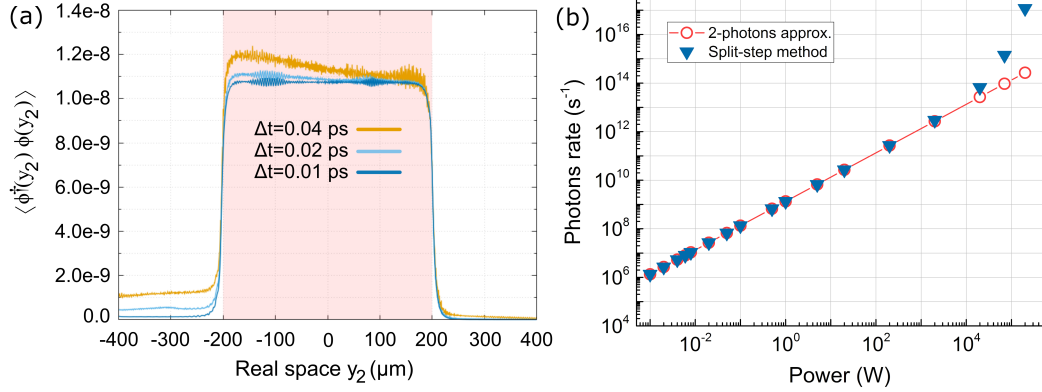


Figure 5.1: (a) Result of the split-step method at the final time t for three time steps showing the convergence of $\langle \phi^\dagger(y_2, t) \phi(y_2, t) \rangle$ to the plateau value inside the d_1 window (red). (b) Generation rate as a function of pump power compared to the case of 2-photon approximation. The trend deviates from the linear regime at high powers.

with

$$\mathbf{G} = \begin{bmatrix} g_{11} & g_{12} \\ g_{21} & g_{22} \end{bmatrix}, \quad \mathbf{M} = \begin{bmatrix} 0 & -im_S(y_2, t) \\ im_S^*(y_2, t) & 0 \end{bmatrix}, \quad (5.42)$$

which is solved at each point y_2 by diagonalizing the matrix \mathbf{M} and solving the new matrix equation

$$\frac{\partial}{\partial t} \tilde{\mathbf{G}} = \mathbf{D} \tilde{\mathbf{G}}, \quad (5.43)$$

where $\tilde{\mathbf{G}} = \mathbf{U}^{-1} \mathbf{G} \mathbf{U}$, with \mathbf{U} being the 2×2 eigenvector matrix and \mathbf{D} is the diagonal matrix containing the two eigenvalues $\lambda_{1,2} = \pm |m_S(y_2, t)|$. Then one has

$$\tilde{g}_{ij}(t + \Delta t) = e^{\lambda_i \Delta t} \tilde{g}_{ij}(t), \quad (5.44)$$

for $i, j = 1, 2$, and returns back to the matrix \mathbf{G} using \mathbf{U}^{-1} and \mathbf{U} . The second one involves the dispersion part and we have

$$\frac{\partial}{\partial t} \mathbf{G} = \mathbf{S} \mathbf{G}, \quad (5.45)$$

with the same definition for \mathbf{G} and

$$\mathbf{S} = \begin{bmatrix} \frac{i\bar{\beta}}{2} \frac{\partial^2}{\partial y_2^2} & 0 \\ 0 & -\frac{i\bar{\beta}}{2} \frac{\partial^2}{\partial y_2^2} \end{bmatrix}. \quad (5.46)$$

In this case we Fourier transform both sides of the equation, defining $\hat{g}_{ij} = \mathcal{F}[g_{ij}]$ and remembering that $\partial/\partial y \rightarrow (ik)$. The solution in the reciprocal space is

$$\begin{aligned}\hat{g}_{1j}(t + \Delta t) &= e^{-\frac{i\bar{\beta}}{2}k^2\Delta t}\hat{g}_{1j}(t), \\ \hat{g}_{2j}(t + \Delta t) &= e^{\frac{i\bar{\beta}}{2}k^2\Delta t}\hat{g}_{2j}(t),\end{aligned}\tag{5.47}$$

for $j = 1, 2$, which is then back-transformed in real space.

Once the solutions of (5.40) for each delta centered at y_1 are found, they are summed up at the corresponding time steps and provide the time evolution of the operators as defined in (5.39). Obviously, we are interested in the result at the final time step and in particular, to verify our model and method, we analyse the quantity

$$\langle \phi^\dagger(y_2, t)\phi(y_2, t) \rangle = \int dy_1 g_{21}^t(y_2, y_1)g_{12}^t(y_2, y_1),\tag{5.48}$$

which, according to the definition of the operators, gives the average number of generated photons per unit length. In Fig. 5.1(a) we show the result of a split-step method simulation for a power of 1 mW performed using three different steps in time. The value of $\langle \phi^\dagger(y_2, t)\phi(y_2, t) \rangle$ converges to a constant plateau inside the d_1 window where we swept the $\delta(y_2 - y_1)$, which is the region where results have physical meaning. A direct comparison with the approximate regime of photon pair generation can be performed by multiplying $\langle \phi^\dagger(y_2, t)\phi(y_2, t) \rangle$ with the group velocity v_g to get the rate of generated photons. For values of the pump power that don't increase the nonlinear term $m_S(y_2, t)$ significantly the split-step method should give the same result as the photon pair generation regime obtained in the backward-Heisenberg approach of the previous chapters. We show this comparison in Fig. 5.1(b) where the agreement between the two methods extends for a large range of powers. This is understandable since we are working with a non resonant structure of small length where the only enhancement of the field comes from the confinement of light in the waveguide material. Nevertheless, when the pump is sufficiently strong the split-step method correctly predicts the deviation from the linear trend, indicating that more than one pair of photon per pulse is generated. This behaviour can be obtained for more realistic power values by considering a longer structure and a material with a stronger χ_2 nonlinearity, such as gallium arsenide, since the generation rate scales with the square of both these parameters.

5.4 CHANNEL COUPLING AND FURTHER DEVELOPMENTS

The introduction of additional waveguides to describe a physical situation in which squeezed light is generated in an array is in general straightforward. Our linear Hamiltonian of Eq. (5.27), which is now valid for a generic channel J , needs an additional term that accounts for the coupling with adjacent channels. This term describes the exchange of field energy from one channel to its closest neighbors at the fundamental frequencies, and we can write it intuitively as

$$\begin{aligned} \mathcal{H}_C = & \sum_{J=1}^N c_{J,J+1} \int \psi_{J+1}^\dagger(y,t) \psi_J(y,t) dy \\ & + c_{J,J-1} \int \psi_{J-1}^\dagger(y,t) \psi_J(y,t) dy + \text{H.c.}, \end{aligned} \quad (5.49)$$

where $c_{J,J\pm 1}$ are complex coupling coefficients between channels J and $J\pm 1$, and satisfy boundary conditions $c_{1,0} = c_{N,N+1} = 0$. If we write explicitly all the terms in the equation (5.49) and factor the coefficients for the same operators we find

$$\mathcal{H}_C = \sum_{J=1}^{N-1} \sigma_{J,J+1} \int \psi_J^\dagger(y,t) \psi_{J+1}(y,t) dy + \text{H.c.}, \quad (5.50)$$

with coupling coefficients

$$\sigma_{J,J+1} = (c_{J,J-1} + c_{J,J+1}^*), \quad (5.51)$$

that can be written in the form $\sigma_{J,J+1} = \hbar v_J \kappa_{J,J+1}$ to give the Hamiltonian the correct dimension of energy, and the $\kappa_{J,J+1}$ are the usual coefficients from coupled-wave analysis having units of $[\text{L}^{-1}]$. The contribution of (5.50) to the dynamical evolution of the channel operators is

$$\frac{1}{i\hbar} [\psi_J(y,t), \mathcal{H}_C] = \frac{1}{i\hbar} (\sigma_{J,J+1} \psi_{J+1}(y,t) + \sigma_{J-1,J}^* \psi_{J-1}(y,t)), \quad (5.52)$$

which result in off-diagonal terms in the matrix operator that describe the time evolution of all the channel operators $\phi_J(y,t)$ and their Hermitian conjugates in the dynamical equation corresponding to the general case of Eq. (5.33). At this point one must reconsider the strategy of resolution for the corresponding Green function problem, since in this case the split-step

method could be extremely demanding, both computationally and in terms of time. The decision is relevant considering that the goal is to perform an analysis on the effects of disorder, and this requires a large ensemble. In conclusion, these steps and their implementation represents right now the status of our research and will be the focus of the following months.

CONCLUSIONS

The improving possibility to generate and manipulate the quantum state of physical objects has spurred researchers to envision a new generation of quantum technologies that can dramatically improve the efficiency, accuracy, and security of many application that today still rely on classical principles. This new class of devices that operate on the base of quantum mechanics and its rules are expected to bring a breakthrough in many fields such as information, communication, computing, and sensing. While every one of these fields is just starting to find its natural platform to achieve this transformation, photonics has emerged to become an ideal candidate for many applications in which the quantum state of light is exploited to perform the required tasks. The strength of the photonic platform resides in its ability to be integrated in micro-structures fabricated with standard technologies borrowed from the electronic industry. This incredible advantage has already proven to be fundamental for the stability of all the integrated elements, which can be many, and for the properties of the generated quantum state of light. Despite this property the fabrication process inevitably introduces defects in the positioning and features of the integrated elements that can compromise the quality of the output quantum state. To mitigate this problem it has been suggested to exploit topology in photonic applications, with the aim of creating structures that are robust against random disorder. In this work we focused on a particular kind of one-dimensional topological structure that can be reproduced with a waveguide array, and we performed a thorough statistical analysis of the effects of disorder on both the linear properties of the supported topological guided mode, and the generation of photon pairs in it via parametric fluorescence. The purpose of this research is to investigate if the topological protection observed in the linear regime is also effective in shielding from disorder the properties of the generated photons quantum state.

In the first part of this work we introduced the fundamental concepts and mathematical tools to understand our findings. In Ch. 1 we presented the topological photonic structure used in this study, which can be understood as

the photonic analogue of the Su-Schrieffer-Heeger model describing the formation of a topological electronic state in a dimer chain molecule. The structure is one-dimensional and can be easily reproduced with an array of parallel waveguides appropriately positioned. Specifically, in our work we considered the reference structure of the model, with one topological defect, and a second structure, with two closely separated defects that result in the formation of two strongly coupled topological modes. We described the propagation of light in the arrays with a simplified model that assumes the waveguide modes to be orthogonal, with energy exchange between waveguides described in a tight-binding approach. This model reproduces the formation of the topological mode in both structures and is simple enough to be implemented in simulations. The linear properties of the topological mode were studied in the presence of positional disorder that modifies the relative distance of the waveguides in the transverse dimension of the array. We confirmed the robustness against disorder in the linear regime observing that some properties of the topological mode, such as its propagation constant and field distribution, are very weakly affected by disorder compared to all the other modes. In Ch. 2 we gave a background on the nonlinear quantum processes that are used to generate two-photon states. In particular, we considered spontaneous four-wave mixing (SFWM) and spontaneous parametric down conversion (SPDC) for the generation of photon pairs, respectively in the reference structure and the one with two topological defects. We presented the method of asymptotic fields for the treatment of nonlinear processes in large integrated structure, and the backward Heisenberg approach to derive the state of the generated photons starting from an initial input state. Finally, we introduced appropriate figures of merit, coming from the theory of quantum mechanics, to track in a quantitative way the effects of disorder on the quantum state of the generated photons.

In the second part we presented our results on the topological protection of the generated photon pairs state properties. Specifically, in Ch. 3 we focused on SFWM in an array supporting a single topological mode, where we analyzed the state of photon pairs in the path degree of freedom. An initial inspection of the path state showed that photons are generated not entangled, with a Schmidt number (SN) close to 1 and a joint path intensity (JPI) symmetrical along the two axis. By introducing moderate levels of disorder in the structure, we showed that the fidelity of the state and the SN are weakly affected, and the JPI continues to display the symmetry properties of the topological mode field profile. As disorder increases to larger levels the drop in fidelity is accompanied by an increase of the SN. We demonstrated that this is caused by an increased efficiency in the nonlinear coupling of the topological mode with other modes of the array in the SFWM process, and

we identified two contributions, intra- and inter-mode SFWM. These non-linear interactions are responsible with different weights for the degradation of the state and its topological protection, the second being twice more effective than the first. The role of these contributions is also visible in the JPI, with the appearance of terms that would be null had the two photons been generated only in the topological mode. In Ch. 4 we studied the generation of photon pairs by SPDC in an array supporting two strongly coupled topological modes, focusing on both the spectral and path properties of their state. When we initially investigating the unperturbed structure, an inspection of the state revealed that, within the generation bandwidth considered, the generated photons are entangled both in path and frequency, but these components are not correlated with each other and the respective reduced states in either degree of freedom are pure. The entanglement of the photons was confirmed by an analysis in terms of SN: in frequency this is due to properties of the pump pulse with respect to the phase matching bandwidth; in path this is due to the strong coupling of the topological modes. Thus, we demonstrated that the generated state is by all means hyper-entangled. Following the same approach used for the SFWM case, we studied the effects of disorder on the hyper-entangled state. Our analysis showed that the purity of the reduced state in path is well preserved for all levels of disorder thanks to the small collection bandwidth and the weak spectral dependence of the coupling constants on disorder. The fidelity of the generated state, in contrast, is robust against perturbations for low levels of disorder, while at higher levels drops significantly with a large variance. This behaviour, which is similar to that observed in the SFWM case, hid a different cause that was revealed by our analysis in terms of SN and Schmidt decomposition of the reduced path state. Here, the loss of symmetry in the structure due to disorder is the main cause of the state degradation with disorder, and the nonlinear coupling with other modes of the array that are not topological plays only a minor role thanks to the stringent requirements of SPDC in terms of phase matching and mode overlap.

Finally, in the last chapter we presented a preliminary work on our current research direction. There, we introduced the theoretical elements to extend the study on topological protection to the generation of squeezed states of light, which are important for many applications ranging from metrology, where noise reduction is a pivotal requirement, to quantum computing based on continuous variables. The mathematical model we presented and verified in the case of a single waveguide will be adapted to the case of an array structure and then a similar statistical process will be performed to study the effects of disorder.

In conclusion, we can state that topological protection can be effective in

preserving the properties of the generated quantum state if the level of disorder is small and perturbations of the structure do not modify the supported modes excessively. The maximum level that can be tolerated depends on the quality of the state required by the specific application, as in general the state properties degrade smoothly with disorder and there isn't a threshold with a clear discontinuity indicating the loss of topological protection. The main point, though, is that topological protection of the linear properties is very effective because it involves each mode separately, however it doesn't extend equally well to nonlinear interactions, which are based on the simultaneous interaction of more than one mode in the photon pair generation process. This was highlighted in the case of SFWM by the inter- and intra-mode mechanisms, which enhance the role played by other non topological modes supported by the array, and in the case of SPDC by the reduction of structure symmetry, which leads to an imbalance in the relative weight of the two available topological modes.

APPENDIX: THE BACKWARD HEISENBERG PICTURE APPROACH

We start by recalling the connection between the asymptotic-in and -out states in the backward Heisenberg picture

$$|\psi_{\text{out}}\rangle = U(t_1, t_0) |\psi_{\text{in}}\rangle, \quad (53)$$

where the operator $U(t_1, t_0)$ is

$$U(t_1, t_0) = e^{iH_L t_1/\hbar} e^{-iH(t_1-t_0)/\hbar} e^{-iH_L t_0/\hbar}, \quad (54)$$

and the asymptotic-in state is taken as a coherent quantum state

$$|\psi_{\text{in}}\rangle = e^O |\text{vac}\rangle, \quad (55)$$

with the operator O defined as

$$O = \alpha A^\dagger - \text{H.c.}, \quad (56)$$

with

$$A^\dagger = \int dk \phi_P(k) c_k^\dagger. \quad (57)$$

Using the equation (53) and (55) the asymptotic-out state becomes

$$\begin{aligned} |\psi_{\text{out}}\rangle &= U(t_1, t_0) e^O U^\dagger(t_1, t_0) |\text{vac}\rangle \\ &= e^{U(t_1, t_0) O U^\dagger(t_1, t_0)} |\text{vac}\rangle \\ &= e^{\bar{O}(t_0)} |\text{vac}\rangle, \end{aligned} \quad (58)$$

and the operator $\bar{O}(t_0)$ evolved in time is

$$\bar{O}(t_0) = U(t_1, t_0) O U^\dagger(t_1, t_0), \quad (59)$$

which satisfies the final boundary condition $\bar{O}(t_1) = O$ and the dynamical equation

$$i\hbar \frac{\partial \bar{O}(t)}{\partial t} = [\bar{O}(t), \hat{V}(t)], \quad (60)$$

with $\hat{V}(t) = U(t_1, t) V(t) U^\dagger(t_1, t)$ and

$$V(t) = e^{iH_L t/\hbar} H_{\text{NL}} e^{-iH_L t/\hbar}. \quad (61)$$

The form of the operator $\hat{V}(t)$ depends on the nonlinear process considered, thus from here we present separately the mathematical steps to solve the backward time evolution.

SPDC PROCESS

For the SPDC process we have the nonlinear Hamiltonian is

$$H_{\text{NL}} = - \int dk_1 dk_2 dk S(k_1, k_2, k) c_{k_1}^\dagger c_{k_2}^\dagger c_k + \text{H.c.}, \quad (62)$$

and thus the operator $\hat{V}(t)$ has the form

$$\hat{V}(t) = - \int dk_1 dk_2 dk S(k_1, k_2, k; t) \bar{c}_{k_1}^\dagger(t) \bar{c}_{k_2}^\dagger(t) \bar{c}_k(t) + \text{H.c.}, \quad (63)$$

and

$$S(k_1, k_2, k; t) = S(k_1, k_2, k) e^{-i(\omega_k - \omega_{k_1} - \omega_{k_2})t}. \quad (64)$$

At the same time we see from Eqs. (59) and (56) that

$$\bar{A}^\dagger(t_0) = \int dk \phi_P(k) \bar{c}_k^\dagger(t_0), \quad (65)$$

and from the dynamical equation (60) we can build a set of differential equation for $\bar{c}_k^\dagger(t)$ as

$$i\hbar \frac{d\bar{c}_k^\dagger(t)}{dt} = \int dk_1 dk_2 S(k_1, k_2, k; t) \bar{c}_{k_1}^\dagger(t) \bar{c}_{k_2}^\dagger(t), \quad (66)$$

and the same applies for the $\bar{c}_{k_i}^\dagger(t)$. It is intended that all these barred creation operators satisfy a final condition similar to $\bar{O}(t)$ in the sense that at the final time $t = t_1$ they are equal to their respective non-barred operator, which represents the *zero-th* order solution of the respective differential equation (66). Looking for solution to the first order we find

$$\bar{c}_k^\dagger(t) = c_k^\dagger + \frac{1}{i\hbar} \int dk_1 dk_2 \left[\int_{t_1}^t dt' S(k_1, k_2, k; t') \right] c_{k_1}^\dagger c_{k_2}^\dagger, \quad (67)$$

and evaluating $\bar{c}_k^\dagger(t_0)$, inverting the range of integration over t' and extending $t_1 \rightarrow \infty$ and $t_0 \rightarrow -\infty$, we find that the barred operator \bar{A}^\dagger can be written as

$$\bar{A}^\dagger(-\infty) = A^\dagger + \frac{\beta}{\alpha} C_{\text{II}}^\dagger \quad (68)$$

where C_{II}^\dagger is

$$C_{\text{II}}^\dagger = \frac{1}{\sqrt{2}} \int dk_1 dk_2 \phi(k_1, k_2) c_{k_1}^\dagger c_{k_2}^\dagger, \quad (69)$$

and $\phi(k_1, k_2)$ is the biphoton wave function

$$\phi(k_1, k_2) = \frac{i\sqrt{2}\alpha}{\hbar\beta} \int dk \phi_P(k) \int_{-\infty}^{\infty} dt S(k_1, k_2, k; t), \quad (70)$$

normalized as

$$\int dk_1 dk_2 |\phi(k_1, k_2)|^2 = 1. \quad (71)$$

Using Eq. (68) with (56) in the last line of (58), we can now write the asymptotic-out state as

$$|\psi_{\text{out}}\rangle = e^{(\alpha A^\dagger + \beta C_{\text{II}}^\dagger) - \text{H.c.}} |\text{vac}\rangle, \quad (72)$$

and since the operators A^\dagger and C_{II}^\dagger commute

$$\begin{aligned} |\psi_{\text{out}}\rangle &= e^{(\alpha A^\dagger + \beta C_{\text{II}}^\dagger) - \text{H.c.}} |\text{vac}\rangle \\ &= e^{\alpha A^\dagger - \text{H.c.}} e^{\beta C_{\text{II}}^\dagger - \text{H.c.}} |\text{vac}\rangle, \end{aligned} \quad (73)$$

we can also write it as

$$|\psi_{\text{out}}\rangle = e^{\alpha A^\dagger - \text{H.c.}} |\psi_{\text{out}}\rangle_{\text{gen}}, \quad (74)$$

where $|\psi_{\text{out}}\rangle_{\text{gen}}$ is the state of the generated photons

$$|\psi_{\text{out}}\rangle_{\text{gen}} = e^{\beta C_{\text{II}}^\dagger - \text{H.c.}} |\text{vac}\rangle. \quad (75)$$

When the parameter $|\beta|^2$ is small we can expand this state to the first order as

$$|\psi_{\text{out}}\rangle_{\text{gen}} \approx |\text{vac}\rangle + \beta |\text{II}\rangle + \dots, \quad (76)$$

and

$$|\text{II}\rangle = C_{\text{II}}^\dagger |\text{vac}\rangle = \frac{1}{\sqrt{2}} \int dk_1 dk_2 \phi(k_1, k_2) c_{k_1}^\dagger c_{k_2}^\dagger |\text{vac}\rangle \quad (77)$$

is the normalized two-photon state with $|\beta|^2$ representing the generation probability per pulse of a pair when this approximation is valid.

We can now work a bit on $\phi(k_1, k_2)$ to simplify the form (70) and we also try to rewrite the state (77) in the frequency domain, which is the one used in our simulations. We start by completing the Fourier transform of $S(k_1, k_2, k)$

$$\int_{-\infty}^{\infty} dt S(k_1, k_2, k; t) = 2\pi S(k_1, k_2, k) \delta(\omega_k - \omega_{k_1} - \omega_{k_2}), \quad (78)$$

and we assume that pump spectrum is peaked enough in wavevector space so that it is different from zero only in the range of positive k . In this case, with typical dispersion relations, also the photon pairs can be considered generated in a bandwidth covering only positive k_1 and k_2 . Then, since a one-to-one relation between positive wavevectors and positive frequencies can be established, we define new operators

$$\tilde{c}_{\omega}^{\dagger} = \sqrt{\frac{dk(\omega)}{d\omega}} c_{k(\omega)}^{\dagger}, \quad (79)$$

so that the commutation relations remain in a canonical form, and

$$\tilde{\phi}_P(\omega) = \sqrt{\frac{dk(\omega)}{d\omega}} \phi_P(k(\omega)), \quad (80)$$

is now normalized as

$$\int_0^{\infty} d\omega |\tilde{\phi}_P(\omega)|^2 = 1. \quad (81)$$

The new biphoton wavefunction in frequency becomes

$$\begin{aligned} \tilde{\phi}(\omega_1, \omega_2) &= \frac{2\sqrt{2}i\pi\alpha}{\hbar\beta} \sqrt{\frac{dk(\omega_1)}{d\omega_1}} \sqrt{\frac{dk(\omega_2)}{d\omega_2}} \sqrt{\frac{dk(\omega_1 + \omega_2)}{d(\omega_1 + \omega_2)}} \\ &\times \phi_P(\omega_1 + \omega_2) S(\omega_1, \omega_2, \omega_1 + \omega_2), \end{aligned} \quad (82)$$

normalized as

$$\int_0^{\infty} d\omega_1 \int_0^{\infty} d\omega_2 |\tilde{\phi}(\omega_1, \omega_2)|^2 = 1, \quad (83)$$

and the normalized two-photons state becomes

$$|\text{II}\rangle = \frac{1}{\sqrt{2}} \int_0^{\infty} d\omega_1 d\omega_2 \tilde{\phi}(\omega_1, \omega_2) \tilde{c}_{\omega_1}^{\dagger} \tilde{c}_{\omega_2}^{\dagger} |\text{vac}\rangle. \quad (84)$$

SFWM PROCESS

The steps for the SFWM process are similar but there are some subtleties that must be considered. In this case the nonlinear Hamiltonian is

$$H_{\text{NL}} = - \int dk_1 dk_2 dk_3 dk_4 S(k_1, k_2, k_3, k_4) c_{k_1}^\dagger c_{k_2}^\dagger c_{k_3} c_{k_4} + \text{H.c.}, \quad (85)$$

and the corresponding operator $\hat{V}(t)$ has the form

$$\begin{aligned} \hat{V}(t) = & - \int dk_1 dk_2 dk_3 dk_4 S(k_1, k_2, k_3, k_4; t) \\ & \times \bar{c}_{k_1}^\dagger(t) \bar{c}_{k_2}^\dagger(t) \bar{c}_{k_3}(t) \bar{c}_{k_4}(t) + \text{H.c.}, \end{aligned} \quad (86)$$

with

$$S(k_1, k_2, k_3, k_4; t) = S(k_1, k_2, k_3, k_4) e^{-i(\omega_{k_4} + \omega_{k_3} - \omega_{k_1} - \omega_{k_2})t}. \quad (87)$$

As before, we see that the barred operator $\bar{A}^\dagger(t)$ in the asymptotic-out state is

$$\bar{A}^\dagger(t) = \int dk \phi_P(k) \bar{c}_k^\dagger(t), \quad (88)$$

and from the dynamical equation (60) we build a set of differential equation for $\bar{c}_k^\dagger(t)$ as

$$i\hbar \frac{d\bar{c}_k^\dagger(t)}{dt} = 2 \int dk_1 dk_2 dk_3 S(k_1, k_2, k_3, k; t) \bar{c}_{k_1}^\dagger(t) \bar{c}_{k_2}^\dagger(t) \bar{c}_{k_3}(t). \quad (89)$$

Recalling that the non-barred operators c_k^\dagger are zeroth-order solutions of these equations, we find that the first order solution for $\bar{c}_k^\dagger(t)$ is

$$\begin{aligned} \bar{c}_k^\dagger(t) &= c_k^\dagger + \frac{2}{i\hbar} \int dk_1 dk_2 dk_3 \left[\int_{t_1}^{t_0} dt' S(k_1, k_2, k_3, k; t') \right] c_{k_1}^\dagger c_{k_2}^\dagger c_{k_3} \\ &= c_k^\dagger + \frac{4\pi i}{\hbar} \int dk_1 dk_2 dk_3 S(k_1, k_2, k_3, k) c_{k_1}^\dagger c_{k_2}^\dagger c_{k_3} \\ &\quad \times \delta(\omega_{k_3} + \omega_k - \omega_{k_2} - \omega_{k_1}), \end{aligned} \quad (90)$$

where again we extended to infinity the range of integration over t' and used the Fourier transform of $S(k_1, k_2, k_3, k; t')$ to eliminate the integral. If we substitute the solution (90) back into Eq. (88) we see that

$$|\psi_{\text{out}}\rangle = e^{\bar{O}(-\infty)} |\text{vac}\rangle, \quad (91)$$

with $\bar{O}(-\infty)$ composed of two terms A and B

$$\begin{aligned} A &= \alpha \int dk \phi_P(k) c_k^\dagger - \text{H.c.} \\ B &= \frac{4\pi i \alpha}{\hbar} \int dk \phi_P(k) \int dk_1 dk_2 dk_3 S(k_1, k_2, k_3, k) c_{k_1}^\dagger c_{k_2}^\dagger c_{k_3} \\ &\quad \times \delta(\omega_{k_3} + \omega_k - \omega_{k_2} - \omega_{k_1}) - \text{H.c.}, \end{aligned} \quad (92)$$

that don't commute because of the presence of c_{k_3} in B . What we can do is to use the *Baker-Campbell-Hausdorff* (BCH) formula to write an approximate factorized solution of the exponentiated operator $\bar{O}(-\infty)$.

To the first order, the BCH formula is

$$e^{A+B} = e^A e^{-\frac{1}{2}[A,B]} e^B, \quad (93)$$

and considering that $\exp(B)$ acts on the vacuum state like the identity, precisely because of the destruction operator, we focus only on the commutator $[A, B]$. Keeping only the terms corresponding to the creation of two photons we find that

$$\begin{aligned} -\frac{1}{2}[A, B] &= \frac{2\pi i \alpha^2}{\hbar} \int dk \phi_P(k) \int dk_1 dk_2 dk_3 \phi_P(k_3) \\ &\quad \times S(k_1, k_2, k_3, k) c_{k_1}^\dagger c_{k_2}^\dagger \delta(\omega_{k_3} + \omega_k - \omega_{k_2} - \omega_{k_1}) - \text{H.c.}, \end{aligned} \quad (94)$$

and thus the asymptotic-out state can be written

$$|\psi_{\text{out}}\rangle = e^{(\alpha A^\dagger + \beta C_{\text{II}}^\dagger) - \text{H.c.}} |\text{vac}\rangle, \quad (95)$$

as in (72), where

$$C_{\text{II}}^\dagger = \frac{1}{\sqrt{2}} \int dk_1 dk_2 \phi(k_1, k_2) c_{k_1}^\dagger c_{k_2}^\dagger, \quad (96)$$

is identical to Eq. (69) but now the biphoton wave function $\phi(k_1, k_2)$ is different

$$\begin{aligned} \phi(k_1, k_2) &= \frac{2\sqrt{2}i\pi\alpha^2}{\hbar\beta} \int dk_3 dk \phi_P(k) \phi_P(k_3) \\ &\quad \times S(k_1, k_2, k_3, k) \delta(\omega_{k_3} + \omega_k - \omega_{k_2} - \omega_{k_1}), \end{aligned} \quad (97)$$

with β the constant that normalizes it to unity as

$$\int dk_1 dk_2 |\phi(k_1, k_2)|^2 = 1. \quad (98)$$

Following the same argument done for the SPDC process we can move from the wavevector space to the frequencies and the biphoton wave function becomes

$$\begin{aligned} \tilde{\phi}(\omega_1, \omega_2) &= \frac{2\sqrt{2}i\pi\alpha^2}{\hbar\beta} \sqrt{\frac{dk(\omega_1)}{d\omega_1}} \sqrt{\frac{dk(\omega_2)}{d\omega_2}} \\ &\times \int_0^\infty d\omega \left\{ \sqrt{\frac{dk(\omega)}{d\omega}} \sqrt{\frac{dk(\omega_1 + \omega_2 - \omega)}{d(\omega_1 + \omega_2 - \omega)}} \right. \\ &\left. \times \phi_P(\omega)\phi_P(\omega_1 + \omega_2 - \omega)S(\omega_1, \omega_2, \omega) \right\}, \end{aligned} \quad (99)$$

which is normalized as Eq. (83). The state of the generated photons can be written again as

$$|\psi_{\text{out}}\rangle_{\text{gen}} = e^{\beta C_{\text{II}}^\dagger - \text{H.c.}} |\text{vac}\rangle, \quad (100)$$

and when the parameter $|\beta|^2$ is small we can expand this state to the first order as

$$|\psi_{\text{out}}\rangle_{\text{gen}} \approx |\text{vac}\rangle + \beta |\text{II}\rangle + \dots, \quad (101)$$

with $|\beta|^2$ the generation probability per pulse of a photon pair and

$$|\text{II}\rangle = \frac{1}{\sqrt{2}} \int_0^\infty d\omega_1 d\omega_2 \tilde{\phi}(\omega_1, \omega_2) \tilde{c}_{\omega_1}^\dagger \tilde{c}_{\omega_2}^\dagger |\text{vac}\rangle. \quad (102)$$

the normalized two-photon state.

PUBLICATIONS

Publications marked with an asterisk * are directly related to the topic of this thesis

- N. Bergamasco, M. Menotti, J. E. Sipe, and M. Liscidini “*Generation of path-encoded Greenberger-Horne-Zeilinger states*” Phys. Rev. Applied **8**, 054014 (2017)
- M.P. Massara, M. Menotti, N. Bergamasco, N. C. Harris, T. Baehr-Jones, M. Hochberg, C. Galland, M. Liscidini, M. Galli, and D. Bajoni “*Nonlinear characterization of a silicon integrated Bragg waveguides*” Opt. Lett. **43**, 1171-1174 (2018)
- * N. Bergamasco M. Liscidini “*Generation of photon pairs in topologically protected guided modes*”, Phys. Rev. A **100**, 053827 (2019).
- * N. Bergamasco, J. E. Sipe, and M. Liscidini ” *Generation of hyper-entangled states in strongly coupled topological defects*” Opt. Lett. **46**, 2244-2247 (2021)

BIBLIOGRAPHY

- ¹K. v. Klitzing, G. Dorda, and M. Pepper, “New method for high-accuracy determination of the fine-structure constant based on quantized hall resistance”, *Phys. Rev. Lett.* **45**, 494–497 (1980).
- ²R. B. Laughlin, “Quantized hall conductivity in two dimensions”, *Phys. Rev. B* **23**, 5632–5633 (1981).
- ³D. J. Thouless, M. Kohmoto, M. P. Nightingale, and M. den Nijs, “Quantized hall conductance in a two-dimensional periodic potential”, *Phys. Rev. Lett.* **49**, 405–408 (1982).
- ⁴F. D. M. Haldane and S. Raghu, “Possible realization of directional optical waveguides in photonic crystals with broken time-reversal symmetry”, *Phys. Rev. Lett.* **100**, 013904 (2008).
- ⁵S. Raghu and F. D. M. Haldane, “Analogues of quantum-hall-effect edge states in photonic crystals”, *Phys. Rev. A* **78**, 033834 (2008).
- ⁶Z. Wang, Y. Chong, J. D. Joannopoulos, and M. Soljačić, “Observation of unidirectional backscattering-immune topological electromagnetic states”, *Nature* **461**, 772–775 (2009).
- ⁷T. Kitagawa, M. A. Broome, A. Fedrizzi, M. S. Rudner, E. Berg, I. Kassal, A. Aspuru-Guzik, E. Demler, and A. G. White, “Observation of topologically protected bound states in photonic quantum walks”, *Nature Communications* **3**, 882 (2012).
- ⁸M. C. Rechtsman, J. M. Zeuner, Y. Plotnik, Y. Lumer, D. Podolsky, F. Dreisow, S. Nolte, M. Segev, and A. Szameit, “Photonic floquet topological insulators”, *Nature* **496**, 196–200 (2013).
- ⁹P. A. Franken, A. E. Hill, C. W. Peters, and G. Weinreich, “Generation of optical harmonics”, *Phys. Rev. Lett.* **7**, 118–119 (1961).
- ¹⁰N. Bloembergen, *Nonlinear optics*, *Frontiers in physics* (Benjamin, 1965).

- ¹¹D. C. Burnham and D. L. Weinberg, “Observation of simultaneity in parametric production of optical photon pairs”, *Phys. Rev. Lett.* **25**, 84–87 (1970).
- ¹²R. E. Slusher, L. W. Hollberg, B. Yurke, J. C. Mertz, and J. F. Valley, “Observation of squeezed states generated by four-wave mixing in an optical cavity”, *Phys. Rev. Lett.* **55**, 2409–2412 (1985).
- ¹³A. Politi, M. J. Cryan, J. G. Rarity, S. Yu, and J. L. O’Brien, “Silica-on-silicon waveguide quantum circuits”, *Science* **320**, 646–649 (2008).
- ¹⁴J. P. Sprengers, A. Gaggero, D. Sahin, S. Jahanmirinejad, G. Frucci, F. Mattioli, R. Leoni, J. Beetz, M. Lermer, M. Kamp, S. Höfling, R. Sanjines, and A. Fiore, “Waveguide superconducting single-photon detectors for integrated quantum photonic circuits”, *Applied Physics Letters* **99**, 181110 (2011).
- ¹⁵C. W. Gardiner and M. J. Collett, “Input and output in damped quantum systems: quantum stochastic differential equations and the master equation”, *Phys. Rev. A* **31**, 3761–3774 (1985).
- ¹⁶A. Blanco-Redondo, I. Andonegui, M. J. Collins, G. Harari, Y. Lumer, M. C. Rechtsman, B. J. Eggleton, and M. Segev, “Topological optical waveguiding in silicon and the transition between topological and trivial defect states”, *Phys. Rev. Lett.* **116**, 163901 (2016).
- ¹⁷A. Blanco-Redondo, B. Bell, D. Oren, B. J. Eggleton, and M. Segev, “Topological protection of biphoton states”, *Science* **362**, 568–571 (2018).
- ¹⁸K. Fang, Z. Yu, and S. Fan, “Realizing effective magnetic field for photons by controlling the phase of dynamic modulation”, *Nature Photonics* **6**, 782–787 (2012).
- ¹⁹M. C. Rechtsman, J. M. Zeuner, A. Tünnermann, S. Nolte, M. Segev, and A. Szameit, “Strain-induced pseudomagnetic field and photonic landau levels in dielectric structures”, *Nature Photonics* **7**, 153–158 (2013).
- ²⁰R. O. Umucalılar and I. Carusotto, “Artificial gauge field for photons in coupled cavity arrays”, *Phys. Rev. A* **84**, 043804 (2011).
- ²¹M. Hafezi, E. A. Demler, M. D. Lukin, and J. M. Taylor, “Robust optical delay lines with topological protection”, *Nature Physics* **7**, 907–912 (2011).
- ²²M. Hafezi, S. Mittal, J. Fan, A. Migdall, and J. M. Taylor, “Imaging topological edge states in silicon photonics”, *Nature Photonics* **7**, 1001–1005 (2013).
- ²³W. P. Su, J. R. Schrieffer, and A. J. Heeger, “Solitons in polyacetylene”, *Phys. Rev. Lett.* **42**, 1698–1701 (1979).

- ²⁴N. Malkova, I. Hromada, X. Wang, G. Bryant, and Z. Chen, “Observation of optical shockley-like surface states in photonic superlattices”, *Opt. Lett.* **34**, 1633–1635 (2009).
- ²⁵M. Verbin, O. Zilberberg, Y. E. Kraus, Y. Lahini, and Y. Silberberg, “Observation of topological phase transitions in photonic quasicrystals”, *Phys. Rev. Lett.* **110**, 076403 (2013).
- ²⁶R. Luo, Y. He, H. Liang, M. Li, and Q. Lin, “Highly tunable efficient second-harmonic generation in a lithium niobate nanophotonic waveguide”, *Optica* **5**, 1006–1011 (2018).
- ²⁷N. Quesada and J. E. Sipe, “Why you should not use the electric field to quantize in nonlinear optics”, *Opt. Lett.* **42**, 3443–3446 (2017).
- ²⁸R. W. Boyd, *Nonlinear optics* (Elsevier, 2007).
- ²⁹J. E. Sipe, N. A. R. Bhat, P. Chak, and S. Pereira, “Effective field theory for the nonlinear optical properties of photonic crystals”, *Phys. Rev. E* **69**, 016604 (2004).
- ³⁰J. D. Jackson, *Classical electrodynamics*, 3rd ed. (Wiley, New York, NY, 1999).
- ³¹L. G. Helt, M. Liscidini, and J. E. Sipe, “How does it scale? comparing quantum and classical nonlinear optical processes in integrated devices”, *J. Opt. Soc. Am. B* **29**, 2199–2212 (2012).
- ³²M. Liscidini, L. G. Helt, and J. E. Sipe, “Asymptotic fields for a hamiltonian treatment of nonlinear electromagnetic phenomena”, *Phys. Rev. A* **85**, 013833 (2012).
- ³³G. Breit and H. A. Bethe, “Ingoing waves in final state of scattering problems”, *Phys. Rev.* **93**, 888–890 (1954).
- ³⁴Z. Yang, M. Liscidini, and J. E. Sipe, “Spontaneous parametric down-conversion in waveguides: a backward heisenberg picture approach”, *Phys. Rev. A* **77**, 033808 (2008).
- ³⁵J. H. Eberly, “Schmidt analysis of pure-state entanglement”, *Laser Physics* **16**, 921–926 (2006).
- ³⁶J. E. Sharping, K. F. Lee, M. A. Foster, A. C. Turner, B. S. Schmidt, M. Lipson, A. L. Gaeta, and P. Kumar, “Generation of correlated photons in nanoscale silicon waveguides”, *Opt. Express* **14**, 12388–12393 (2006).
- ³⁷S. Clemmen, K. P. Huy, W. Bogaerts, R. G. Baets, P. Emplit, and S. Massar, “Continuous wave photon pair generation in silicon-on-insulator waveguides and ring resonators”, *Opt. Express* **17**, 16558–16570 (2009).

- ³⁸S. Azzini, D. Grassani, M. J. Strain, M. Sorel, L. G. Helt, J. E. Sipe, M. Liscidini, M. Galli, and D. Bajoni, “Ultra-low power generation of twin photons in a compact silicon ring resonator”, *Opt. Express* **20**, 23100–23107 (2012).
- ³⁹M. Savanier, R. Kumar, and S. Mookherjea, “Photon pair generation from compact silicon microring resonators using microwatt-level pump powers”, *Opt. Express* **24**, 3313–3328 (2016).
- ⁴⁰S. Azzini, D. Grassani, M. Galli, D. Gerace, M. Patrini, M. Liscidini, P. Velha, and D. Bajoni, “Stimulated and spontaneous four-wave mixing in silicon-on-insulator coupled photonic wire nano-cavities”, *Applied Physics Letters* **103**, 031117 (2013).
- ⁴¹C. M. Gentry, X. Zeng, and M. A. Popović, “Tunable coupled-mode dispersion compensation and its application to on-chip resonant four-wave mixing”, *Opt. Lett.* **39**, 5689–5692 (2014).
- ⁴²X. Zeng, C. M. Gentry, and M. A. Popović, “Four-wave mixing in silicon coupled-cavity resonators with port-selective, orthogonal supermode excitation”, *Opt. Lett.* **40**, 2120–2123 (2015).
- ⁴³M. Menotti, B. Morrison, K. Tan, Z. Vernon, J. E. Sipe, and M. Liscidini, “Nonlinear coupling of linearly uncoupled resonators”, *Phys. Rev. Lett.* **122**, 013904 (2019).
- ⁴⁴Z. Vernon, M. Menotti, C. C. Tison, J. A. Steidle, M. L. Fanto, P. M. Thomas, S. F. Preble, A. M. Smith, P. M. Alsing, M. Liscidini, and J. E. Sipe, “Truly unentangled photon pairs without spectral filtering”, *Opt. Lett.* **42**, 3638–3641 (2017).
- ⁴⁵J. W. Silverstone, D. Bonneau, K. Ohira, N. Suzuki, H. Yoshida, N. Iizuka, M. Ezaki, C. M. Natarajan, M. G. Tanner, R. H. Hadfield, V. Zwiller, G. D. Marshall, J. G. Rarity, J. L. O’Brien, and M. G. Thompson, “On-chip quantum interference between silicon photon-pair sources”, *Nature Photonics* **8**, 104–108 (2014).
- ⁴⁶T. Onodera, M. Liscidini, J. E. Sipe, and L. G. Helt, “Parametric fluorescence in a sequence of resonators: an analogy with dicke superradiance”, *Phys. Rev. A* **93**, 043837 (2016).
- ⁴⁷N. Bergamasco and M. Liscidini, “Generation of photon pairs in topologically protected guided modes”, *Phys. Rev. A* **100**, 053827 (2019).
- ⁴⁸A. B. Khanikaev, S. Hossein Mousavi, W.-K. Tse, M. Kargarian, A. H. MacDonald, and G. Shvets, “Photonic topological insulators”, *Nature Materials* **12**, 233–239 (2013).

- ⁴⁹C. W. Hsu, B. Zhen, J. Lee, S.-L. Chua, S. G. Johnson, J. D. Joannopoulos, and M. Soljačić, “Observation of trapped light within the radiation continuum”, *Nature* **499**, 188–191 (2013).
- ⁵⁰L. Piloizzi and C. Conti, “Topological lasing in resonant photonic structures”, *Phys. Rev. B* **93**, 195317 (2016).
- ⁵¹S. Mittal, E. A. Goldschmidt, and M. Hafezi, “A topological source of quantum light”, *Nature* **561**, 502–506 (2018).
- ⁵²M. Wang, C. Doyle, B. Bell, M. J. Collins, E. Magi, B. J. Eggleton, M. Segev, and A. Blanco-Redondo, “Topologically protected entangled photonic states”, *Nanophotonics* **8**, 1327–1335 (2019).
- ⁵³B. Desiatov, A. Shams-Ansari, M. Zhang, C. Wang, and M. Lončar, “Ultra-low-loss integrated visible photonics using thin-film lithium niobate”, *Optica* **6**, 380–384 (2019).
- ⁵⁴N. Bergamasco, J. E. Sipe, and M. Liscidini, “Generation of hyper-entangled states in strongly coupled topological defects”, *Opt. Lett.* **46**, 2244–2247 (2021).
- ⁵⁵J. T. Barreiro, N. K. Langford, N. A. Peters, and P. G. Kwiat, “Generation of hyperentangled photon pairs”, *Phys. Rev. Lett.* **95**, 260501 (2005).
- ⁵⁶M. A. Ciampini, A. Gherardi, V. Cimini, C. Macchiavello, J. E. Sipe, M. Liscidini, and P. Mataloni, “Stimulated emission tomography: beyond polarization”, *Opt. Lett.* **44**, 41–44 (2019).
- ⁵⁷S. S. Y. Chua, B. J. J. Slagmolen, D. A. Shaddock, and D. E. McClelland, “Quantum squeezed light in gravitational-wave detectors”, *Classical and Quantum Gravity* **31**, 183001 (2014).
- ⁵⁸N. C. Menicucci, P. van Loock, M. Gu, C. Weedbrook, T. C. Ralph, and M. A. Nielsen, “Universal quantum computation with continuous-variable cluster states”, *Phys. Rev. Lett.* **97**, 110501 (2006).
- ⁵⁹M. I. Kolobov and C. Fabre, “Quantum limits on optical resolution”, *Phys. Rev. Lett.* **85**, 3789–3792 (2000).
- ⁶⁰M. O. Scully and M. S. Zubairy, *Quantum optics* (Cambridge University Press, 1997).
- ⁶¹T. R. Taha and M. I. Ablowitz, “Analytical and numerical aspects of certain nonlinear evolution equations. numerical, nonlinear schrödinger equation”, *Journal of Computational Physics* **55**, 203–230 (1984).

FUNDING

This research is sponsored by the RDECOM, RFEC-Atlantic and the US Army Aviation and Missile Research, Development and Engineering Center, under Grant No. W911NF-18-1-0262.